Inelastic Light Scattering Spectroscopy of Lead-based Ferroelectrics

Tae Hyun Kim

February 2014

Inelastic Light Scattering Spectroscopy of Lead-based Ferroelectrics

Tae Hyun Kim
Doctoral Program in Materials Science

Submitted to the Graduate School of
Pure and Applied Sciences
in Partial Fulfillment of the Requirements
for the Degree of Doctor of Philosophy in
Engineering

at the
University of Tsukuba

Abstract

Lead-based ferroelectric materials with the perovskite structure are widely used as electromechanical devices. However, the physical nature of these materials is still not understood completely. Especially, the microscopic origin of the ferroelectric phase transition in these materials has not yet revealed clearly. To understand the phase transition mechanism at the Curie temperature (T_c) and its related lattice dynamics, it is useful to apply inelastic light scattering techniques. Since the optical and acoustical modes are very sensitive to phase transitions and low frequency relaxation phenomena can be directly observed by this method under various conditions, it provides us with the information on the interatomic forces, internal and external vibrations, and relaxation dynamics associated with the ferroelectric phase transitions.

Relaxors are chemically- and structurally-disordered materials, and their relaxation processes exhibit a slowing down behavior. They are characterized by a diffuse phase transition extending in a wide temperature range without any macroscopic structural phase transition. They do not show any ferroelectric long-range order below the dielectric maximum temperature. During the last half century, many researchers have tried explain the diffuse phase transition behavior of the relaxor ferroelectrics by using various experimental and theoretical methods. Presently, it is widely accepted that relaxor properties are generally governed by the dynamics of polar nano-regions (PNRs).

This thesis is devoted to the study of inelastic light-scattering properties of the lead-based binary and ternary ferroelectric single crystals under an external electric field and domain engineering processes. In order to explain the phase transition behaviors, we investigated the characteristic temperatures associated with the evolution of the PNRs by investigating the temperature dependence of their relaxation time.

First, we investigated the phase transition behaviors of unpoled $Pb(In_{1/2}Nb_{1/2})O_3$–$Pb(Mg_{1/3}Nb_{2/3})O_3$–$PbTiO_3$ (PIN–PMN–PT) single crystals by using Brillouin and dielectric spectroscopies in a wide temperature range. For obtaining the characteristic temperatures of PNRs, we investigated the temperature dependences of the dielectric constant and the Brillouin spectra, the former having been analyzed based on the curve fitting procedure by using the Vogel-Fulcher law and the extended Curie-Weiss law.

Second, we compared the phase transition behaviors of unpoled, $[001]_c$-and $[011]_c$-poled single crystals. By using different poling directions a single or peculiar multi-domain structures may be realized according to the domain engineering process. Physical properties such as the sound velocity in a GHz range and low-frequency dielectric properties were investigated having

focused on the complex phase transition behaviors in a frequency range between a few Hz and a few hundreds of GHz.

 Third, we investigated local structure by using angular dependence of Raman scattering. By using Raman tensor analysis, we compare the observed results with the calculated results. After then we analyze the temperature dependence of polarized and depolarize Raman spectra. Lastly, we connect the CPs of Brillouin and Raman scattering spectra to study the broadband spectra. From these analyses, we obtain two-type different relaxation behaviors.

 In this thesis, chaps. 1 and 2 deal with the importance of dynamic properties related to a phase transition. In chap. 3, we describe the experimental conditions about dielectric, Brillouin, and Raman spectroscopies. In chaps. 4~6 describe sequentially the results and discussions about the experimental results of PIN-PMN-PT. Finally, the brief conclusion of the present results is presented.

Contensts

Chapter 5. Phase transition behaviors in relaxor ferroelectric   [011]-poled Pb(In$_{1/2}$Nb$_{1/2}$)O$_3$–Pb(Mg$_{1/3}$Nb$_{2/3}$)O$_3$–PbTiO$_3$ single crystals studied by Brillouin light scattering..61

Chapter 6.   Polarized Raman study of the phonon dynamics in [001]-poled Pb(In$_{1/2}$Nb$_{1/2}$)O$_3$–Pb(Mg$_{1/3}$Nb$_{2/3}$)O$_3$–PbTiO$_3$ single crystals 74

Chapter 1. Introduction

1. 1 Ferroelectricty

Ferroelectricity is a phenomenon that was discovered in single crystals of Rochelle salt [1.1]. Ferroelectrics have a spontaneous electric polarization P_s that can be reversed by the application of an external electric field as shown in Fig. 1. 1 [1.2].

Ps=spontaneous polarization

Pr=remnant polarization

Ec=coercive field
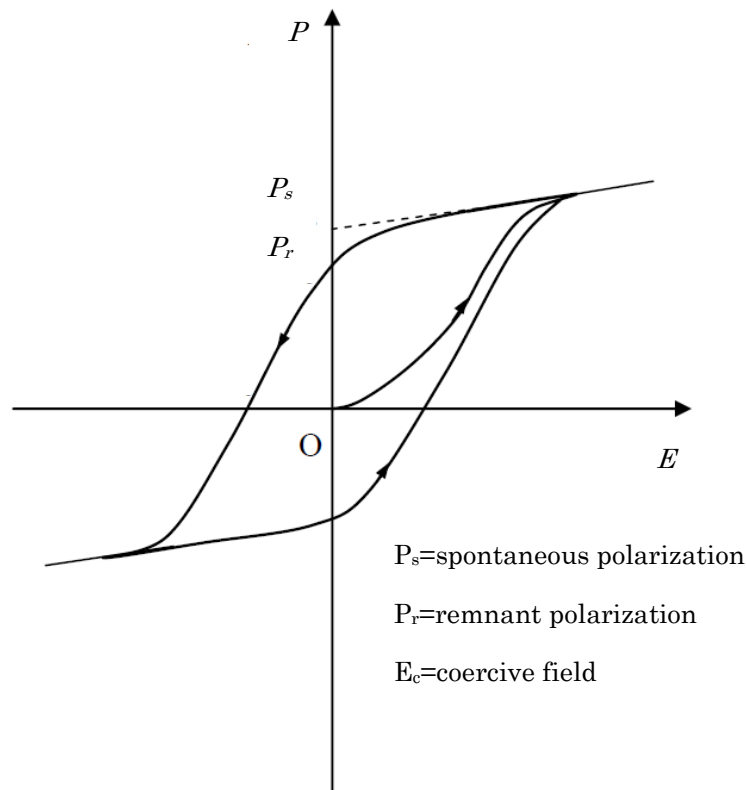
Fig. 1. 1. A typical Ferroelectrics *P-E* hysteresis loop.

One distinctive characteristic of Ferroelectrics is the hysteresis loop in the polarization vs. electric field curve. A net spontaneous polarization exists even at zero electric field and the loop disappears at the Curie temperature T_c, where the material undergoes a phase transition from low temperature ferroelectric to high temperature paraelectric states. In a paraelectric phase, the dielectric constant obeys Curie-Weiss law;

$$\varepsilon = \frac{C}{(T-T_c)}, \qquad \text{for } T > T_C \qquad (1.1)$$

where C and T_c are the Curie-Weiss constant and Curie-Weiss temperature, respectively.

In ferroelectric materials, four kinds of groups are well known on the basis of the unit cell structure: the tungsten-bronze group, the oxygen octahedral (ABO_3, Perovskite) group, the pyrochlore group and the bismuth layer-structure group [1.2-4]. Above all, the ABO_3 perovskites have attracted much attention due to various factors.

1. 2 Ferroelectric phase transition

A thermodynamic, or phenomenological, theory that is used extensively to describe a phase transition is the Landau free energy theory [1.2,4-6]. It is based on the polynomial thermodynamics potential expressed in terms of deviation from the prototype paraelectric state ($P_s = 0$). Again, an order parameter (P_s) measures the extent of the departure of the atomic (or electronic) configuration in the low symmetric phase (low temperature) from that high symmetric (high temperature) phase.

Following a basic Landau-Devonshire theory [1.7,8], one assume

$$G(P,T) = -EP + G_0 + \frac{1}{2}\alpha P^2 + \frac{1}{4}\beta P^4 + \frac{1}{6}\gamma P^6 + \cdots \qquad (1.2)$$

where the coefficients α, β, γ are the 2nd, 4th, and 6th dielectric stiffnesses.

For the second-order phase transition $\beta > 0$, $\gamma = 0$. For the first-order phase transition $\beta < 0$, $\gamma > 0$. The conditions for the stability of the system are

$$\frac{\partial G}{\partial P} = 0 \quad \text{and} \quad \frac{\partial^2 G}{\partial P^2} > 0, \qquad (1.3)$$

which gives one minimum above T_c while, two minima below T_c in the potential.

1. 2. 1 Second-order phase transition

Case $\beta > 0$. Since G is minimum for $\alpha > 0$ when $T \geq T_c$, and for $\alpha < 0$ when $T < T_c$, the sign of α must change at T_c. In the first approximation $\alpha = \alpha_0(T - T_C)$ with a constant $\alpha_0 > 0$, and the expansion of G is given by

$$G(T,P) = G_0 + \frac{\alpha_0(T-T_C)}{2}P^2 + \frac{\beta}{4}P^4 \qquad . \qquad (1.4)$$

We now find the polarization without an external electric field (E=0) form

$$\frac{\partial G}{\partial P} = E = \alpha P + \beta P^3 + \gamma P^5 = 0 \tag{1.5}$$

and from the first approximation condition, it holds that

$$P_s = 0 \text{ for } T > T_C, \quad P_s^2 = \frac{\alpha_0(T_C - T)}{\beta} \quad \text{for } T < T_C. \tag{1.6}$$

The static dielectric susceptibility ε is calculated from the equilibrium polarization. At constant temperature, differentiating P with respect to E,

$$\frac{\partial P}{\partial E} = \alpha_0(T - T_C) + 3\beta P^2 = \frac{1}{\varepsilon}, \tag{1.7}$$

ε is obtained as

$$\varepsilon = \frac{1}{\alpha_0(T - T_C)} \qquad\qquad \text{for } T > T_C \tag{1.8a}$$

$$\varepsilon = \frac{1}{2\alpha_0(T_C - T)} \qquad\qquad \text{for } T < T_C \tag{1.8a}$$

respectively. Eq. 1. 8a is same as the Curie-Weiss law. The second-order phase is well described as $|P_s|$ goes continuously to zero at T_c as Fig. 1. 2(b).

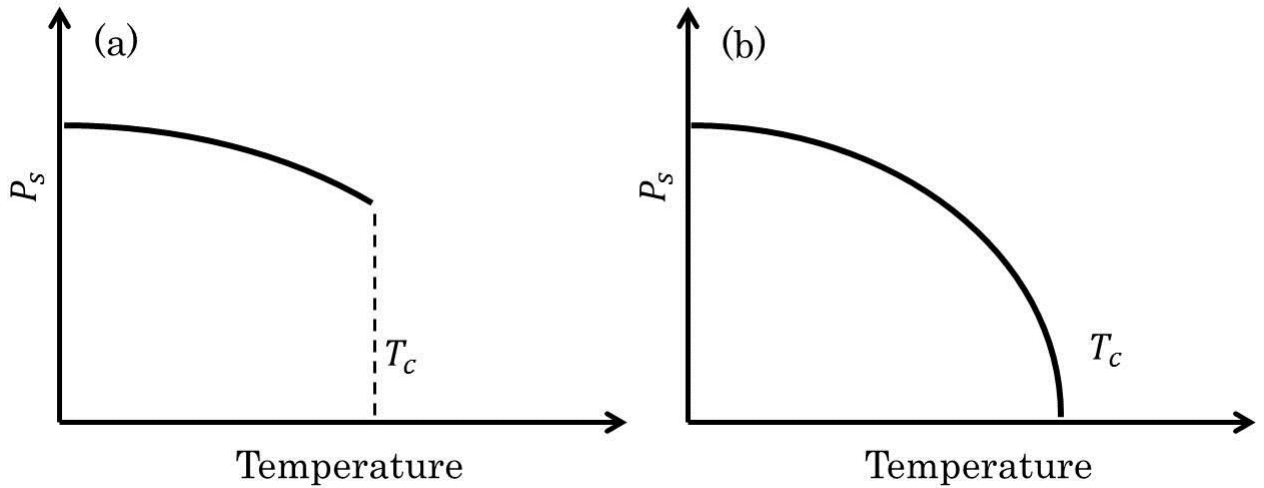Fig. 1. 2. P_s of a ferroelectric with a (a) first-order phase transition and (b) second-order phase transition.

1. 2. 2 First-order phase transition

Case $\gamma > 0$ and $\beta < 0$. Similarly to the pervious case, the stable states are given by

$$P_s = 0 \text{ for } T > T_C, \qquad P_s^2 = \frac{-\beta + (\beta^2 - 4\alpha_0\gamma(T - T_0))^{1/2}}{2\gamma}, \text{ for } T < T_C \tag{1.9}$$

3

T_0 is called the Curie-Weiss temperature and is not same to T_C. The obtained temperature dependence of P_s is shown in Fig. 1. 2(a). Contrary to the second-order phase transition, P_s disappear suddenly at T_c. In first-order phase transition, ε is obtained

$$\varepsilon = \frac{1}{\alpha_0 (T - T_0)} \qquad \text{for } T > T_C \qquad (1.\,10a)$$

$$\varepsilon = \frac{1}{4(T_0 - T)} \qquad \text{for } T < T_C \qquad (1.\,10a)$$

as shown in Fig. 1. 3.
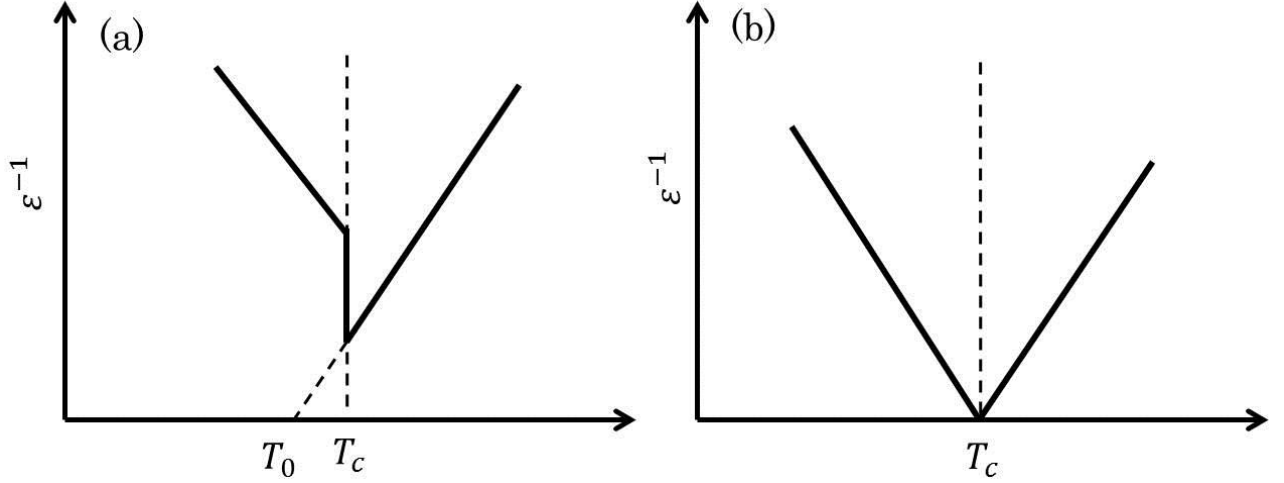
Fig. 1. 3. The Curie-Weiss law of (a) first-order and (b) second-order phase transitions.

1. 3 Displacive and order-disorder type phase transitions

In 1959 Cochran [1.9] showed that in weakly anharmonic systems, ferroelectric phase transitions are the result of instability of the lattice against a soft polar phonon at the centre of the Brillouin zone. Later, it is modified in terms of anharmonic lattice dynamics [1.10] and coupled order parameters.

For a second-order transition, we can write η (order parameter) as

$$\eta = \eta_0 (T_0 - T)^{1/2} \qquad (1.\,11)$$

assuming that η_0 is temperature independent.

The connection between a phonon frequency ω and the corresponding order parameter η follows from the equation of motion of a simple one-dimensional harmonic oscillator.

This write as

$$mω^2 = \frac{\partial^2 F}{\partial \eta^2} \qquad (1.\ 12)$$

where F is the oscillator potential and η corresponds to a small amplitude displacement.

Eg.1. 12 writes again as

$$\frac{\partial^2 F}{\partial \eta^2} = \alpha \qquad (1.\ 13)$$

then

$$ω = ω_0(T - T_0)^{1/2} \qquad (1.\ 14)$$

The temperature dependences of the order parameter and the soft-mode frequency given by Eqs. 1. 11 and 1. 14 imply that the particles move in mean field corresponding to the long range forces.

Expanding the free energy density G in a power series of P (from Eq. 1.2), we get

$$\frac{dP}{dt} = -\Gamma[\alpha_0(T - T_0)P + \beta P^3 + \gamma P^5]. \qquad (1.\ 15)$$

where Γ is a kinetic constant, expressing P as $\delta P + P_0$, and linearizing , we find

$$\frac{d(\delta P)}{dt} = -\Gamma[\alpha_0(T - T_0)P + 3\beta P_0{}^2 + 5\gamma P_0{}^4]\delta P, \qquad (1.\ 16)$$

The solution of this equation is

$$δP(t) = δP(0) \exp(-\frac{t}{τ}), \qquad (1.\ 17)$$

where the polarization time t is given by a product of the isothermal dielectric susceptibility

$$χ_T = [\alpha_0(T - T_0)P + 3\beta P_0{}^2 + 5\gamma P_0{}^4]^{-1} \qquad (1.\ 18)$$

and the inverse Landau kinetic coefficient;

$$τ = χ_T/\Gamma. \qquad (1.\ 19)$$

Because inverse $χ_T$ is proportional to $|T - T_C|$ for a second order transition, the polarization relaxation time diverges at T_C,

$$τ \to ∞ \quad \text{as} \quad |T - T_C|^{-1}. \qquad (1.\ 20)$$

This critical slowing down from the vanishing of the thermodynamic restoring force at T_C.

1. 4 Relaxor Ferroelectrics

Relaxor ferroelectrics (RFEs) (relaxors) are a special type of ferroelectrics which have been extensively investigated over the past 50 years with the aim of tailoring their physical properties. At the beginning relaxors have also been called dirty ferroelectrics as they exhibit a diffuse frequency-dependent phase transition over a temperature range. The broad and frequency dispersive behavior of the dielectric permittivity at T_m distinguishes relaxors from normal ferroelectrics (see Fig. 1. 4). Relaxors can be separated into two groups: (i) such that develop long-range ferroelectric order at T_c (Fig. 1. 4(b)), and (ii) canonical relaxors (Fig. 1. 4(c)) which do not show a macroscopic phase transition, therefore remain isotropic, *i.e.*, the polar-nano regions (PNR) or domains freeze at $T_f = T_{VF}$ resulting in a change of the translational symmetry.
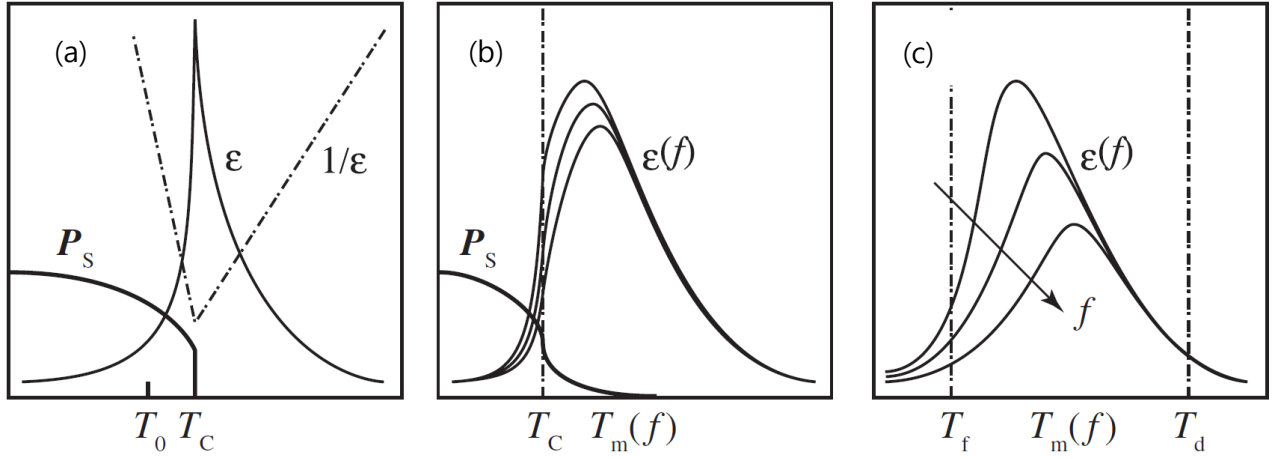
Fig. 1. 5. Behavior of the dielectric permittivity ε with respect to the different characteristic temperatures T_B, T_m, T_c, and T_f: in normal ferroelectrics (a), relaxors with a phase transition to ferroelectric (b), and canonical relaxors (c) [1.11].

In relaxor ferroelectrics, there are locally ordered nanoscale regions called chemically ordered regions (CORs) where 1:1 type B-site ordering is observed. CORs are known to be static, stable and independent of temperature. Another feature of relaxors is a PNR in which a local spontaneous polarization exists and its direction is flipping randomly by thermal fluctuations. Depending on the temperature evolution of PNRs, several characteristic temperatures can be defined and discussed. On cooling from very high temperature, RFEs show the deviation of the refractive index from the high temperature linear temperature dependence below the Burns temperature T_B[1.12], which is usually a few hundred degrees above the dielectric maximum temperature (T_m) or a Curie temperature (T_c). The dynamic PNRs appear at T_B and a normal dielectric state changes into an ergodic relaxor state. Recently strong acoustic emission signals were observed in Pb-based relaxors at an intermediate temperature T^* located between T_B and T_m. It was suggested that the onset of rapid growth in the size of PNRs and the local phase transformation in them may generate acoustic bursts at T^* [1.13]. The temperature

variation of characteristic relaxation times, usually estimated from dielectric dispersion, can be described by the Vogel-Fulcher law [1.14], and dynamic PNRs freeze into static PNRs at $T_{VF} = T_f$. These characteristic temperatures related to the temperature evolution of PNRs are summarized in Fig. 1. 6 [1.15-16].
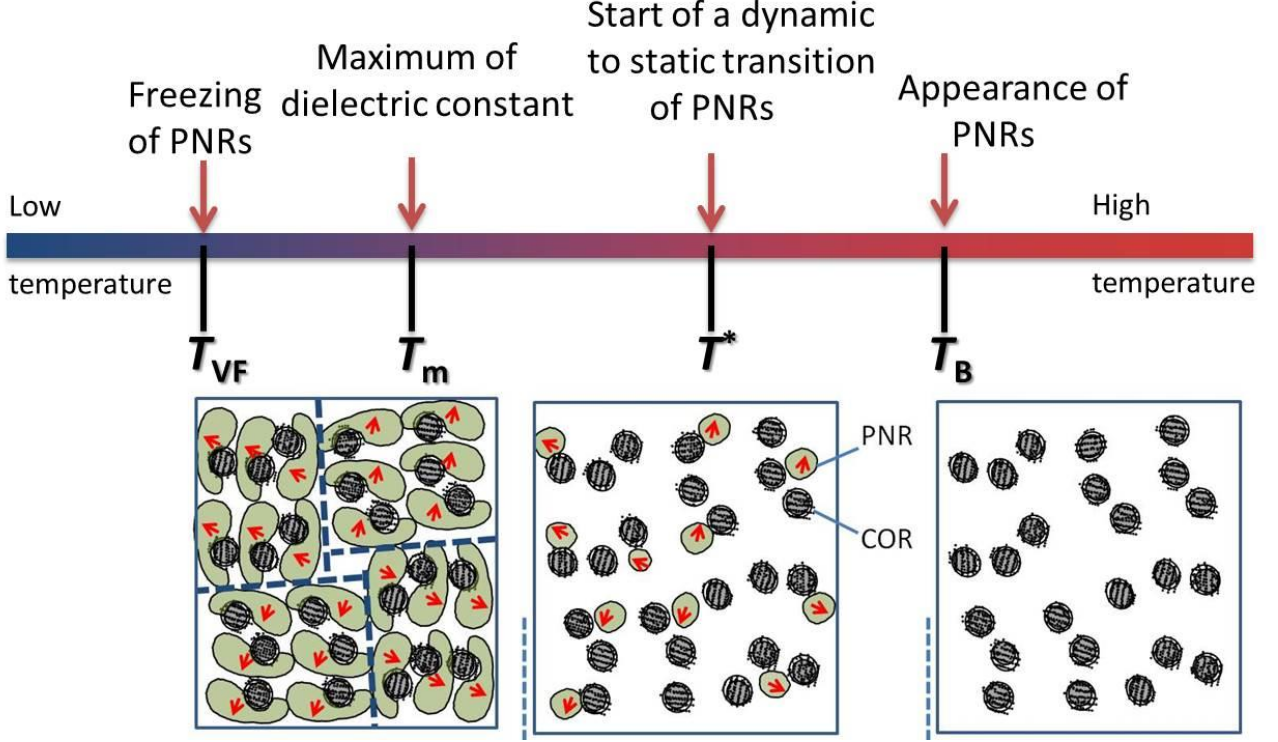
Fig. 1. 6. Temperature evolution of PNRs and characteristic temperature.

1. 5 Local symmetry of Relaxor Ferroelectrics

$Pb(B'_{1/3}B''_{2/3})O_3$ such as PbZn$_{1/3}$Nb$_{2/3}$O$_3$ (PZN) and PbMg$_{1/3}$Nb$_{2/3}$O$_3$ (PMN) has a perovskite structure with (on average) a cubic $P_{m\bar{3}m}$ symmetry, with B'^{2+} and B''^{5+} ions interchanging on B sites. Measurements of the dielectric constant show that the crystal does not undergo a sharp transition to a ferroelectric phase. Instead, the dielectric constant exhibits a broad maximum. Below T_B, it deviates from Curie-Weiss law and exhibits strong frequency dispersion. The structure of $Pb(B'_{1/3}B''_{2/3})O_3$ is not homogeneous. If B' and B'' occupation ratio was uniformly and ideally equal (1:2) throughout the crystal, it would have a rhombohedral symmetry ($R3m$). But, a network of superstructure clusters with face-centered cubic symmetry ($F_{m\bar{3}m}$) destroys the picture. The size of these clusters is of the order of 2~3 nm in PMN [1.17]. The most widely accepted hypothesis, so-called "space charge model,"

associates the $F_{m\bar{3}m}$ clusters with antiferroelectrically ordered regions [1.18] where the Mg:Nb occupation ratio is equal to 1:1, *i.e.*, with local composition PMN [1.19]. Such 1:1 clusters carry an excessive negative charge, which is compensated by the positively charged host matrix. The network of such charges acts as a source of random fields. From diffuse neutron scattering in PMN [1.20], the polarzation inside a PNR has been reported to align along the eight equivalent [111]c.

Table 1. I. Symmetry and size of average structure and local structures

Origin	symmetry	size
Average structure	$P_{m\bar{3}m}$	-
PNRs	$R3m$	7~20 nm(below T_B)
COR	$F_{m\bar{3}m}$	below 5 nm

1. 6 Review of various models of relaxor ferroelectrics

1. 6. 1 Dipolar glass model

The nonequilibrium dipolar glassy state of relaxors is characterized by two temperatures, T_B, Burns temperature (or dipole temperature and T_f), freezing temperature. The relaxors exhibits glassy behavior between these two characterization temperatures. However, these two characterization temperatures are different from follow evidence. It is interesting to put them together, although they are proposed independently. Burns and Dacol [1.12] made comprehensive study on materials with both complex perovskite structure and tungsten bronze structure by accurate measurement of optical refractive index, thermal expansion, and Raman scattering. They found that up to hundreds degrees above T_m, where the index deviates from a high temperature linear behavior, a local random polarization (or glassy dipolar) still exist in the relaxor system. In the temperature range from T_m to T_B, the average polarization $\bar{P}$ is zero, but the $\sqrt{P^2}$ is not zero. Burns and Dacol reported the idea of composition fluctuations is transformed.

The dipolar glass model was extended by Viehland *et al.* [1.14] as superparaelectric model to account for polar cluster interaction in analogy to magnetic spin glass. By fitting the frequency and temperature dependent dielectric constants with Vogel-Fulcher relation

$$f = f_0 \exp[-\frac{E}{k_B(T_m - T_f)}] \qquad\qquad (1.\,21),$$

8

where T_f is the freezing temperature, E the activation energy, f_0 the Debye frequency. The extrapolated values of freezing temperature usually are very close to temperature of the collapse in the remnant polarization. The fundamental difference between glassy dipole freezing and thermal localization process in superparaelectrics is that freezing is a cooperative performance, while the thermal localization is an independent behavior. This cooperative performance is believed to be an indication of interactions between polar regions.

These models successfully explained the polar dynamics and their extreme slowing down at the diffuse phase transition. However, they are not capable of describing the ferroelectric symmetry breakdown on a nanometric scale [1.21]. The Vogel-Fuclcher relation is not the only one that can describe the frequency and temperature dependence dielectric constants. A superexponential function proposed [1.22] also can fit well with experiment results in the range of its physical significance, though the physical origin is unclear.

1. 6. 2 Random field model

A spherical cluster glass model or spherical random-bond-random-field (SRBRF) model involving both random bonds and quenched random fields has been recently proposed [1.23]. In this model, relaxor ferroelectric is regarded as an intermediate state between dipole glasses and normal ferroelectrics. In contrast to dipolar glasses, where elementary dipolar moments exist on the atomic scale, the relaxor state is characterized by the presence of nanoscale polar cluster of variable sizes. This picture constitutes the basis of the superparaelectric model [1.24] and of the more recent reorientable polar cluster model of relaxor [1.25]. The long range frustrated intercluster interaction of a spin-glass type is also taken into account into this picture. The system can be described by the pseudospin Hamiltonian:

$$\text{H} = -\sum_{ij} J_{ij} P_i P_j - \sum_i h_i P_i. \qquad (1.22)$$

Here the first sum is the interaction between the dipole moments (pseudospin) P at lattice site i and j that are coupled by interaction constants J_{ij} with Gaussian distribution. The second sum denotes the interaction of the dipole moments P_i (pseudospin) with quenched random field h_i, where $\sum h_i = 0$, but $\sum h_i^2 \neq 0$. The electric dipoles random distributed in the system were treated as the main souses of random fields.

This model is capable of elucidating the static behavior of relaxors, such as the line shape of quadrapole nuclear magnetic resonance (NMR) in PMN [1.23]. This model has been extended to describe the dynamic of relaxor ferroelectrics by introducing Langevin-type equation of motion [1.26]

1. 7 Domain engineering

A domain-engineered crystal is one which has been poled by the application of a sufficiently high field along one of the possible polar axes of the crystal other than the zero field polar axis, creating a set of domains in which the polarizations are oriented such that their angles to the poling direction are minimized [1.27]. Therefore, in a perovskite material, there are three possible sets of poling directions [111]c, [101]c, and [001]c (if monoclinic phases are ignored). These directions correspond, respectively, to the polar axes of rhombohedral (R, point group $3m$), orthorhombic (O, $mm2$) and tetragonal (T, $4mm$) crystal phases. According to the definition, this results in six possible domain-engineered structures, formed by cutting and poling a perovskite crystal along certain directions; these are listed in Table 1. II. Also given are the three possible monodomain structures $1R$, $1C$, and $1T$ formed by poling a perovskite crystal along its polar axis.

Table 1. II. Engineered and monodomain states in perovskite single crystals [1.28].

Crystal	Polar direction	Poling direction	Polar directions for the resultant set of equivalent domainvariants	Domain-Engineered structure
Rhombohedral	[111]c	[111]c	[111]c	1R
		[101]c	[1-11]c,[111]c	2R
		[001]c	[111]c,[11-1]c,[1-11]c,[1-1-1]c	4R
Orhorhombic	[101]c	[111]c	[101]c,[011]c,[110]c	3O
		[101]c	[101]c	1O
		[001]c	[101]c,[011]c,[-101]c,[0-11]c	4O
Tetragonal	[001]c	[111]c	[001]c,[010]c,[100]c	3T
		[101]c	[001]c,[100]c	2T
		[001]c	[001]c	1T

References

[1.1] J. Valasek, Phys. Rev., **17** (1921) 475.

[1.2] M. E. Line and A. M. Glass, *Principles and Applications of Ferroelectrics and Related Materals*, Clarendon, Oxford 1977).

[1.3] B. Jaffe, W. R. Cook Jr. and H. Jaffe, *Piezoelectric ceramics*, (Academic, London 1971).

[1.4] R. Blinc and B. Zeks, *Soft Modes in Ferroelectrics and Antiferroelectrics*, (North-Holland, Amsterdam, 1983).

[1.5] H. Z. Cummins and A. P. Levanyuk, *Light scattering near phase transitions*, (North-Holland, Amsterdam 1983).

[1.6] A. K. Muller and H. Thomas, *Structural phase transtion* I, (Springer-Verlag, New York 1981).

[1.7] A. F. Devonshire, Adv. Phys., **3** (1954) 85.

[1.8] C. Kittel, *Introduction to Solid State Physics* 8th, (Wiley, 2005).

[1.9] W. Cochran, Phys. Rev. Lett., **3** (1959) 412.

[1.10] A. R. Cowley, Adv. Phys., **12** (1963) 421.

[1.11] K. Hirota, S. Wakimoto, and D. E. Cox, J. Phys. Soc. Jpn., **75** (2006) 111006.

[1.12] G. Burns and F. H. Dacol, Phys. Rev. B, **28** (1983) 2527.

[1.13] E. Dul'kin, M. Roth, P.-E. Janolin, and B. Dkhil, Phys. Rev. B, **73** (2006) 012102.

[1.14] D. Viehland, S.J. Jang, L.E. Cross, and M. Wuttig, J. Appl. Phys., **68** (1990) 2916.

[1.15] S. Kojima and J. –H. Ko, Curr. Appl. Phys., **11** (2011) S22.

[1.16] D. Fu, H. Taniguchi, M. Itoh, S. –Y, Koshihara, N. Yamamoto, and S. Mori, Phys. Rev. Lett., **103** (2009) 207601.

[1.17] J. Chen, H.M. Chan, and M.P. Harmer, J. Am. Ceram. Soc., **72** (1989) 593.

[1.18] S. Miao, J. Zhu, X. Zhang, and Z.-Y. Cheng, Phys. Rev. B, **65** (2001) 052101.

[1.19] E. Husson, M. Chubb, and A. Morell, Mater. Res. Bull., **23** (1988) 357.

[1.20] G. Xu, G. Shirane, J. R. D. Copley, and P. M. Gehring, Phys. Rev. B, **69** (2004) 64112.

[1.21] N. de. Mathan, E. Husson, G. Calvarin, J. R. Gavarri, A. W. Hewat, and A. J. Morell, J. Phys.: Condens. Matter, **3** (1991) 8159.

[1.22] Z. Y. Cheng, L. Y. Cheng, and X. Yao, J. Appl. Phys., **79** (1996) 8615.

[1.23] R. Pirc, and R. Blinc, Phys. Rev. B, **60** (1999) 13470.

[1.24] L. E. Cross, Ferroelectrics, **76** (1987) 241.

[1.25] B. E. Vugmeister and H. Rabitz, Phys. Rev. B, **57** (1998) 7581.

[1.26] R. Pirc, R. Blinc, and V. Bobnar, Phys. Rev. B, **63** (2001) 054203.

[1.27] A. J. Bell, J. Appl. Phys., **89** (2001) 3907.

[1.28] M. Davis, D. Damjanovic, D. Hayem, and N. Setter, J. Appl. Phys., **98** (2005) 014102.

Chapter 2. Inelastic Light Scattering Spectroscopy

2. 1 Light scattering

Light is scattered by fluctuations in the dielectric tensor in a material. Fluctuations of certain physical quantities are coupled to the fluctuations in the dielectric tensor. Near a phase transition point, the fluctuations of some of these quantities are enhanced. Most of all, inelastic light scattering is one of the powerful tools for the study of both the dynamic properties and phenomena of a phase transition [2.1-5].

The inelastic scattering of light by long wavelength acoustic phonons gives rise to the Brillouin spectra, whereas the scattering by optical phonons results in Raman spectra. A large number of ferroelectric soft modes, which become unstable at Brillouin zone center, have been studied by observing these inelastic components in the light scattering [2.2]. In addition, the peak in the center of the spectrum is the contribution of incident photons that have been elastically or quasi-elastically scatted with no change in frequency. These are called Rayleigh scattering or central peak. Fig. 2. 1 gives the frequency spectrum of scattered light in the three distinct frequency region [2.1].
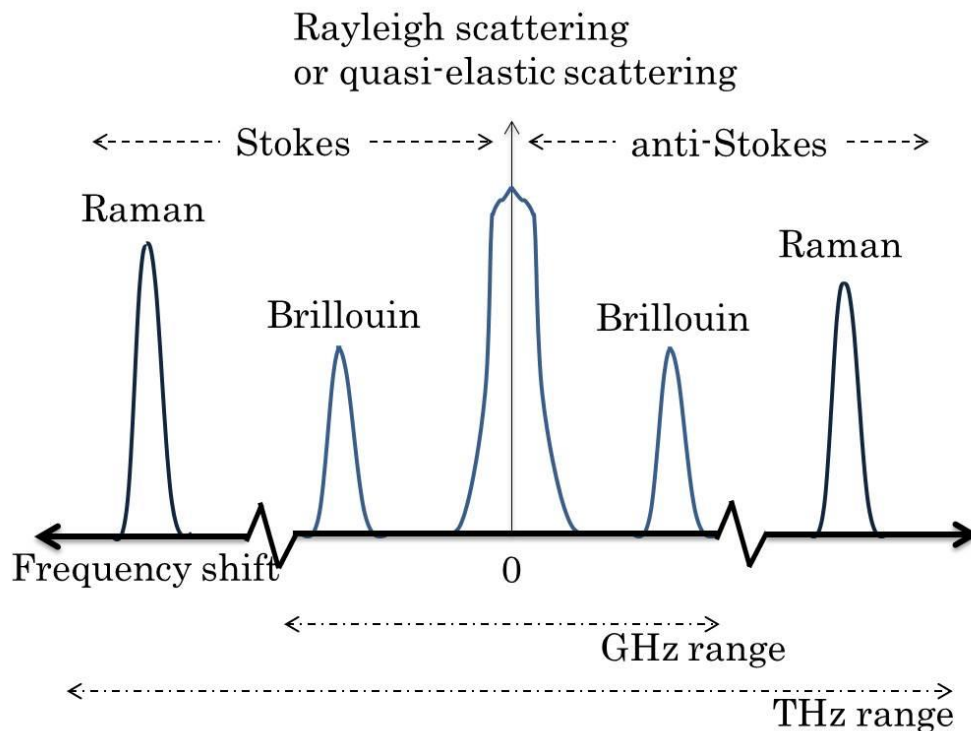
Fig. 2. 1. Schematic light scattering spectra

The classical theory of light scattering in dense media developed by Einstein [2.6] and Smoluchowski considers the sample as divided into small volume elements large enough to contain many molecules, but of linear dimension small compared to the wavelength of light. An incident light wave induces a dipole moment in each volume element, which becomes the source of scattered radiation [2.7]. Provided that the induced polarization is constant through the medium, the scattered radiation in all directions but the forward will be zero due to destructive interference, because the wavelets scattered from each sub-region differ only by a phase factor that depends on the relative position of the small volumes. Therefore, neglecting small surface effects, it is possible to pair each small volume with another small one whose scatted field is identical in amplitude, while opposite in phase, this they cancel out [2.8].

However, in real media, especially relaxor, there will be always small random fluctuations in the local dielectric constant due to the thermal motion of the atoms and molecules in the sample. Because these fluctuations should be uncorrelated from one volume element to the next, these regions are optically different. That means that now light is also scattered in other directions than forward due to only partial interference.

The local dielectric constant at a point at position $\mathbf{r}$ and time t, $\epsilon(\mathbf{r}, t)$, is generally described by the dielectric constant fluctuation tensor $\delta\epsilon(\mathbf{r}, t)$. It describes the relation between the local and the average dielectric constant ϵ_0;

$$\epsilon(\mathbf{r}, t) = \epsilon_0 \boldsymbol{I} + \delta\epsilon(\mathbf{r}, t), \tag{2.1}$$

where $\boldsymbol{I}$ is the (initial) dielectric constant second-rank tensor [2.9].

When the incident light is a plane wave with field amplitude E_0, angular frequency ω_i, and incident propagation vector $\boldsymbol{k}_i$, the incident electric field can be written as

$$\boldsymbol{E}_i(\boldsymbol{r}, t) = \boldsymbol{n}_i E_0 \exp i(\boldsymbol{k}_i \cdot \boldsymbol{r} - \omega_i t) \tag{2.2}$$

with $\boldsymbol{n}_i$ being the unit vector in the direction of the incident field.

At Large distance $\boldsymbol{R}$ from the scattering volume, the scattered electric field $\boldsymbol{E}_s(\boldsymbol{r}, t)$ can be obtained from the fact that the Maxwell equations must hold for the total electric field, the incident electric field and as well for the scattered electric field, where the total field is just the sum of the two others;

$$\boldsymbol{E} = \boldsymbol{E}_i + \boldsymbol{E}_s. \tag{2.3}$$

In the end it follows for the component of the scattered electric field $E_s(R, t)$ that

$$E_s(R, t) = \frac{E_0}{4\pi R \epsilon_0} \exp i k_s R \int_V d^3 r$$

$$\times \exp i(\boldsymbol{q} \cdot \boldsymbol{r} - \omega_i t [\boldsymbol{n}_s \cdot [\boldsymbol{k}_s \times (\boldsymbol{k}_s \times (\delta\epsilon(\boldsymbol{r}, t) \cdot \boldsymbol{n}_i)]], \tag{2.4}$$

where $\boldsymbol{n}_s$ is the polarization, $\boldsymbol{k}_s$ is the propagation vector, ω_s is the frequency of the scattered plane wave field that reaches the detector, and V indicates that the integral is over

the whole scattering volume. The scattering wave vector $\boldsymbol{q}$ is defined as the difference between incident and scattered propagation vector,

$$\boldsymbol{q} = \boldsymbol{k}_i - \boldsymbol{k}_s. \tag{2.5}$$

The angle between $\boldsymbol{k}_i$ and $\boldsymbol{k}_s$ is called the scattering angle θ as Fig. 2. 2.
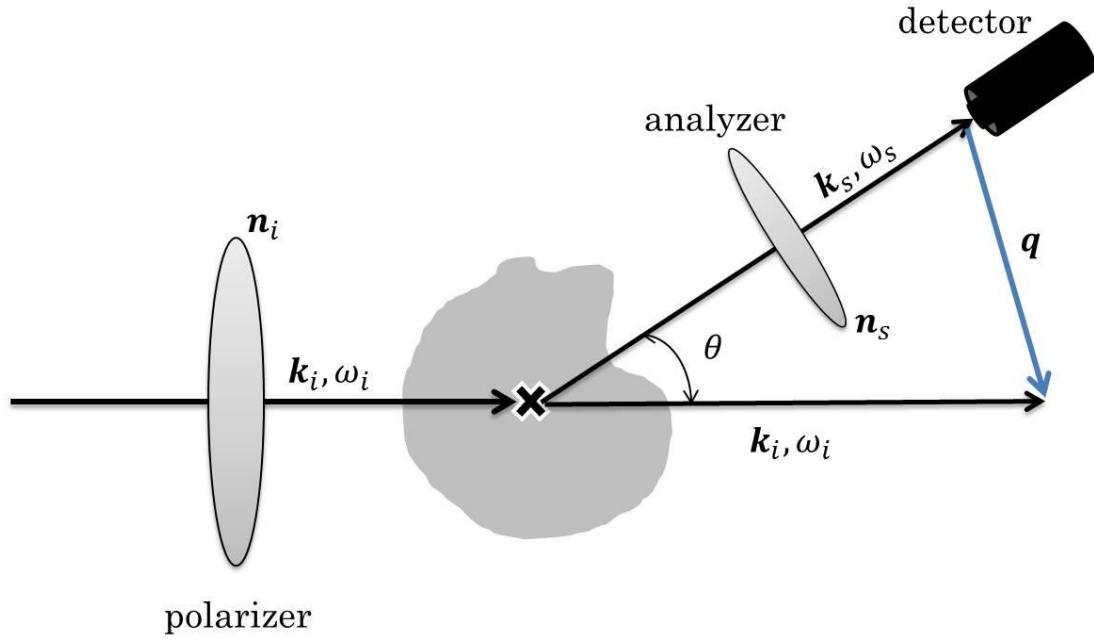

Fig. 2. 2. Light of polarization $\boldsymbol{n}_i$ and wave vector $\boldsymbol{k}_i$ is scattered in all directions. Only scattered light of wave vector $\boldsymbol{k}_s$ and polarization $\boldsymbol{n}_s$ arrives at the detector.

Fig. 2. 2 makes clear that the magnitude of the scattering wave vector $\boldsymbol{q}$ can be computed as

$$q^2 = |\boldsymbol{q}|^2 = k_i^2 + k_s^2 - 2\boldsymbol{k}_i \cdot \boldsymbol{k}_s. \tag{2.6}$$

When the scattering is quasi-elastic, the cosine rule becomes applicable and Eq. 2. 6 becomes

$$q^2 = k_i^2 + k_s^2 - 2\boldsymbol{k}_i \cdot \boldsymbol{k}_s = 2k_i^2(1 - \cos\theta) = 4k_i^2\sin^2\frac{\theta}{2}. \tag{2.7}$$

Or, with $k_s = k_i = 2\pi n/\lambda$, where the length of the incident wave vector is written as function of the refractive index n and the incident wave length λ;

$$q = 2k_i \sin\frac{\theta}{2} = \frac{4\pi n}{\lambda}\sin\frac{\theta}{2} \tag{2.8}$$

This is the Bragg condition.

Using the spatial Fourier transform of the dielectric fluctuation

$$\delta\epsilon(\boldsymbol{q},t) = \int_V d^3r \exp i\boldsymbol{q}\cdot\boldsymbol{r}\,\delta\epsilon(\boldsymbol{r},t),\qquad(2.9)$$

Eq. 2. 4 can be rewritten as

$$E_s(R,t) = \frac{E_0}{4\pi R\epsilon_0}\exp i(k_sR - \omega_i t)[\,\boldsymbol{n}_s\cdot[\boldsymbol{k}_s\times(\boldsymbol{k}_s\times(\delta\epsilon(\boldsymbol{r},t)\cdot\boldsymbol{n}_i))]].\qquad(2.10)$$

This can be simplified [2.8];

$$E_s(R,t) = \frac{-k_s^2 E_0}{4\pi R\epsilon_0}\exp i(k_sR - \omega_i t)\delta\epsilon_{is}(\boldsymbol{q},t),\qquad(2.11)$$

where

$$\delta\epsilon_{is}(\boldsymbol{q},t) \equiv \boldsymbol{n}_s\cdot\delta\epsilon(\boldsymbol{q},t)\cdot\boldsymbol{n}_i\qquad(2.12)$$

is the component of the dielectric constant fluctuation tensor along the initial and final polarization direction.

The time-correlated function of E_s can then be written as

$$< E_s^*(R,0)E_s(R,t) > = \frac{k_s^4|E_0|^2}{16\pi^2 R^2\epsilon_0^2} < \delta\epsilon_{is}(\boldsymbol{q},t) > \exp(-i\omega_i t).\qquad(2.13)$$

Then, the spectral density

$$I_E(\omega) = \frac{1}{2\pi}\int_{-\infty}^{+\infty}d\tau < E^*(t)E(t+\tau) > \exp(-i\omega_i\tau)\qquad(2.14)$$

of light reaching the detector with $\boldsymbol{n}_s$, $\boldsymbol{k}_s$, and ω_s can be computed as

$$I_{is}(\boldsymbol{q},\omega_s,R) = \left(\frac{I_0 k_s^4}{16\pi^2 R^2\epsilon_0^2}\right)\frac{1}{2\pi}\int_{-\infty}^{+\infty}dt < \delta\epsilon_{is}(\boldsymbol{q},0)\delta\epsilon_{is}(\boldsymbol{q},t) > \exp(i\omega t)\qquad(2.15)$$

with $I_0 \equiv |E_0|^2$ and

$$\omega \equiv \omega_i - \omega_s.\qquad(2.16)$$

The latter means that the spectral density (the intensity measured by the detector) depends only on the difference between the incident and the scattered frequency. Furthermore, from Eq. 2. 15 one can learn that $I_{is} \propto k_s^4$ and $I_{is} \propto R^{-2}$. The λ^{-4} dependence means that electromagnetic radiation with apparent in the blue color of the sky. The R^{-2} dependence is expected, because it just expresses the attenuation of spherical wave.

For a given experiment, the coefficient in Eq. 2. 15 becomes a constant, and the scattering intensity is then only affected by the spectral density of the dielectric constant fluctuations,

$$I_{is}(\boldsymbol{q},\omega) \propto \int_{-\infty}^{+\infty}dt < \delta\epsilon_{is}^*(\boldsymbol{q},0)\delta\epsilon_{is}(\boldsymbol{q},t) >.\qquad(2.17)$$

The integral of Eq. 2. 17 over frequency, the integrated intensity at all frequencies, provides

16

information about the q dependent mean-square fluctuation ϵ;

$$I_{is}(\boldsymbol{q}) = <|\delta\epsilon_{is}(\boldsymbol{q})|^2>. \qquad (2.18)$$

A light scattering event is produced by the creation or annihilation of a phonon as indicated in Fig. 2. 3.

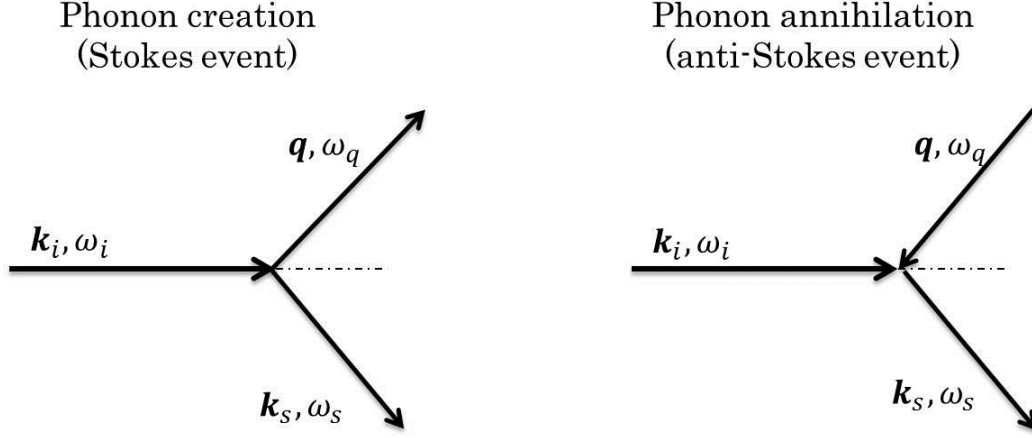| Phonon creation (Stokes event) | Phonon annihilation (anti-Stokes event) |

Fig. 2. 3. Diagrams for the first order photon-phonon scattering.

Conservation of energy and momentum between the photons and phonons yields for Stokes event;

$$\hbar\omega_s = \hbar\omega_0 - \hbar\omega_q,$$

$$\boldsymbol{k}_s = \boldsymbol{k}_0 - \boldsymbol{q}. \qquad (2.19)$$

For anti-Stokes event

$$\hbar\omega_s = \hbar\omega_0 + \hbar\omega_q,$$

$$\boldsymbol{k}_s = \boldsymbol{k}_0 + \boldsymbol{q}. \qquad (2.20)$$

The spectral power density of the scattered light is obtained from Eq. 2.15 by

$$I_{is}(\boldsymbol{q},\omega_s) \propto |\delta\epsilon_{is}(\boldsymbol{q},\omega)|^2 \propto [n(\omega)+1]\mathrm{Im}\chi_{is}(\boldsymbol{q},\omega), \qquad (2.21)$$

where the second identity is the fluctuation-dissipation theorem, χ_{is} is the dielectric susceptibility, $n(\omega)$ is the Bose-Einstein thermal factor at frequency ω and is given by

$$n(\omega) = \frac{1}{\exp\left(\frac{\hbar\omega}{kT}\right)-1} \qquad (2.22)$$

We note that the spectral intensity is proportional to the imaginary part of the dielectric susceptibility. It is very useful when analyze a spectrum.

17

2. 2 Raman scattering

Raman spectroscopy is now finding a very wide-ranging application in pure and applied sciences. Actually, Raman scattering is a fundamental form of molecular spectroscopy. Thus it is generally used to obtain information about the structure and properties of molecules from their vibrational transitions [2.10]. When applied in solid state physics, Raman spectroscopy is used to characterize materials, measure temperature, and find the crystallographic orientation of a sample. The measurement of the Raman spectra of a crystal is one of the main methods for obtaining information about its lattice vibration frequencies [2.11].

2. 2. 1 Origin of Raman scattering

Raman scattering is the inelastic scattering of a photon by molecular or crystal lattice vibrations, with either gain or loss in the incident photon energy and accordingly equal loss or gain in the scattering photon energy. The energy difference between the incident photon and the Raman scattered photon is equal to the energy level of a vibration of the scattering molecule. Note that the photon as a whole is never absorbed in Raman scattering, but rather perturbs the molecule and induce it to undergo a vibrational or rotational transition. Thus the Raman scattering doesn't involve the actual attainment of an excited intermediate level, but a virtual level, just like what Fig.2.3 shows. In practice, as a vibrational frequency has a value of the order of 10^{12} Hz. The resulting quantity is then a wavenumber in units of wave number cm^{-1}.

$$k(\text{cm}^{-1}) = \frac{\nu}{c}, \tag{2.23}$$

where ν and c indicate frequency shift (Hz) and the speed of light, respectively.

From the elementary classical theory derived by Ferraro *et al.* [2.10], we can know more clear about the origin of a Raman spectrum. Considering a diatomic molecule is irradiated by a monochromatic light wave with an electric component which is described as;

$$E = E_0 \cos 2\pi\nu_0 t \tag{2.24}$$

here E_0 is the intensity amplitude of the electric component and ν_0 is the wave frequency.

The effect of the electric field on a molecule is to polarize the electron distribution. Thus, a dipole moment is induced in the molecule. If the electric field is not too strong, the induced dipole moment M_d is given by:

$$M_d = \alpha E = \alpha E_0 \cos 2\pi\nu_0 t \tag{2.25}$$

where α is a proportionality constant and is called polarizability.

Assuming the binding effect of the electronic charge distribution of the diatomic molecule is approximated by a spring between its points like nuclei. Accordingly, the nuclei are space- and rotation-fixed about their equilibrium positions but free to vibrate in simple harmonic motion along one normal coordinate Q. If the molecule has a vibration with a frequency ν_1, the nuclear displacement Q can be written as

$$Q = Q_0 \cos 2\pi \nu_1 t \qquad (2.26)$$

where Q_0 is the vibrational amplitude. When the vibration amplitude is small, α is a linear function of Q and can be expanded as a Taylor series in Q:

$$\alpha = \alpha_0 + \left(\frac{\partial \alpha}{\partial Q}\right)_0 Q + \cdots \approx \alpha_0 + \left(\frac{\partial \alpha}{\partial Q}\right)_0 Q_0 \cos 2\pi \nu_1 t \qquad (2.27)$$

here α_0 is the polarizability of the molecule at the equilibrium position, and $\left(\frac{\partial \alpha}{\partial Q}\right)_0$ is the rate of change of α with respect to the change in Q, evaluated at the equilibrium position.

From Eq. 2.25 to 2.27, we can obtain;

$$M_d = \alpha_0 E_0 \cos 2\pi \nu_0 t + \left(\frac{\partial \alpha}{\partial Q}\right)_0 Q_0 E_0 \cos 2\pi \nu_0 t \cos 2\pi \nu_1 t$$

$$= \alpha_0 E_0 \cos 2\pi \nu_0 t + \frac{1}{2}\left(\frac{\partial \alpha}{\partial Q}\right)_0 Q_0 E_0 [\cos\{2\pi(\nu_0 + \nu_1)t\} + \cos\{2\pi(\nu_0 - \nu_1)t\}]. (2.28)$$

The vibrating molecule can therefore be the source of scattered radiation. In the Eq. 2.28, the first term represents an oscillating dipole that radiates light of frequency ν_0 (Rayleigh scattering), while the second term corresponds to the Raman scattering of frequency $\nu_0 + \nu_1$ (anti-Stokes component) and $\nu_0 - \nu_1$ (Stokes component) which can be observed in any particular direction. The second term vanishes when $\left(\frac{\partial \alpha}{\partial Q}\right)_0$ is zero. That is to say, to be Raman-active, the rate of change of polarizability (α) with the vibration must not be zero.

3. 2. 2 Polarization in crystals

The polarizability of the crystal is anisotropic, *i.e.* different for different directions in space. Thus, it can be given in the form of the polarizability tensor related to the rectangular spatial coordinate system (*i, j=x, y, z*);

$$\alpha_{ij} = \begin{bmatrix} \alpha_{xx} & \alpha_{xy} & \alpha_{xz} \\ \alpha_{yx} & \alpha_{yy} & \alpha_{yz} \\ \alpha_{zx} & \alpha_{zy} & \alpha_{zz} \end{bmatrix}. \qquad (2.29)$$

The polarizability tensor is symmetrical, i.e. $\alpha_{ij} = \alpha_{ji}$. Hence the number of distinct components is reduced to six. According to Eq.2.28, if any one of the $\left(\frac{\partial \alpha}{\partial Q}\right)_0$ in six polarization

tensor components is non-zero, a Raman spectrum can be observed. The rate of change of the polarizability $\left(\frac{\partial^2 \alpha}{\partial Q^2}\right)_K$ also is a tensor of second order called Raman tensor for the Kth mode. For each vibrational mode is associated such a tensor $\left(\frac{\partial \alpha}{\partial Q}\right)_K$; its general form depends upon the symmetry of the mode characterized by an irreducible representation of the point group of a crystal [2.4].

In present thesis, the back scattering geometry is employed, as shown in Fig.2. 4. The laser beam (incident light) is directed along the Z axis, and the scattered light in the –Z direction is collected. Both excitation and scattering are assumed to be in the form of parallel beams of light. The excitation light is assumed to be polarized in the Y direction and the polarization of the scattered light can be chose in either the X or the Y direction with the use of an analyzer. The orientation of a single crystal in a given Raman experiments is generally specified by the Porto notation [2.12]. Three directions x, y and z in the crystal are defined which are not necessarily coincident with the crystallographic axes. If the crystal is oriented so that the axes x, y, z are collinear with the space-fixed axes X, Y, Z. Thus the two configurations described in Fig.2.4 are represented by $z(yy)\bar{z}$ and $z(yx)\bar{z}$, the former is generally called VV scattering geometry, while the latter is called VH scattering geometry. In the Porto notation, the first symbol defines the direction of propagation of the incident light, while the last one refers to the observation direction, i.e. the propagation of the scattered light. The symbols in parentheses specify, in order, the polarization directions of the incident and scattered light.
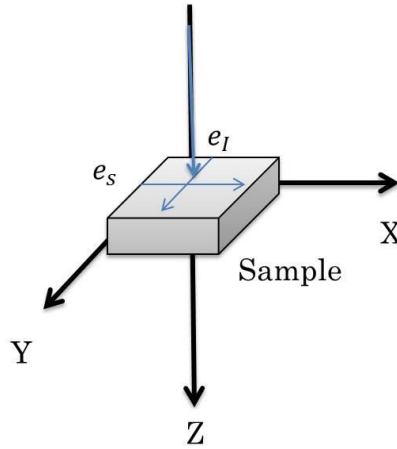

Fig 2. 4. The back scattering geometry usually used in Raman scattering.

In literature, phonon modes are addressed to in several ways. Group theory analysis, which refers to phonon modes as irreducible representations, often uses the so called Mulliken symbols (see Table 3.1). Here the capital letters gives information about the degeneration, i.e., if two different vibrations have the same frequency thus being equal in phonon energy, while the subscripts g and u describe whether the modes are symmetric (g) and anti-symmetric (u) with respect to the center of inversion. The subscripts 1 and 2 denote whether the mode is

symmetric or anti-symmetric upon rotation about the center of the atom, while the superscript ' and '' denote whether the mode is symmetric or anti-symmetric with respect to a mirror plane horizontal to the principal rotational axis.

Table 2.1. Irreducible representations of phonon modes

Mode designation	Description
A	non-degenerated (single) symmetric mode, with respect to the principle rotation axis n
B	non-degenerated (single) anti-symmetric mode, with respect to the principle rotation axis n
E	doubly degenerated only in uniaxial and cubic crystals
F or T	triply degenerated (occurs only in lattices with cubic symmetry)

2. 2. 3 Group theoretical analysis and Raman peak assignment for Pb-based perovskite relaxors

As described in chapter 1 the ideal perovskite structure is $Pm\bar{3}m$ though if two B-site cations are present chemical 1:1 ordering of the structure can lead to a doubling of the unit cell and results in face-centered cubic symmetry $Fm\bar{3}m$ [2.13]. For such symmetries and the occupied Wyckoff positions in the perovskite structure the corresponding phonon modes at the Γ point of the Brillouin zone are given in Table 3.2. The letters R, IR, and I stand for Raman-active, IR-active and silent mode, respectively.

Table 2.2. Wyckoff positions and corresponding phonon modes

Atoms	Wyckoff position, $Pm\bar{3}m$	Phonon mode, $Pm\bar{3}m$ acoustic	optic
A	1a	F_{1u}	
B	1b		$F_{1u}(IR)$
O	3c		$2F_{1u}(IR) + F_{1u}(I)$
Atoms	Wyckoff position, $Fm\bar{3}m$	Phonon mode, $Fm\bar{3}m$ acoustic	optic
A	8c	F_{1u}	$F_{2g}(R)$
B′	4a		$F_{1u}(IR)$
B″	4b		$F_{1u}(IR)$
O	24e		$A_{1g}(R) + E_g(R) + 2F_{1u}(IR) + F_{1g}(I) + F_{2g}(R) + F_{2u}(I)$

The F_{1u}(irreducible representation associated to A-site cations) was assigned to the acoustic vibration because Pb is the heaviest element in the structure, i.e., it should generate low-wavenumber vibrations. Symmetry analysis cannot distinguish between IR active and

acoustic modes and therefore this distinction has to be made on the basis of physics. As there are always 3 acoustic modes and the wavevector should be small the heaviest atom is the most likely to generate this mode. Though only a small degree of chemical B-site ordering or none has been detected in RFE. TEM analysis has shown that the spectra should be interpreted in terms of doubled perovskite structure [2.13, 14]. Therefore, on the local scale B-site chemical ordering is always present, which is typical of all Pb-based relaxors with mixed B-site cations. The selection rules and polarizability tensors for the cubic $Fm\overline{3}m$ it is possible to assign the four allowed Raman-active modes (A_{1g} + E_g + $2F_{2g}$) to the Raman spectra [2.13]. The assignment of the allowed Raman active modes is given in Table 2.3.

Table 2.3. Mode assignment for the symmetry-allowed Raman active modes in $Fm\overline{3}m$ [2. 15].

Mode	(Approximate wave number)	Phonon vibration
A_{1g}	800 cm^{-1}	symmetric BO$_6$ stretching
E_g	600 cm^{-1}	symmetric B-O stretching
F_{2g}	350 cm^{-1}	O-B-O symmetrical bending
F_{2g}	45 cm^{-1}	Pb vibrations

It is widely believed that PNRs make peaks appear static to Raman spectroscopy, which is sensitive to dynamic phenomena with lifetimes larger than the period of phonon oscillations, which is ~ 10^{-12}s. Thus it is not unexpected to see a contribution of the PNRs in the Raman spectra as this is sensitive to intermediate- and short range order. Those Raman bands that could be assigned to the expected Raman-active modes are caused by the local distortions in the structure with $R3m$ by the PNRs [2.13,16].

2. 3 Brillouin scattering

2. 3. 1 Elastic waves in condensed matter

In this part, fundamental concepts of the theory of elasticity are introduced, following mostly the notation of the textbook of Nye [2.9].

Essential terms are the strain and stress tensors. To introduce them, we first define the displacement vector $\boldsymbol{u}$ that shifted a point P that can be found by following the vector $\boldsymbol{r}$ from the origin coordinate system to the point P' with coordinates given by the vector $\boldsymbol{r}'$, i.e.,

$$\boldsymbol{u} = \boldsymbol{r} - \boldsymbol{r}' \tag{2.30}$$

The distance between any two infinitesimally adjacent points dl is given by

$$dl=\sqrt{dx_1^2 + dx_2^2 + dx_3^2}=\sqrt{dx_i^2} \qquad (2.31)$$

using the Einstein summation convention behind the second equal. After a deformation it becomes

$$dl'=\sqrt{dx'^2_1 + dx'^2_2 + dx'^2_3}=\sqrt{dx'^2_i} \qquad (2.32)$$

Therefore, it is possible to write

$$dl^2=dx'^2_i = (dx_i + du_i)^2=dl^2 + 2\frac{\partial u_i}{\partial x_k}dx_i dx_k + \frac{\partial u_i}{\partial x_k}\frac{\partial u_i}{\partial x_l}dx_k dx_l \qquad (2.33)$$

substituting $du_i=\frac{\partial u_i}{\partial x_k}dx_k$ in the last step. With $\frac{\partial u_i}{\partial x_k}dx_i dx_k = \frac{\partial u_k}{\partial x_i}dx_i dx_k$ and swap of i and l in the last term, finally we get

$$dl'^2=dl^2 + 2u_{ik}dx_i dx_k. \qquad (2.34)$$

The strain tensor u_{ik} is defined as

$$u_{ik} = \frac{1}{2}\left(\frac{\partial u_i}{\partial x_k} + \frac{\partial u_k}{\partial x_i} + \frac{\partial u_l}{\partial x_k}\cdot\frac{\partial u_l}{\partial x_i}\right) \approx \frac{1}{2}\left(\frac{\partial u_i}{\partial x_k} + \frac{\partial u_k}{\partial x_i}\right). \qquad (2.35)$$

The last approximation is valid, if second order terms can be neglected. Obviously, u_{ik} is a symmetric tensor. Each symmetric tensor can be diagonalized in any point. With the diagonal elements $u^{(1)}$, $u^{(2)}$, $u^{(3)}$ the strain in any point can be written as the sum of three independent terms, which give the strain in three orthogonal main directions.

$$dl'^2 =(1+2u^{(1)})dx_1^2 + \left(1 + 2u^{(2)}\right)dx_2^2 + \left(1 + 2u^{(3)}\right)dx_3^2. \qquad (2.36)$$

For $u^{(i)} \ll 1$ and if higher order terms are neglected, the relative change of elongation becomes

$$\frac{dx'_i-dx_i}{dx_i}=\sqrt{1 + 2u^{(i)}} - 1 \approx u^{(i)}. \qquad (2.37)$$

With that approximation we can write the relative volume change of an infinitesimal small volume element $dV\rightarrow dV'$ as the sum of the diagonal elements of the strain tensor [2.9].

$$\frac{dV'-dV}{dV} = u_{ii}. \qquad (2.38)$$

The resulting force $\boldsymbol{F}$ on any partial volume of an elastic body can be written as the integral over the forces on any element of the volume $\int \boldsymbol{F}dV$. Because of the identity of action and reaction for all forces between any two points within the volume the resulting force can also be written as the sum over the integrals of the three components F_i, $\int \boldsymbol{F}dV$, which can be translated into an integral over the surface;

$$\int \pmb{F_i} dV = \int \frac{\partial \sigma_{ik}}{\partial x_i} dV = \oint \sigma_{ik} df_k. \qquad (2.39)$$

Here, $\pmb{F_i}$ is expressed as divergence of a second rank, the stress tensor σ_{ik};

$$F_i = \frac{\partial \sigma_{ik}}{\partial x_i} \qquad (2.40)$$

In Eq. 2.39, df_i are the components of a vector that is always oriented in the direction normal to the surfaces. The nature of the stress tensor is visualized in the coordinate system, the component σ_{ab} of the stress tensor equals to the a-component of the force that is normal to that x_b-axis.
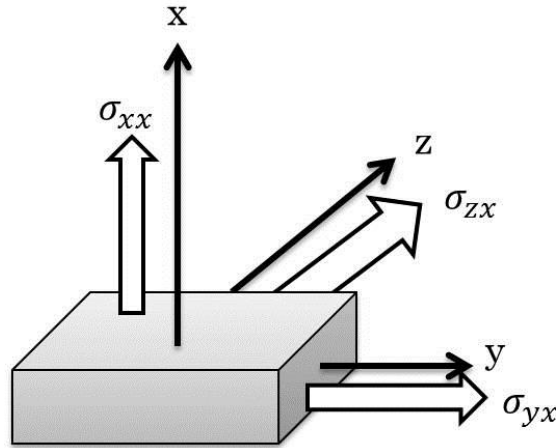

Fig 2. 5. Illustraion of the stress tensor for the σ_{ax}-components working on a surface normal to the x-aixs.

The work δw that is achieved to perform a deformation is

$$\delta w = -\sigma_{ik} \delta u_{ik}. \qquad (2.41)$$

For reversible, elastic deformations it follows for the free energy A ($A=U - TS$) that

$$\sigma_{ik} = \left(\frac{\partial A}{\partial u_{ik}}\right)_T. \qquad (2.42)$$

For a perfectly elastic body, Hook's law can be generalized to state that each component of the stress tensor is linearly related to each component of the strain tensor;

$$\sigma_{ik} = c_{iklm} u_{lm}. \qquad (2.43)$$

Here, c_{iklm} is the fourth-rank stiffness tensor with 81 components. Taking into account the symmetry of the strain and stress tensors, it is possible to reduce the number of coefficients to 36. However, these 36 components are not independent. In the general case the following symmetry relations are valid:

$$c_{iklm} = c_{kilm} = c_{ikml} = c_{kiml} \tag{2.44}$$

That is in an anisotropic body there are at most 21 independent components, which are usually noted in a matrix notation, which uses the itemized identities to abbreviate the tensor notation and to replace the tensor by a 6×6 matrix with only two indices per component. By matrix notation, one can rewrite Eq. 2.43 as

$$\begin{bmatrix} \sigma_1 \\ \sigma_2 \\ \sigma_3 \\ \sigma_4 \\ \sigma_5 \\ \sigma_6 \end{bmatrix} = \begin{bmatrix} C_{11} C_{21} C_{31} C_{41} C_{51} C_{61} \\ C_{12} C_{22} C_{32} C_{42} C_{52} C_{62} \\ C_{13} C_{23} C_{33} C_{43} C_{53} C_{63} \\ C_{14} C_{24} C_{34} C_{44} C_{54} C_{64} \\ C_{15} C_{25} C_{35} C_{45} C_{55} C_{65} \\ C_{16} C_{26} C_{36} C_{46} C_{56} C_{66} \end{bmatrix} \begin{bmatrix} u_1 \\ u_2 \\ u_3 \\ u_4 \\ u_5 \\ u_6 \end{bmatrix} \tag{2.45}$$

While the discussion of the stiffness matrix for different crystal symmetries is done in specialized treatments, here only the isotropic case, which is a good approximation for many cases, including also most polymer systems, should be discussed in the rest of this section. For an isotropic body, it can be shown that due to further symmetry considerations the stiffness matrix in Eq. 2.43 has the following form [2.4];

$$\begin{bmatrix} \sigma_1 \\ \sigma_2 \\ \sigma_3 \\ \sigma_4 \\ \sigma_5 \\ \sigma_6 \end{bmatrix} = \begin{bmatrix} C_{11} C_{21} C_{31} & 0 & 0 & 0 \\ C_{12} C_{22} C_{32} & 0 & 0 & 0 \\ C_{13} C_{23} C_{33} & 0 & 0 & 0 \\ 0 & 0 & 0 & C_{44} & 0 & 0 \\ 0 & 0 & 0 & 0 & C_{55} & 0 \\ 0 & 0 & 0 & 0 & 0 & C_{66} \end{bmatrix} \begin{bmatrix} u_1 \\ u_2 \\ u_3 \\ u_4 \\ u_5 \\ u_6 \end{bmatrix}. \tag{2.46}$$

The elastic constants are related to the propagating phonon wave velocity V. and the medium density ρ, through the Christoffel's equation [2.17].

$$(c_{iklm} I_l I_m - \rho V^2 \delta_{il}) \cdot u_m = 0, \tag{2.47}$$

where, I_l and I_m are the direction cosines of the phonon, u_m is the local displacement vector, and δ_{il} is the Kronecher delta.

Phonon velocity can be obtained by measuring the frequency shift of the respective Brillouin component. Therefore, inelastic Brillouin scattering is a non-destructive powerful tool to understand the elastic behavior of a material.

2. 3. 2 Theory of Brillouin scattering

The main principle of Brillouin scattering is the scattering of photons on sound waves and the constructive interference of the multiply reflected light beam. A plane elastic wave creates a periodic change of density and hence of the local dielectric constant in a medium. The typical velocity of an acoustic wave is between 10^3 and 10^4 m/s. It is slower speed than light in vacuum. Because of this great discrepancy the dielectric inhomogeneity can be regarded as a quasi-static lattice on which the photons of the probing light are scattered. Thus, it is justified

to treat the medium as a periodic multilayer stack with periodicity Λ, the wavelength of the phonon, as shown in Fig. 2. 6. The probing laser light is multiply reflected on these layers and the reflected light interferes on the detector, whose distant to the sample $\boldsymbol{R}$ is much larger than the periodicity of the scattering planes $(\boldsymbol{R} \gg \Lambda)$. The reflected intensity reaches its maximum when the interference is constructive, i.e.,

$$2\text{n}\Lambda \sin\frac{\theta}{2} = \lambda \tag{2.48}$$

With refractive index n and wavelength of light λ.
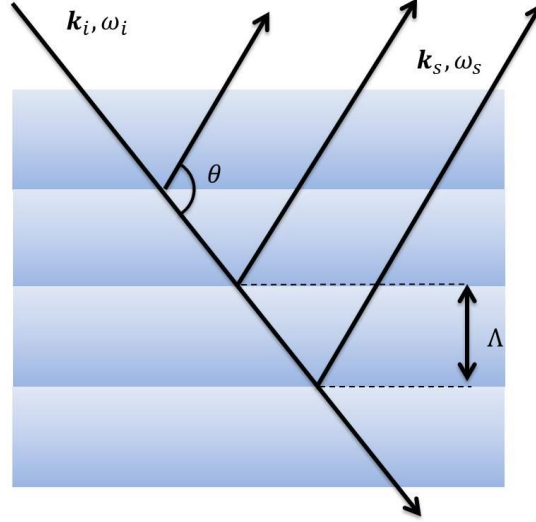
Fig. 2. 6. Brillouin scattering process

Insertion of Eq. 2.48 in the Bragg condition (Eq. 2.8) leads to

$$\frac{2\pi}{\Lambda} = \frac{4\pi n}{\lambda} \sin\frac{\theta}{2} \tag{2.49}$$

and

$$q = \frac{2\pi}{\Lambda}. \tag{2.50}$$

The scattering wave vector $\boldsymbol{q}$ is equivalent to the wave vector $\boldsymbol{k}$ of the sound wave (k=$2\pi/\Lambda$), by changing θ, $\boldsymbol{q}$ can be chosen and at every $\boldsymbol{q}$ the corresponding sound waves are probed selectively. The identity $\boldsymbol{q}= \boldsymbol{k}$ shows that the momentum conservation during the scattering process is realized by a momentum transfer between the sound wave and the photon. From this point of view it is clear that the scattered light changes its angular frequency from ω_i to ω_s by inelastic interaction, in which an acoustic phonon can be either created (Stokes process) or annihilated (anti-Stokes process) depending on the direction of motion of the acoustic wave. In terms of energy conservation considerations it is clear that the exchanged energy $\hbar\omega$

comes from the angular frequency of the phonon which is related to the phonon wavelength and the velocity c of the acoustic wave by

$$\omega_{acoutic\ phonon} = \omega = \frac{2\pi c}{\Lambda}. \tag{2.51}$$

Therefore, the frequency $f = \frac{\omega}{2\pi}$ shows a Doppler shift;

$$f_s = f_i \pm \frac{cq}{2\pi} = f_i \pm \frac{c}{2\pi} \frac{4\pi n}{\lambda} \sin\frac{\theta}{2}, \tag{2.52}$$

using the definition of q given in Eq. 2.8. Here, the minus corresponds to a motion of the acoustic wave away from the detector leading to a frequency decrease, and the plus corresponds to a propagation direction of the acoustic waves towards the detector leading to an increasing photon frequency.

2. 4 The Dynamic properties and Response function of light scattering

For discussion of the dynamics of the ferroelectric phase transitions, we consider the response of damped harmonic oscillators and single Debye-type relaxations [2. 1].

When one dipole polarization at a ith site, α_i is deduced by an external field f with a frequency ω, α_i is expressed by f though the polarizabiltity per unit volume of the system χ_s

$$\alpha_i = \chi_s(\omega)f. \tag{2.53}$$

$\chi_s(\omega)$ of the damped harmonic oscillator model, $\chi_s^l(\omega)$ can be written in the following form;

$$\chi_s^l(\omega) = \chi_s^l(0) \frac{\omega_s^2}{\omega_s^2 - \omega^2 - i\Gamma_0\omega}, \tag{2.54}$$

where ω_s is the resonance frequency in the absence of damping and Γ_0 is a damping constant.

The broad absorption peaks (Fig. 2. 7) in the orientational polarization range manifest that no discrete energy levels exist for the rotational motions of the molecules due to manifold interactions. Due to this reason the orientational polarization is characterized by a relaxation process. Introducing the concept of relaxation, the complex dielectric constant can be written as;

$$\varepsilon^*(\omega) = \varepsilon_\infty + \frac{\varepsilon - \varepsilon_\infty}{1 + i\omega\tau}, \tag{2.55}$$

with real and imaginary parts as;

$$\varepsilon'(\omega) = \varepsilon_\infty + \frac{\varepsilon - \varepsilon_\infty}{1 + \omega^2 \tau^2}, \tag{2.56}$$

$$\varepsilon''(\omega) = \varepsilon_\infty + \frac{(\varepsilon - \varepsilon_\infty)\omega\tau}{1 + \omega^2 \tau^2}, \tag{2.57}$$

To account for the broader peaks in $\varepsilon''^{(\omega)}$ more realistically, it is assumed that different parts of the orientational polarization decline with distribution of relaxation times with the distribution function $g(\tau)$;

$$\varepsilon^*(\omega) = \varepsilon_\infty + (\varepsilon - \varepsilon_\infty) \int_0^\infty \frac{g(\tau)d\tau}{1 + i\omega\tau}, \tag{2.58}$$

with;

$$\int_0^\infty g(\tau)d\tau = 1, \tag{2.59}$$
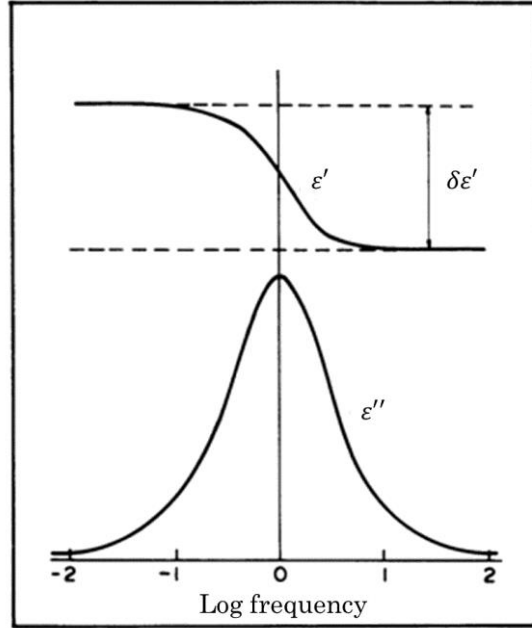
Fig. 2. 7. Comparison of ε' and ε'' as function of log frequency for a single relaxation process.

When $\chi_s(\omega)$ is Debye relaxation model, $\chi_s^r(\omega)$ cab be written in the following from;

$$\chi_s^r(\omega) = \chi_s^r(0) \frac{\gamma_s}{\gamma_s - i\omega}, \tag{2.55}$$

where γ_s is a damping constant. From here, "l" and "r" denote damped harmonic oscillators and Debye-type relaxations, respectively.

28

If we take account of the interaction v_{ij} in the mean-field approximation, the effective field f_i on the ith site is

$$f_i = f + \sum_j v_{ij}\alpha_j \tag{2.56}$$

where we neglect the frequency dependence of v_{ij}. In the mean-field approximation, f_i is treated using linear response theory;

$$\alpha_i = \chi_s(\omega)[f + \sum_j v_{ij}\alpha_j]. \tag{2.57}$$

The dynamic susceptibility $\chi(\omega)$ is obtained as;

$$\chi(\omega) = \frac{N\alpha}{f} = \frac{N\chi_s(\omega)}{1-v\chi_s(\omega)}. \tag{2.58}$$

If frequency go to 0, we know

$$\chi(0)\frac{N\chi_s(0)}{1-v\chi_s(0)}. \tag{2.59}$$

The ferroelectric phase transition occurs when the denominator in Eq. 2.59 becomes zero;

$$1\text{-}v\chi_s(0) = 0, \quad T = T_C. \tag{2.60}$$

In case of the Deby-type relaxation, $\chi_s^r(0)$ can be written as $\mu^2/k_B T$, and Eq. 2.60 gives $T_C = v\mu^2/k_B T$.

If we assume that the ferroelectric phase transition is induced by the damped harmonic oscillator system, Eqs. 2.54 and 2.59 give

$$\chi^l(\omega) = \frac{N\chi_s^l(0)\omega_s^2}{\omega_l^2-\omega^2-i\Gamma_0\omega}, \tag{2.61}$$

$$\frac{\omega_l^2}{\omega_s^2} = \frac{N\chi^l(0)}{\chi^l(0)}, \quad \omega_l^2 = \omega_s^2\frac{T-T_C}{T_C}, \tag{2.62}$$

Eq. 2.62 is identical to the Lyddane-Sachs-Teller relationship, the system becomes untable as $\chi^l(0)$ iverges.

In case of Deby-type relaxation,

$$\chi^l(\omega) = \frac{N\chi_s^r(0)\gamma_0}{\gamma-i\omega}, \tag{2.63}$$

$$\frac{\gamma}{\gamma_s} = \frac{N\chi_s^r(0)}{\chi^r(0)}, \quad \gamma = \gamma_s\frac{T-T_C}{T_C}. \tag{2.64}$$

Eq. 2.64 indicates the "critical slowing down" in the Ising model with mean-field theory.

At high temperature, inelastic light scattering spectrum $I(\omega)$ is expressed as

$$I(\omega) = K\frac{k_B T}{\pi\omega}\text{Im}\chi(\omega). \tag{2.65}$$

In both cases the total integrated intensity of the peak can be obtained by making use of the Kramers-Kronig relations as

$$I = \int_{-\infty}^{\infty} I(\omega) d\omega \propto \mathrm{Re}\chi(0). \qquad (2.66)$$

In the field of spectroscopy, it is general that the type of the ferroelectric phase transition is determined by the behavior of the polarization spectral response around T_c. If the corresponding phonon mode frequency decreases to zero at T_c, it is a signature of the displacive type phase transition. In the order-disorder type one, the relevant phonon frequency stays temperature independent, while another strongly temperature dependent excitation of the relaxation occurs.

References

[2.1] W. Hayes and R. Loudon, *Scattering of Light by Crystals*, (Dover, New York, 1978).

[2.2] R. Blinc and B. Zeks, *Soft Modes in Ferroelectrics and Antiferroelectrics*, (North-Holland, Amsterdam, 1983).

[2.3] H. Z. Cummins and A. P. Levanyuk, *Light scattering near phase transitions*, (North-Holland, Amsterdam 1983).

[2.4] H. Z. Cummins and P. E. Schoen, *Laser Handbook Volume 2*, (North-Holland, Amsterdam 1972).

[2.5] M. E. Line and A. M. Glass, *Principles and Applications of Ferroelectrics and Related Materals*, Clarendon, Oxford 1977).

[2.6] A. Einstein, Ann. Phys., **338** (1910) 1275.

[2.7] H. Z. Cummins and R. W. Gammon, J. Chem. Phys., **44** (1966) 2785.

[2.8] B. J. Berne and R. Pecora, *Dynamic light scattering*, (Dover, Mineola 2000).

[2.9] J. F. Nye, *Physical Properties of Crystals*, (Clarendon, Oxford 1957).

[2.10] J. R. Ferraro and K. Nakamoto, *Introductory Raman spectroscopy*, (Academic, Boston 1994).

[2.11] R. Loudon, Adv. Phys, **13** (1964) 423.

[2.12] T. C. Damen, S. P. S. Porto and B. Tell, Phys. Rev., **142** (1966) 570.

[2.13] J. Toulouse, F. Jiang, O. Svitelskiy, W. Chen and Z. –G. Ye, Phys, Rev. B, **72** (2005) 184106.

[2.14] C. Boulesteix, F. Varnier. A. Llebaria, and E. Husson, J. Solid State Chem., **108** (1994) 141.

[2.15] S. A. Prosandeev, E. Cockayne, B. P. Burton, S. Kamba, J. Petzelt, Y. Yuzyuk, R. S. Katiyar, and S. B. Vakhrushev, Phys. Rev. B, **70** (2004) 134110.

[2.16] H. Taniguchi, M. Itoh and D. Fu, J. Raman Spctrosc., **42** (2011) 706.

[2.17] E. Dieulesaint and D. Royer, *Elastic Waves in Solids* (Wiley, New York 1980).

Chapter 3. Experimental Methods

3. 1 Dielectric spectroscopy

Dielectric spectroscopy measures the dielectric properties of a polar compound as a function of frequency. It is based on the interaction of an external field with the dipole moment of a sample. For a linear, isotropic dielectric the time-dependent polarization P(t) and dielectric displacement D(t) are related to the time-dependent electric filed E(t) through the susceptibility χ as:

$$P(t) = \chi E(t), \tag{3. 1}$$

$$D(t) = (4\pi\chi + 1)E(t), \tag{3. 2}$$

The electric susceptibility χ, which is second-rank tensor, is a dimensionless proportionality constant that indicates the degree of polarization on a dielectric material in response to an applied electric field and is also related to the polarizability by the Clausius-Mossotti relation. The dielectric constant is related the electric susceptibility as:

$$4\pi\chi + 1 = \varepsilon \tag{3. 3}$$

When the frequency ω of the electric field is changed, the definition of complex dielectric constant therefore becomes:

$$D_0 e^{-i\omega t} = \varepsilon^* E_0 e^{-i\omega t}, \tag{3. 4}$$

where D_0 and E_0 are the amplitudes of the displacement and electric fields, respectively. When the frequency is too low, the phase difference δ becomes zero reaching to quasi-static case. The complex dielectric constant can be split into two parts.

$$\varepsilon^* = \frac{D_0}{E_0}(\cos\delta + i\sin\delta) = \varepsilon'(\omega) + i\varepsilon''(\omega) \tag{3. 5}$$

where ε' is the real component, which is in phase with the applied field; ε'' is the imaginary component, which is in quadrature with the applied field. Both components of the complex dielectric permittivity are related each other by the Kramers-Kronig relations.

The frequency dependent behavior of ε' and ε'' for all polar compounds in the condensed phase is described in Fig. 3. 3. The non-equilibrium effects appearing with increase in frequency originate from the electric polarization that is built up of three parts, the orientational, atomic, ad electronic polarization, each part corresponding with motions of a different kind of microscopic particles, molecules and ions, atoms, and electrons, respectively.
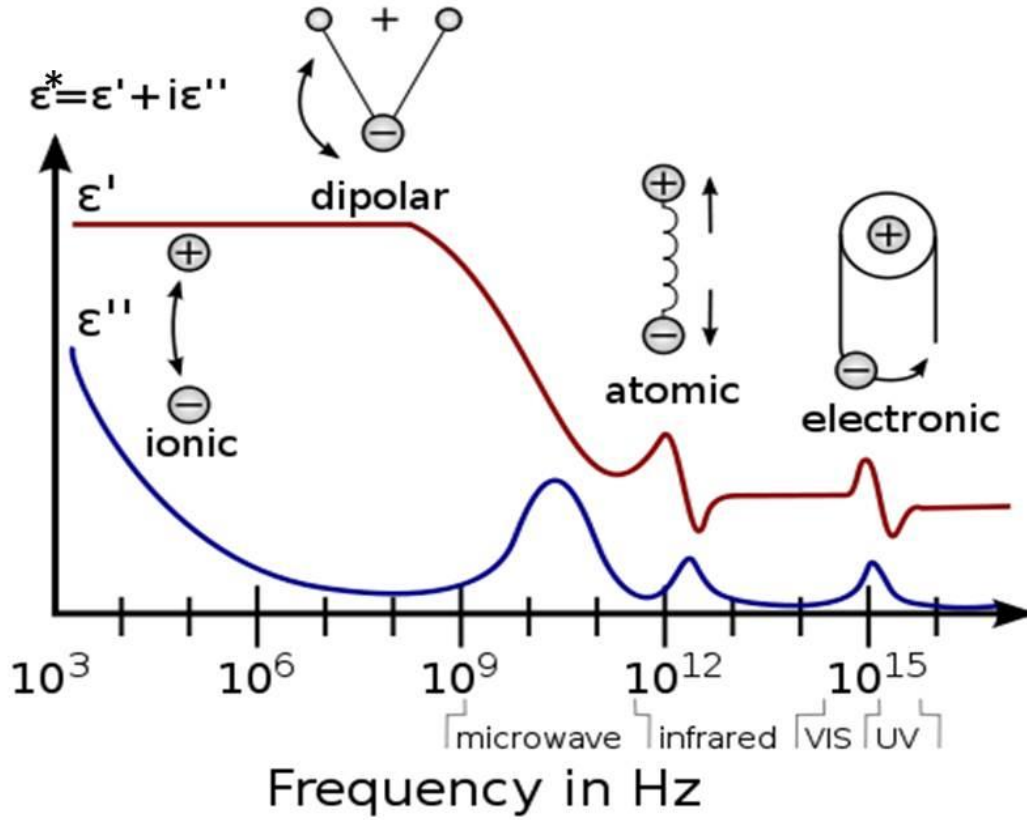
Fig. 3. 1 Dielectric dispersion and loss for a polar compound [3.1]

Dielectric constant of the specimens was measured by using LCR meter (HP4263B, Agilent) and impedance analyzer (SI 1260). A home-made box furnace and Linkam stage (THMS 600, Linkam) were combined to cover the temperature range from 300 ^oC down to -50 ^oC. For auto measurement and fine adjustment process of delay parameter and number of average, the data were collected by using NI LabVIEW™ software to measure temperature & frequency dependence of the capacitance C_p and dielectric loss D. The capacitance of a capacitor with the dielectric is

$$C_p = \frac{\varepsilon\prime\varepsilon_0 A}{d},$$ (3. 6)

$$D = \frac{\varepsilon\prime\prime}{\varepsilon\prime} = \tan\delta,$$ (3. 7)

where, ε_0 (8.85 × 10^{-12}F/m) is the permittivity of free space, A and d corresponds to the area and thickness of the conducting electrode, respectively.

The unpoled samples were first heated to higher temperature and then measurements were done in a cooling run at a rate of 1 ^oC/min. In contrast, the poled samples were measured in a heating run and then measurements were done in a cooling run again for comparison between the poled and unpoled condition.

33

3. 2 Instrumentation of Inelastic Light Scattering

  In light scattering experiments the difference in frequency between the scattered and incident light extends from a few hertz to approximately 10^{14} Hz (~3000 cm^{-1}) and a range of dispersing elements is required to resolve these differences. They have some characteristics in common, although they differ on physical principles. The resoling power ρ is a property of a spectrometer system of major importance. It is determined by the apparatus function W (the representation the system gives of an incident laser beam of monochromatic light). If δv is the width of W then, for a given frequency v, the resolving power is:

$$\rho = \frac{v}{\delta v} \qquad\qquad\qquad\qquad (3.\,8)$$

The dispersion of a Raman (grating) spectrometer with a 1 m focal length is adequate, with slit widths of a few microns, to accommodate diffraction gratings with $\rho \cong 10^5$ in first order [3.2]. However, this magnitude of resolution is not easy to achieve for single grating with excitations of energy less than ~100 cm^{-1}. In case of study of Brillouin scattering in single crystal, resolving powers as high as 10^8 are desirable, and values approaching this can be conveniently achieved with the Fabry-Perot interferometer (FPI).

  The physical principles of the two techniques and particularity of our systems used in this thesis are to be discussed below.

3. 2. 1 Raman scattering experimental

  For the Raman component, spectral dispersion is performed using a double or triple grating monochromator to enhance contrast so that Raman lines near the laser excitation frequency can be observed. The high collimation and narrow bandwidth of laser sources has been used as a Raman excitation source, this provides much higher spectral source intensity, polarization and straightness. Detection of scattered light is usually done by photon counting techniques with a photomultiplier (PM) tube and charge-coupled device (CCD). The detector can achieve sensitivities in the ultraviolet and visible spectral regions.

  In modern spectroscopy usually multiple monochromators are employed for Raman scattering. They can either be operated in an additive or in a subtractive mode as Fig 3. 2. For a subtractive mode the first two monochromators have oppositely directed spatial dispersions. This means that after passing the first two monochromateros the light which satisfies the band-pass condition is refocused on the exit slit which serves as the entrance slit of the third monochromator. Only the latter provides the spatial dispersion. Generally, CCD detector uses the subtractive mode because the detector can record a much large part of the spectrum. For operating of the subtractive mode the output slit is narrow, the linear dispersion and the resolution are low. In order to obtain high resolution, the additive mode is essential with PM tube. In case of the additive mode, the linear dispersion and the resolution are higher than the

subtractive mode but the detector can record a small part of the spectrum, while the output slit is wide.
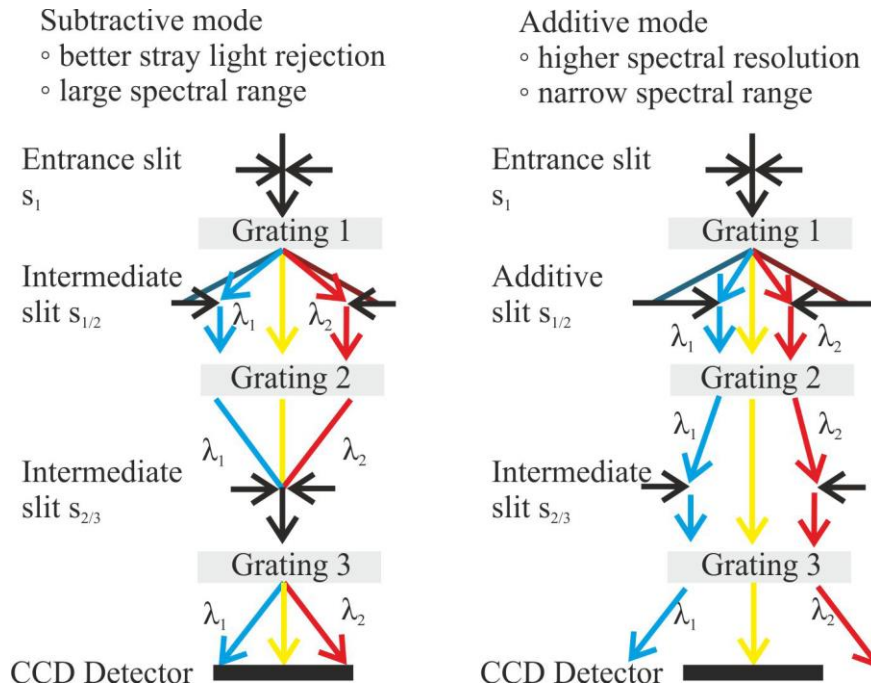

Fig. 3. 2. Schematic sketch of the subtractive and the additive mode for triple monochromators [3.3]

Fig. 3. 3 is sketches of the setup for a double monochromator in the additive and subtractive mode for Czerny-Turner arrangement. For instance, the additive mode needs two grating, three slits, and four concave mirrors. The incoming light is two times additively dispersed by the gratings 1 and 2. Scanning occurs by synchronous rotation of both gratings. The resolution and suppression of stray light is greatly improved compared to a single monochrmator. Although multiple monochromators reduce the intensity of spectrum by passing the grating, we can approach more low frequency range below ~100 cm^{-1} with high resolution.

For further improvement a third monochromator can be arranged behind the exit slit resulting in a triple monochromator system. The third monochromator must be tuned to be synchronous with the two other gratings. Such systems are often used for spectroscopic analyses in the immediate vicinity of a very strong line such as a laser line. For the study of phase transition, it is very powerful tool to study soft optic mode dynamics in ferroelectric, and the low frequency relaxation process such as boson peak in glass system. In this case the third monochromator operates with a wide slit and a sharp cut off towards the laser line.
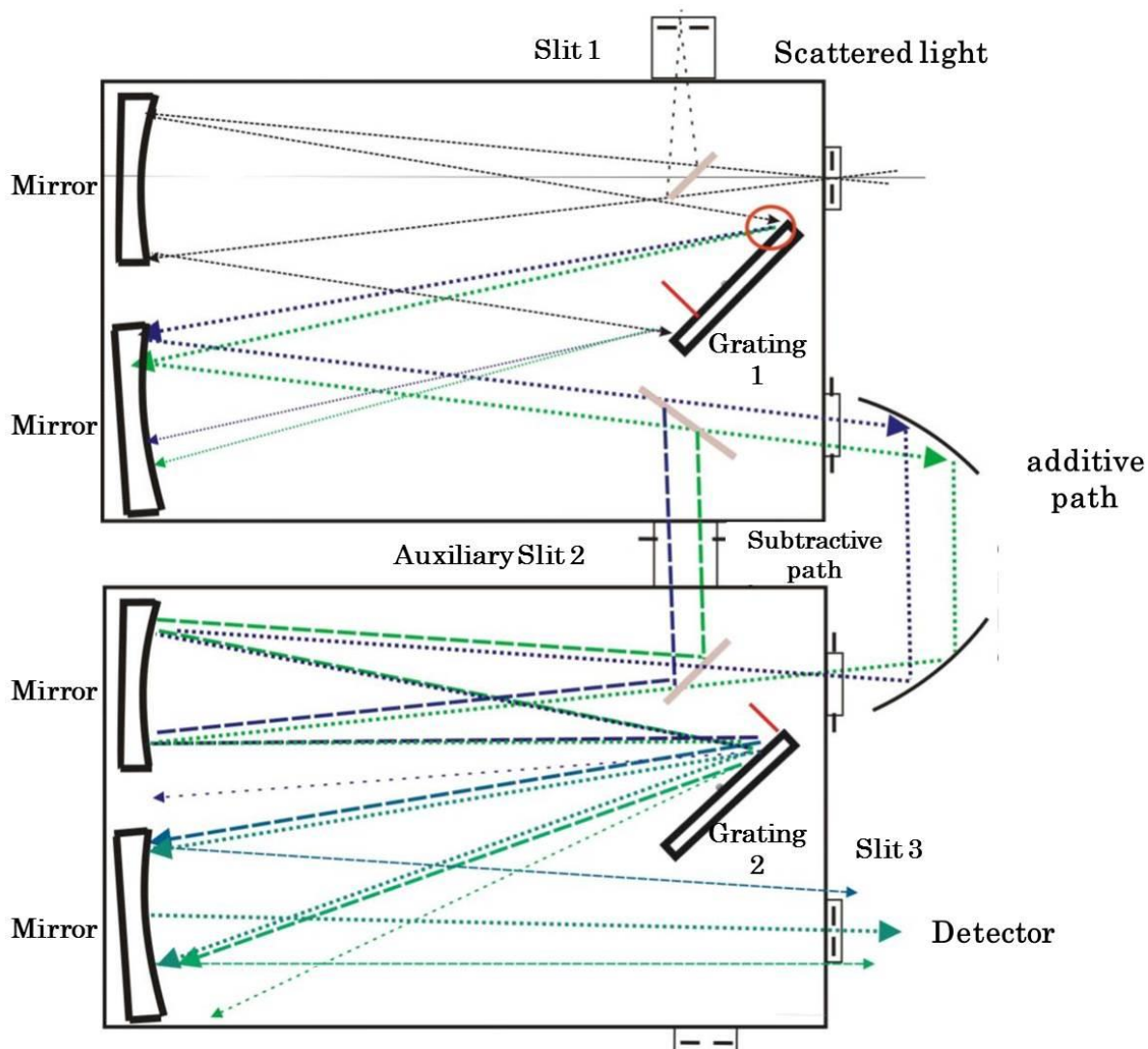
Fig. 3. 3. Schematic representation of a double monochromator in Czerny-Tuner grating system.

Fig. 3. 3 is a block diagram of a micro-Raman spectroscopy setup used in the present study. Raman spectra are excited using a diode-pumped solid-state laser (TORUS, Laser Quantum) with a single frequency operation at 532 nm. The light beam is focused onto a sample by objective lens. Scattered light is then collected by same objective lens using backward geometry, and is focused on the entrance slit of a grating spectrometer, which acts as a tunable filter. The scatted light is analyzed by a triple-grating spectrometer of the additive dispersion (Jobin Ynon T-64000). The spectral resolution was below 2 cm^{-1} (~60 GHz). The temperature variation of the Raman spectra of all samples was carried out. In order to control temperature on microscope, samples were inserted into a cryostat cell (THMS 600, Linkam), whose temperature stability was $\pm 0.1\,^oC$ with ranges of -190 ~ 600 ^oC in temperature dependence Raman measurements.
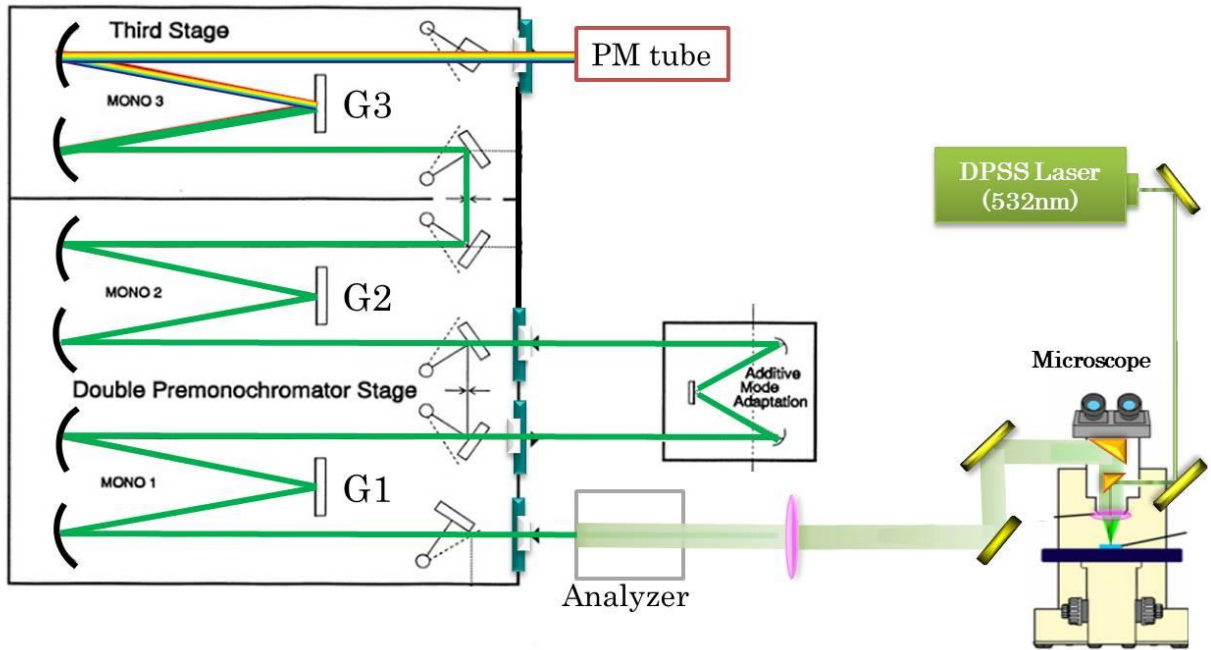
Fig. 3. 4. The block diagram of micro-Raman spectroscopy.

The T64000 system is coupled modified microscope (BH-2, Olympus). The modified microscope is two important features by using small prism mirror and rotation system of $\frac{1}{2}\lambda$ wave-plate. From $\frac{1}{2}\lambda$ wave plate, incident light and scattered light are changed direction of polarization as Fig. 3. 5. By using the rotation system on microscope, angular dependence of Raman scattering is investigated during temperature variation without rotation of samples.
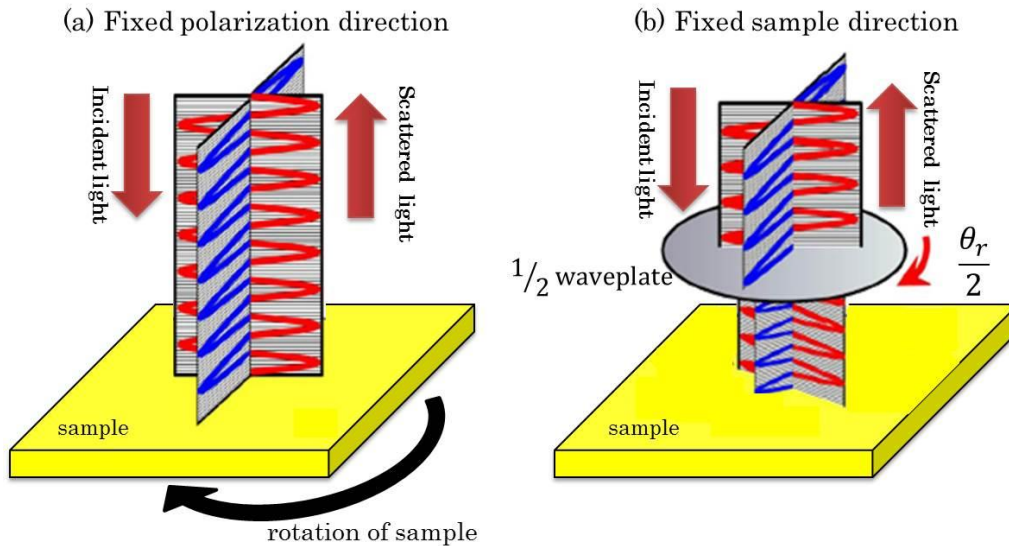
Fig. 3. 5. Comparison between rotation of sample (a) and $\frac{1}{2}\lambda$ wave-plate (b).

3. 2. 2 Brillouin scattering experimental

Fabry-Perot interferometer

The high resolution required to obtain the Brillouin spectrum, coupled the intrinsic signal from the materials with the usually extreme elastic scattering owing to sample surface imperfections and scattering. In order to record the Brillouin spectrum, there are typical cases where grating spectrometers can resolve the Brillouin frequency shifts with the part of huge elastic scattering tail. It was imperfect method to get the weak Brillouin signals to resolve the background of the normally extremely intense elastically scattered light because of their low contrast ratio [3.4]. For the necessary and sufficient condition, FPI is suitable. Since E. Gross who first experimentally demonstrated the existence of the velocity of sound by inelastic light scattering in 1930, Brillouin scattering using a FPI has been a well-established method for the investigation of thermally excited sound waves near GHz range in liquids and solids [3.5].
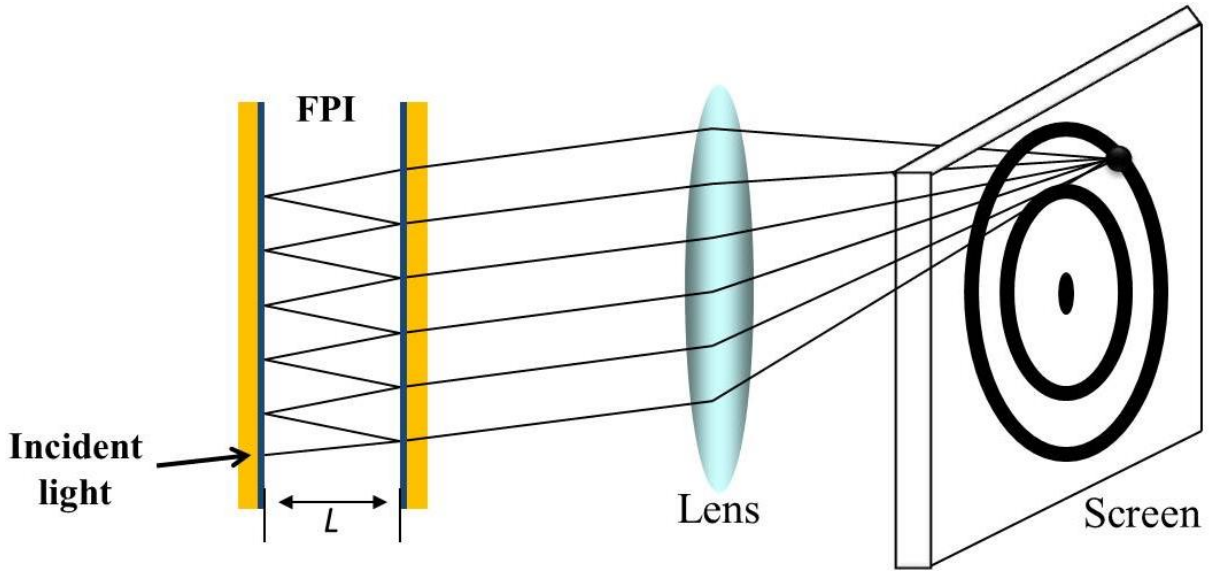
Fig. 3.6 Principle of a Fabry-Perot etalon, which has a fixed mirror spacing L.

Generally, FPI (or Fabry-Perot etalon) consist of two mirror plates and is held accurately parallel at a (fixed) distance L. Using a broad source of monochromatic incident light, we obtain a system of concentric rings in the focal plane of the collecting lens (Fig. 3.6). For a given spacing L the interferometer (etalon) will transmit only certain wavelength λ as determined by

$$T = \frac{\tau_0}{1+\left(\frac{4F^2}{\pi^2}\right)\sin^2\left(\frac{2\pi L}{\lambda}\right)} \qquad (3.\,9)$$

where F, the finesse, is a quality factor depending primarily on the mirror reflectivity, and τ_0 (<1) is the maximum possible transmission determined by losses in the system. These parameter are decided and fixed from quality of mirror coating inside FPI. When only those wavelengths are satisfied as equation (3.2),

$$L = \frac{1}{2}p\lambda \qquad\qquad (3.10)$$

where p is integral values, can be transmitted. After passing focal lens, we obtain the Airy distribution. When we choose one line in center of screen, the form of transmitted wavelengths are expressed in the following Fig. 3.7.
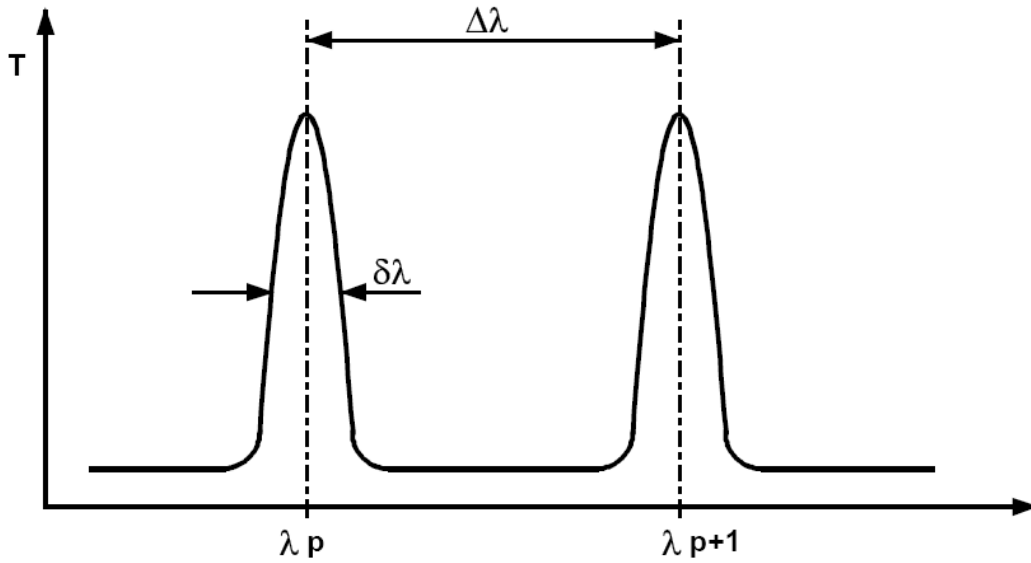
Fig. 3. 7. Two successively transmitted wavelengths from a single FPI.

The finesse F is related to the spacing between successive transmitted wavelengths $\Delta\lambda$ (known as the free spectral range, FSR) and the width $\delta\lambda$ of a given transmission peak by:

$$F = \frac{\Delta\lambda}{\delta\lambda} = \frac{\pi\sqrt{R}}{(1-R)} \qquad\qquad (3.11)$$

where R is the reflectance (it is related the instrument function and the fineness of the fringes). For R=0.7 we find F=8.3, whereas if R is increased to 0.95, F becomes 61.2. For expression of the resolving power:

$$\rho = nF_e \qquad\qquad (3.12)$$

where F_e is the effective finesse. The order of interference n is a maximum at the center of the ring system and for L=0.1 m and λ=500 nm has the value 4×10^5; operating with an effective finesse F_e=25 we have ρ=10^7 in single FPI.

The FPI is used as a spectrometer by varying the spacing L so as to scan the light intensity at different wavelengths. However it is immediately apparent that the measured intensity at a given spacing is the sum of the intensities at all wavelengths satisfying condition Eq.(3.10). An unambigious interpretation of the spectrum is thus impossible unless it is known a priori that the spectrum of the light lies entirely within a wavelength spread$< \Delta\lambda..$

It is true that since:

$$\Delta\lambda = \frac{\lambda^2}{2L} \qquad\qquad (3.\ 13)$$

and similarly:

$$\Delta\nu_{(frequency)} = \frac{c}{2L} \qquad\qquad (3.\ 14)$$

where c is the speed of light. $\Delta\lambda$ can be increased arbitrarily large by decreasing L. However, $\delta\lambda$ increases proportional to $\Delta\lambda$ and thus the resolution decreases. In fact Eq.(3. 11) shows that the ratio between FSR, $\Delta\lambda$ and the resolution $\delta\lambda$, is just the finesse F. In practice F cannot be made much greater than about 100 due to limitations on the quality of mirror substrates and coatings. The relationship between FSR and resolution is thus fixed within limits determined by the achievable values of F.

In order to control the finesse F, we must choose pinhole size because the width $\delta\lambda$ of a transmission peak is related the resolution and mirror spacing L as shown in Fig. 3. 8.
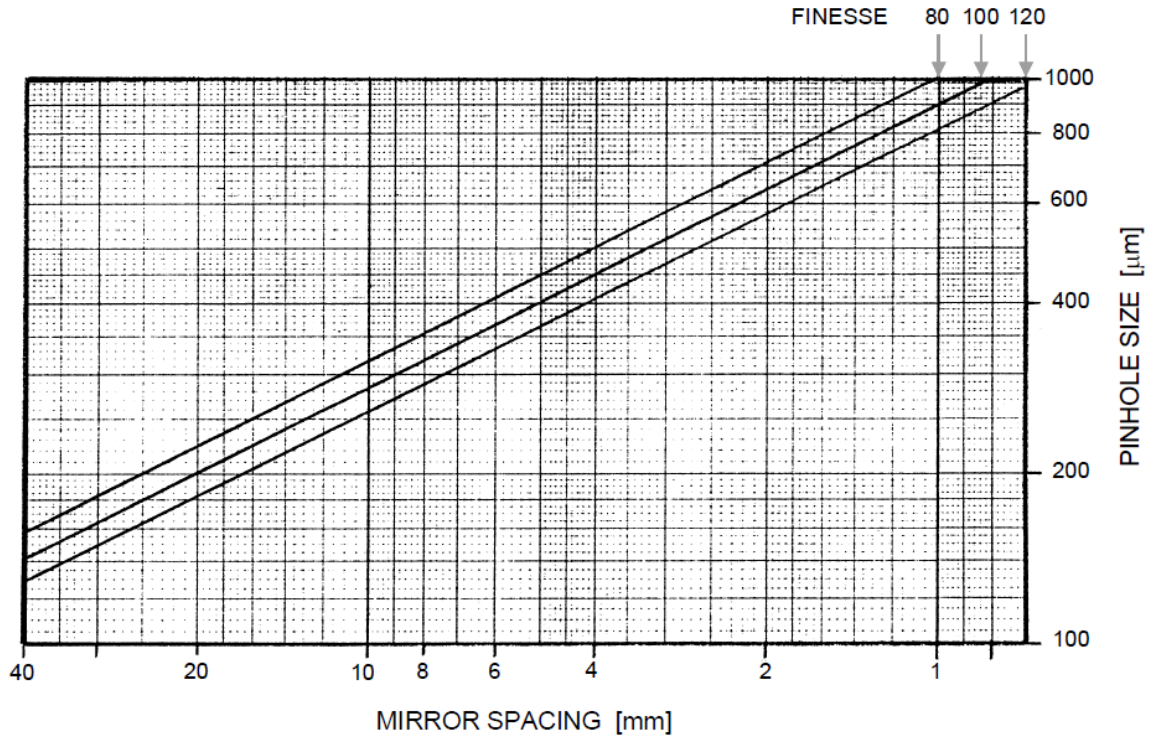

Fig. 3. 8. The relation between mirror spacing L and pinhole size [3.7]

Nevertheless, single-pass FPI was insufficient for condensed matter system such as single crystals. From last half century, multipass interferometer was developed with high resolution [5, 6]. If high resolution is required combined with high contrast, for example to analyze the linewidth of a narrow Brillouin component, a tandem arrangement of a multipass interferometer and a spherical one may be successfully employed.

Tandem Fabry-Perot Interferometer

If two interferometers with mirror distances L_1 and L_2 are placed in cascade to transmit two different interference orders $p_1 = 2L_1/\lambda$ and $p_2 = 2L_2/\lambda$ of the incident wavelength λ, the transmitted intensity is composed of the product of the Airy function of both interferometers. The total transmission curve is composed of a central elastic peak corresponding to exact coincidence of one of the orders of each FPI, and small ghosts representing weakly transmitted interference orders of the two interferometers. Fig. 3. 9 is a schematic of the transmission curves of the etalon (a) FPI2, (b) FPI1 and (c) of both interferometers in series (tandem operation) as a function of the mirror separation of the first etalon, L_1.
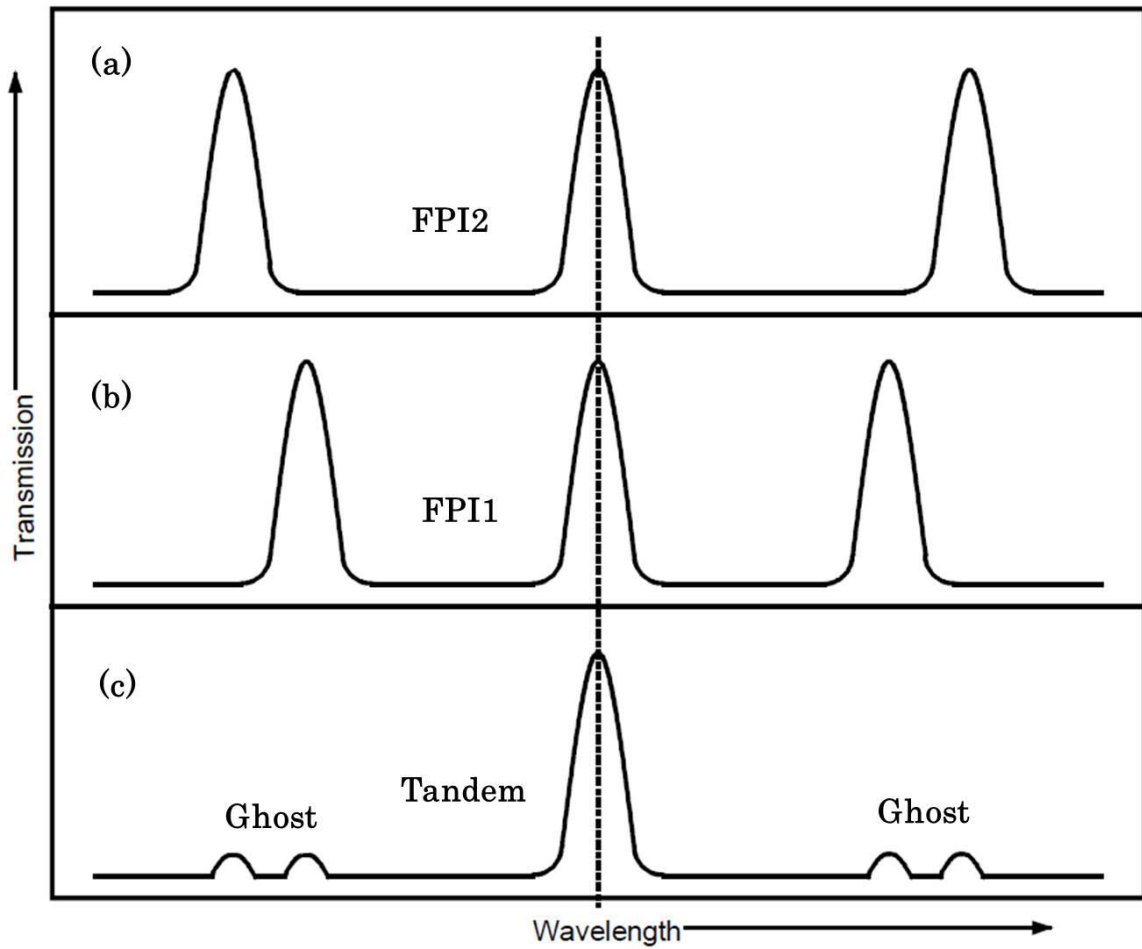

Fig. 3. 9. Transmission properties for (a) FPI1, (b) FPI2, and (c) FPIs in series.

Assuming that for a given value of L_1 both interferometers are in transmission, a change of $\lambda/2$ in L_1 puts FPI1 into the next transmission order. Due to the common mounting of the movable mirrors the change in the spacing of the second interferometer is smaller by a factor of $\cos\theta$ with θ the angle between the optical axes of the two interferometers as displayed in the figure. Thus FPI2 is now not in transmission, and the transmission maxima of both etalons lie at different values of L_1. The same argument applies for inelastic excitations, which are transmitted only if they belong to the common transmission order. The inelastic signal represents closely the scattering cross section of the sample.
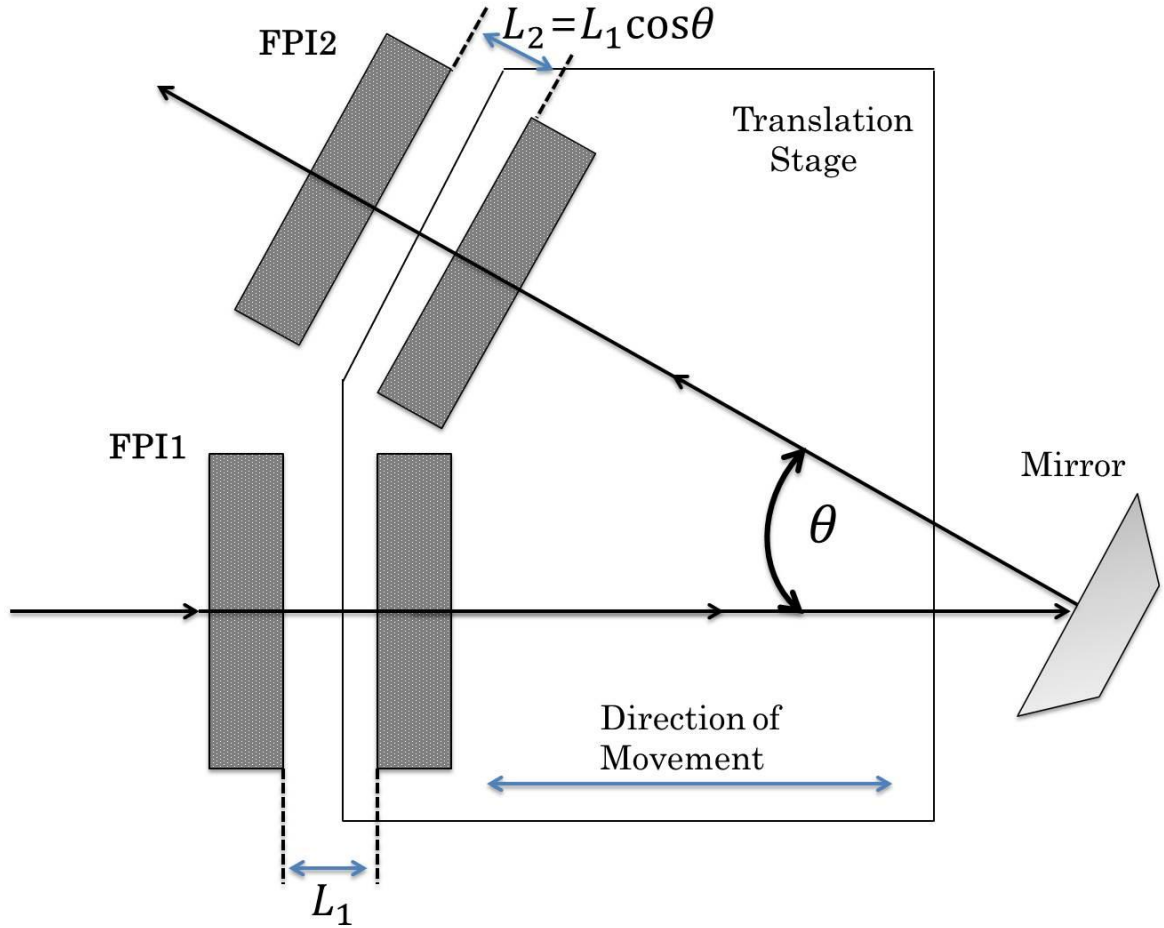
Fig. 3. 10. Schematic view of the operation of a Sandercock-type tadem Fabry-Perot interferometer.

For an experimental realization of the transmission, a flatness of the mirror surfaces of better than $\lambda//200$ and a parallelism of $\lambda//100$ of the two mirrors of each interferometer are necessary. To maintain the latter, a sophisticated active stabilization of the mirror alignment is needed, as discussed above. In order to obtain the high contrast necessary to detect the weak inelastic signals the light is sent several times through both interferometers using a system of retro-reflectors and mirrors.

The overall free spectral range can be increased 10 - 20 times over the FSR of a single interferometer. Usually distances L_1 and L_2 are chosen such that $L_2/L_1 = k / n$, where k and n are incommensurate prime numbers. The effective FSR becomes k times the free spectral range of the first interferometer. The major difficulty of tandem interferometry is represented by the synchronization of the two interferometer scans. The changes δL_1 and δL_2 must satisfy

$$\delta L_1 / \delta L_2 = L_1/L_2 \tag{3.15}$$

In order to realize physically the synchronously scanned tandem interferometers, the two scanning mirrors are mounted on the same scanning stage at an angle θ. (See Fig. 3.10).

In this way, $L_2 = L_1 \cos\theta$ and thus the ratio $\delta L_1 / L_1 = \delta L_2 / L_2$ is satisfied. In the tandem interferometer used for the measurements, $L_2/L_1 = 19/20$, corresponding to $\theta \approx 18^o$.
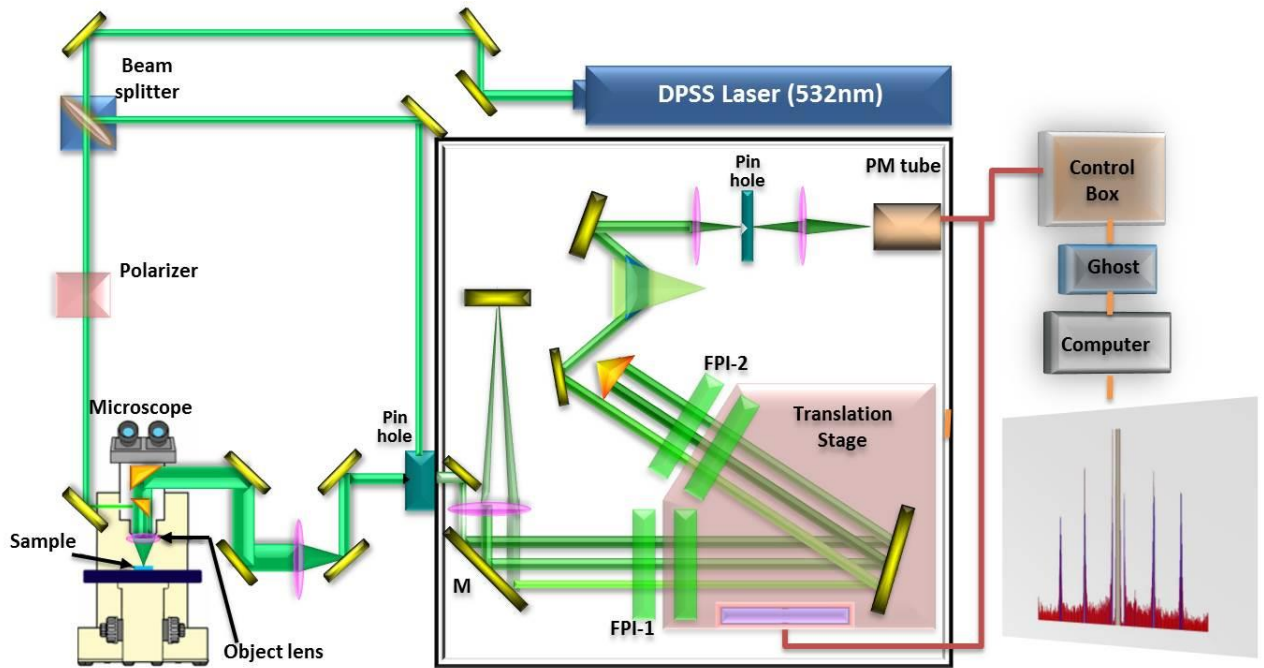

Fig. 3. 11. The block diagram of micro-Brillouin spectroscopy.

Optics for a six-pass tandem interferometer

The application of linear piezoelectric scanning stage and PM tube has been achieved the significant development of six-pass FPI. A most useful FPI is established by Sandercock *et al* [3.8]. and has been the technique of standard Brillouin scattering study for high resolution and contrast. The schematic of Sandercock type tandem FPI is shown in Fig. 3. 11. It passes 3+3 times through two different FPIs to increase its resolution and the contrast of a spectrum. In the present study, a diode-pumped solid-state laser with a single frequency operation at 532 nm with 100 mW (Compass, Coherent) was used as an excitation source. A microscope (BX-60,

Olympus) combined with a temperature controller (THMS 600, Linkam) was used to monitor the sample surface and to control the temperature such as micro-Raman scattering system. In case of the microscope for Brillouin scattering, modified microscope consists of polarizer and analyzer in order to confirm domain structure.
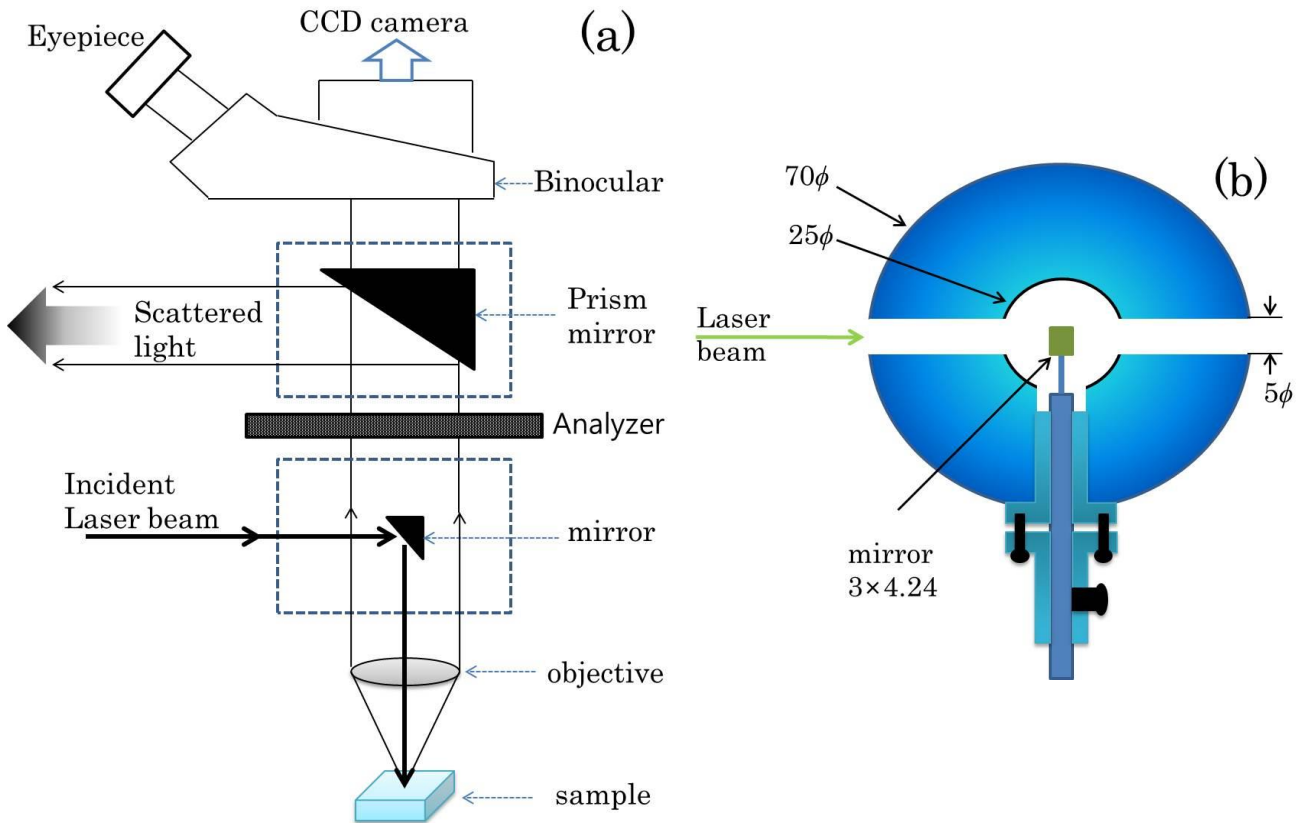
Fig. 3.12. Scheme of a modified microscope: (a) optical path in the microscope; (b) connecting part of the microscope [3.9].

Modified microscope of light scattering

A laser beam is inserted into optical microscope, and it is reflected downward and focused by an objective lens onto the sample. The scatted beam is collected by the same objective lens. It is easy to adjust a focal point because focal point is monitored by using eyepiece of microscope.

In addition, a 90° prism for the outlet of the scatted light and a half-mirror for the illuminator was placed side by side in was placed side by side in the original cube of the microscope. As shown in Fig. 3. 12, the prism was used to direct the scattered light outside the microscope. It is put on a rubber 0 ring which allows a minor adjustment of its orientation. Selection between the light scattering experiment and the sample illumination can be made by

sliding the cube. Use of the high optical quality objective lenses and the backward scattering geometry are shown in Fig. 3. 12 provides this experiment with the following features: (a) Because the objective lens focuses the laser beam, the size of the focal region, whose diameter and length are denoted as d_0 and l_0, respectively, in Fig. 3. 13, is much smaller than that obtained with the conventional optical lens. (b) Changing lenses is easily done by the mechanical revolver. (c) Since the objective lens not only focuses the laser beam but also collects the scattered light, alignment is easy and exact.

Table 3.I summarizes the characteristics of the objective lenses used in this thesis. The values in the table were obtained under the following conditions: the wavelength of a laser $\lambda=$ 532 nm and the diameter of a laser beam $D_L=$ 0.35 mm. The dimension of the focal (or scattering) region was caused by diffraction [3.10]. The spot diameter d_0 and the length l_0, of the focal region are approximately given by:

$$d_0 = \left(\frac{4}{\pi}\right)\lambda f/D_L, \tag{3.16}$$

$$l_0 = \left(\frac{\pi}{\pi 6}\right) d_0^2/\lambda, \tag{3.17}$$

respectively, where f mean focal length. According to above calculation, the spot size is less than 50 μm. Micro Raman and Brillouin scattering are very powerful tools to investigate the relaxor crystals which are characterized by microheterogeneity [3.11].

Table. 3. I. Characteristics of the objective lenses.

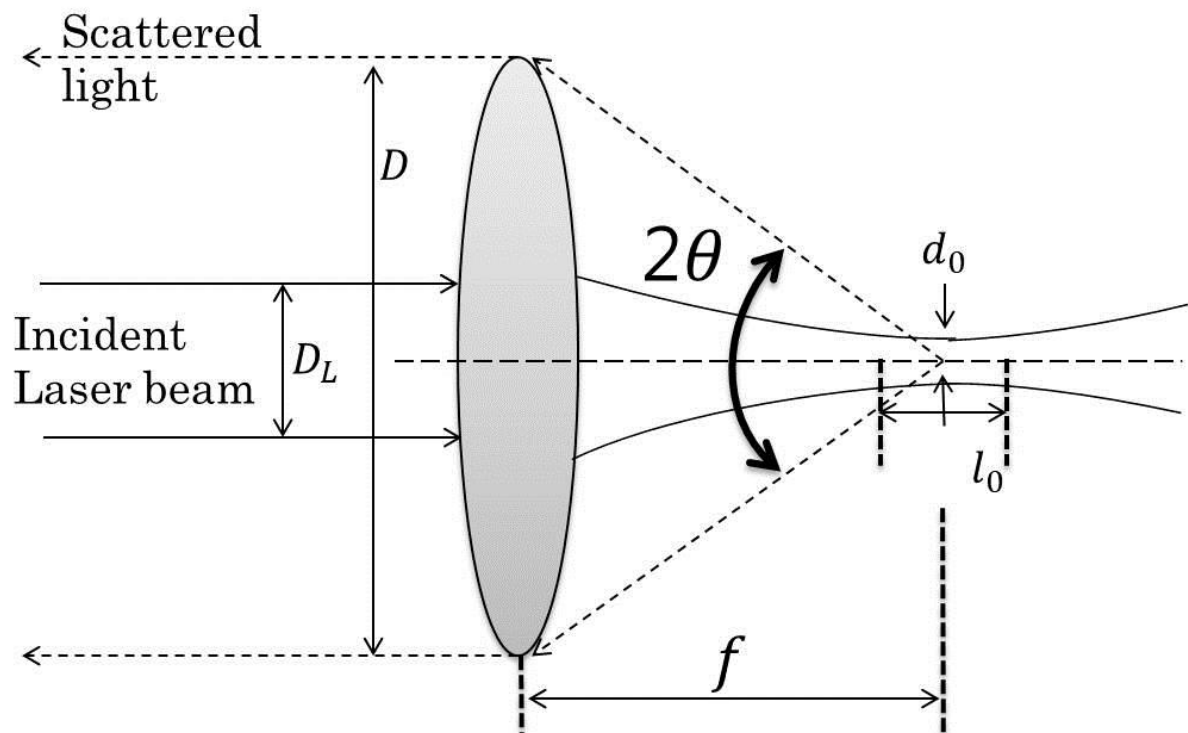| Manifying power	Focal length (mm)	working distance(mm)	spot diameter (μm)	length of focal region (mm)
50×	3.6	10.6	6.967	0.048
20×	9	12	17.42	0.299
10×	18	10.6	34.84	1.194
5×	36	19.6	69.67	4.777

Fig. 3. 13. Sample illumination and scattered light collection through the microscope [3.9]

References

[3.1] M. A. Silaghi, *Dielectric Material*, (INTECH, 2012)

[3.2] W. Hayes and R. Loudon, *Scattering of Light by Crystals*, (Dover, New York, 1978)

[3.3] Horiba Jonin-Yvon: *LabSpec operating manual* (part number : 31 087 064)

[3.4] E. Gross, Nature **126** (1930) 201.

[3.5] J. R. Sandercock: Phys. Rev. Lett. **28** (1972) 237.

[3.6] C. Roychoudhuri and M. Hercher, Appled Optics **16** (1977) 2514

[3.7] JRS Scientific Instruments: *Tandem Fabry-Perot Interferometer-operating manual*

[3.8] R. Blinc and B. Zeks, *Soft Modes in Ferroelectrics and Antiferroelectrics*, (North-Holland, AAmsterdam, 1983).

[3.9] Y. Takagi and K. Kurihara, Rev. Sci. Instrum. **63** (1992) 5552.

[3.10] B. Chu, *Laser Light Scattering* (Academic, New York, 1974)

[3.11] F. M. Jiang and S. Kojima, Appl. Phys. Lett. **77** (2000) 1271.

Chapter 4. Phase transition behaviors in relaxor ferroelectric [001]-poled Pb(In$_{1/2}$Nb$_{1/2}$)O$_3$–Pb(Mg$_{1/3}$Nb$_{2/3}$)O$_3$–PbTiO$_3$ single crystals studied by Brillouin light scattering

4. 1 Introduction

Lead-based complex perovskite single crystals such as $Pb[(Zn_{1/3}Nb_{2/3})_{1-x}Ti_x]O_3$ (PZN-xPT) and $Pb[(Mg_{1/3}Nb_{2/3})_{1-x}Ti_x]O_3$ (PMN-xPT) have been studied intensively due to their excellent piezoelectric performances since the pioneering work by Park *et al.* [4.1]. The piezoelectric coefficient d_{33} and the electromechanical coupling constant k_{33} of these systems were shown to be more than 2000 pC/N and 90% respectively when the composition x was located near the morphotropic phase boundary (MPB). However, PZN-xPT and PMN-xPT suffer from several drawbacks, *i.e.,* low Curie temperature (T_C), low R-T (rhombohedral to tetragonal) transition temperature (T_{RT}), and low coercive field, all of these limiting the temperature and electric field usage ranges for practical applications. Extensive efforts have been focused on the improvement of thermal stability of these lead-based perovskite relaxor ferroelectrics by looking for new binary or ternary systems [4.2-3].

Recently, Pb(In$_{1/2}$Nb$_{1/2}$)O$_3$–Pb(Mg$_{1/3}$Nb$_{2/3}$)O$_3$–PbTiO$_3$ (PIN-PMN-PT) ternary system was found to show higher phase transition temperatures along with comparable piezoelectric performances to PMN-xPT [4.4-8], which is expected to broaden the temperature and electric field ranges for applications as piezoelectric devices. Recently, various properties of PIN-PMN-PT single crystals near MPB including elastic, dielectric, and piezoelectric properties have been studied under different poling conditions [4.9-21]. However, the ferroelectric phase transition behaviors of PIN-PMN-PT single crystals have not been studied in detail. A great portion of the published data on this system are reported on poled samples at room temperatures, and studies on the phase transition behaviors in the temperature window of as-grown or unpoled samples in comparison with poled ones are scarce. The dielectric constant in the vicinity of the Curie temperature of PZN-xPT and PMN-xPT near MPB usually exhibits very sharp, discontinuous changes, while that of PIN-PMN-PT is broad and diffusive [4.8]. These distinctive results suggest that the phase transition behaviors might be different between binary and ternary systems. Understanding of the phase transition behaviors under various conditions including dc bias field effect is prerequisite to improving material performances and practical applications of PIN-PMN-PT, which is the motivation of this study. In this chapter, we report the temperature dependence of acoustic anomalies, quasi-elastic central peaks and dielectric properties of [001]-oriented PIN-PMN-PT single crystals under unpoled and poled conditions. The observed acoustic anomalies and excitation of central peaks will be discussed in detail in relation with the phase transition behaviors and dynamics of

polar nano regions (PNRs), which is one of the key concepts in the physics of relaxor ferroelectrics.

4. 2 Experimental

The single crystal used in the current study was supplied by TRS Technologies Inc. It was grown by the modified Bridgeman method and has the nominal composition of 0.26PIN-0.46PMN-0.28PT.
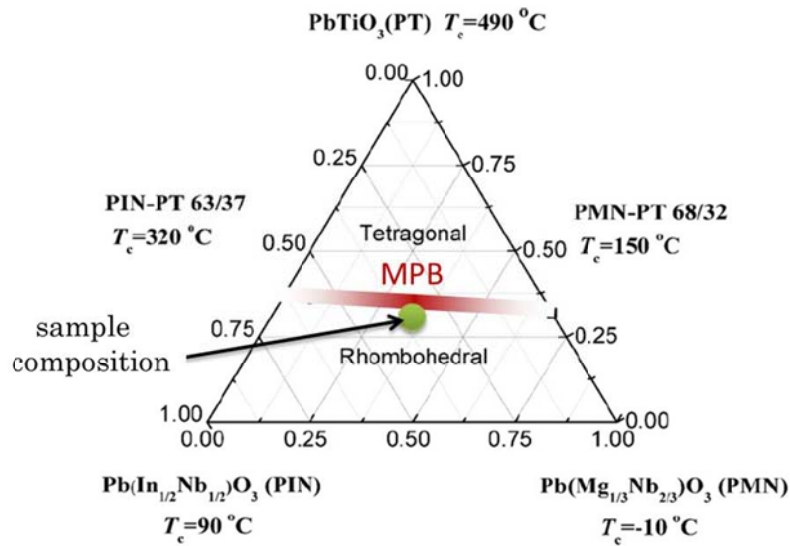

Fig. 4. 1 Phase diagram of PIN-PMN-PT [4.9].

It is well known that the exact contents of PIN, PMN and PT vary along the growth direction and that the room-temperature symmetry and electromechanical properties depend on the sample position in the grown crystal [4.8, 19]. The d_{33}, k_{33} and free dielectric constant of [001]-poled crystals were 1340~1410 pC/N, 90~91%, and ~4310, respectively, at room temperature. These results indicate that the investigated crystals can be close to the part B of Ref.4.8 and to the R(1) or R(2) single crystals of Ref.4.19. The crystal dimensions were $2 \times 11 \times 0.5$ mm³, and the largest surfaces were (001) pseudocubic planes. The Brillouin spectrum was measured in the backward scattering geometry by using a conventional tandem Fabry-Perot interferometer combined by a photomultiplier tube and a photon counting system. Gold was vacuum-sputtered to form electrodes on the largest (001) surfaces. The crystal was

inserted in a silicon oil at room temperature and was poled along the [001]c direction under a dc bias field of 15 kV/cm at 30 ^oC for one hour, where the subscript "c" represents cubic coordinates. After poling, the electrodes were removed and the Brillouin spectra were measured during the heating process. The wavelength of the excitation source was 532 nm. The polarization direction of the incident laser beam was the (001) plane, which was perpendicular to the poling direction. There was no analyzer for the scattered beam during the measurement except when it was necessary to compare the polarized and depolarized components of central peaks. Either an LCR meter (3522-50, Hioki) or the Solartron impedance analyzer (SI1260) was used to measure the dielectric permittivity upon heating.
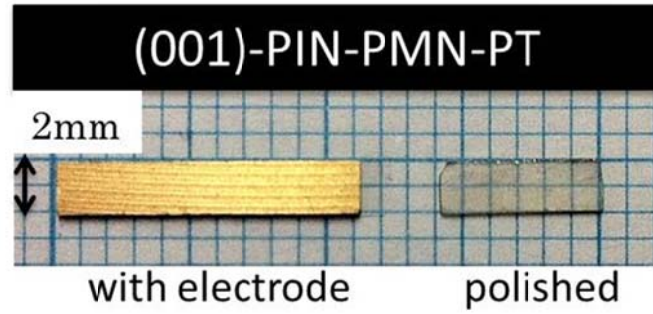
Fig. 4. 2. The (001)c-PIN-PMN-PT crystal with electrodes and the optical polished crystal.

4.3 Result and Discussion

Fig. 4. 3(a) shows three Brillouin spectra of unpoled PIN-PMN-PT at selected temperatures in a semi-log plot to put stress on the substantial changes in spectral features in a wide frequency and temperature ranges. Each spectrum consists of one Brillouin doublet corresponding to the longitudinal acoustic (LA) phonons and a central peak (CP). The absence of the transverse acoustic (TA) mode in the spectrum suggests that the average crystal symmetry is close to cubic even at low temperatures [4.22]. It is noticed that the LA mode frequency becomes softened and the CP intensity increases remarkably upon cooling. The polarized component of CP was much stronger than the depolarized component.

The Brillouin frequency shift v_B and the full width at half-maximum (FWHM) Γ_B were obtained via the following fitting procedure. The spectral response of phonon modes as a function of frequency v is usually modeled by the response function of the damped harmonic oscillator having the form;

$$I(v) = \frac{I_0}{\pi} \frac{v_B^2 \Gamma_B}{(v^2 - v_B^2)^2 + v^2 \Gamma_B^2}. \qquad (4.\ 1)$$

If v_B is much larger than Γ_B as is usual, the above form is well approximated by a Lorentzian function as

$$I(v) \propto I_0 \frac{\Gamma_B/4}{(v - v_B)^2 + \Gamma_B^2/4}, \qquad (4.\ 2)$$

where I_0 is a proportional constant. The measured spectrum I as a function of frequency v was fitted by using (4. 2) convoluted by the Gaussian instrumental function of the interferometer.
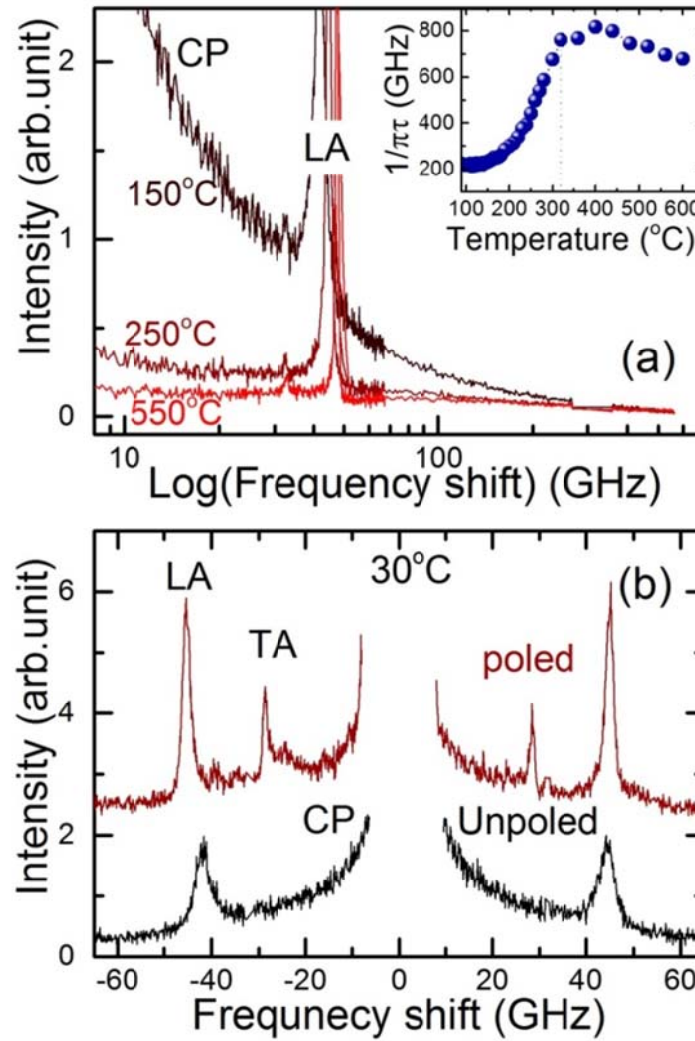
Fig. 4. 3. (a) The Brillouin spectra of [001]c‑oriented unpoled PIN‑PMN‑PT single crystals at a few temperatures in a wide frequency range (b) The Brillouin spectra of unpoled and poled single crystals measured at 30 $^o C$. The inset of (a) shows the temperature dependence of FWHM of CP which is inversely proportional to the relaxation time τ.

The Brillouin spectrum was fitted by using response functions of the damped harmonic oscillator for the phonon modes and of the single Debye relaxator for CP, from which the Brillouin frequency shift (v_B) of the acoustic phonons and the full-width at half-maximum (FWHM,Γ_B) of phonons and unpolarized CP were obtained. The inset of Fig. 4. 3(a) shows the temperature dependence of the FWHM of CP, which is equal to $1/_{\pi\tau}$, where τ is the relaxation time of the relevant process responsible for CP. In chapter 6, we discuss two relaxations of CP by using broadband light scattering spectra. The temperature dependences of v_B and Γ_B measured upon cooling and heating are shown in Fig. 4. 4(a) and (b), respectively, for the unpoled PIN-PMN-PT single crystal. The real part of the complex dielectric constant (ϵ) is also shown in Fig. 4. 4(a) for comparison. ϵ' shows maxima near 200 ^oC of which the value is more than 40000 at 10 Hz. It exhibits frequency dispersion typical in relaxors, *i.e.*, the dielectric maximum shifts to higher temperature with probe frequency. The temperature dependence of the characteristic relaxation frequency could be obtained from the dielectric maximum temperature Tm along with its probe frequency f, which was fitted by using the Vogel-Fulcher law, $f = f_0 \exp[-\frac{E}{k_B(T_m - T_{VF})}]$ where f_0 is the attempted frequency, E the activation energy, k_B the Boltzmann constant, and T_{VF} the Vogel-Fulcher temperature. The best-fitted results are shown in the inset of Fig.4. 4 (b) with parameters f_0 =4.6×10^{12} Hz, E/k_B=610 K, and T_{VF} =454 K (=182 ^oC). These values of f_0 and E/k_B are typical for relaxors.

Broad and frequency-dependent dielectric constants are correlated with the acoustic anomalies occurring in a wide temperature range. v_B shows almost a constant value at high temperatures from 400 to 600 ^oC. While v_B shows a substantial softening below ~ 320 ^oC accompanied by a significant increase in the hypersonic damping. These acoustic anomalies can be explained by the formation of PNRs and their electrostrictive coupling to the acoustic waves. As Fig.4. 3(a) shows, the growth of CP suggests the existence of polarization fluctuations. The most probable origin of these polarization fluctuations is the formation of PNRs at the so-called Burns temperature T_B, although the microscopic origin of PNRs is still not settled completely [4. 24]. The inset of Fig.4(a) indicates a sudden change in τ at about 320 ^oC, below which the relaxation time rapidly increases and Γ_B exhibit significant changes. This characteristic temperature may thus be assigned as the intermediate temperature for the present PIN-PMN-PT single crystal at which size & number of PNRs rapidly increase.

The increase in size and interactions between PNRs leads to the slowing down of their dynamics, which is reflected in both the increase in the relaxation time of CP (see the inset of Fig.4. 3(a)) and the diverging characteristic of the dielectric relaxation time represented by the Vogel-Fulcher behavior. v_B shows a minimum near 100 ^oC, and Γ_B displays a maximum at ~90 ^oC, which may be attributed to the moderately diffused transformation into short-range (or mesoscopic) polar states. This transition may be attributed to some kinetic effect, *i.e.*, the abrupt growth of PNRs at the (diffused) ferroelectric phase transition without changing the directions of their dipole moments due to the frustrated interactions between PNRs [4.25]. The

correlation length of the polar domains would be very small and the average symmetry may not deviate from the prototype cubic phase appreciably, because TA mode, which is forbidden at the backward scattering geometry in the cubic phase, is not observed at low temperatures. Typical relaxor behaviors shown from both dielectric and elastic anomalies are also consistent with the observation of the labyrinthine domain pattern [4. 18], which is typical in relaxors, confirmed from similar compositions. Large thermal hysteresis can be noticed from both v_B and Γ_B, similar to PZN-4.5%PT [4.26]. The change in v_B measured on heating became sharper at about 137 ^oC compared to the relatively broad minimum obtained upon cooling. This is accompanied by much larger Γ_B recorded upon heating than upon cooling. This thermal hysteresis may be related to the evolution of PNRs and polar domains in the low-temperature phase. This kind of aging phenomena has often been observed from non-equilibrium state in disordered systems like relaxor, dipolar glasses, spin glasses, etc.
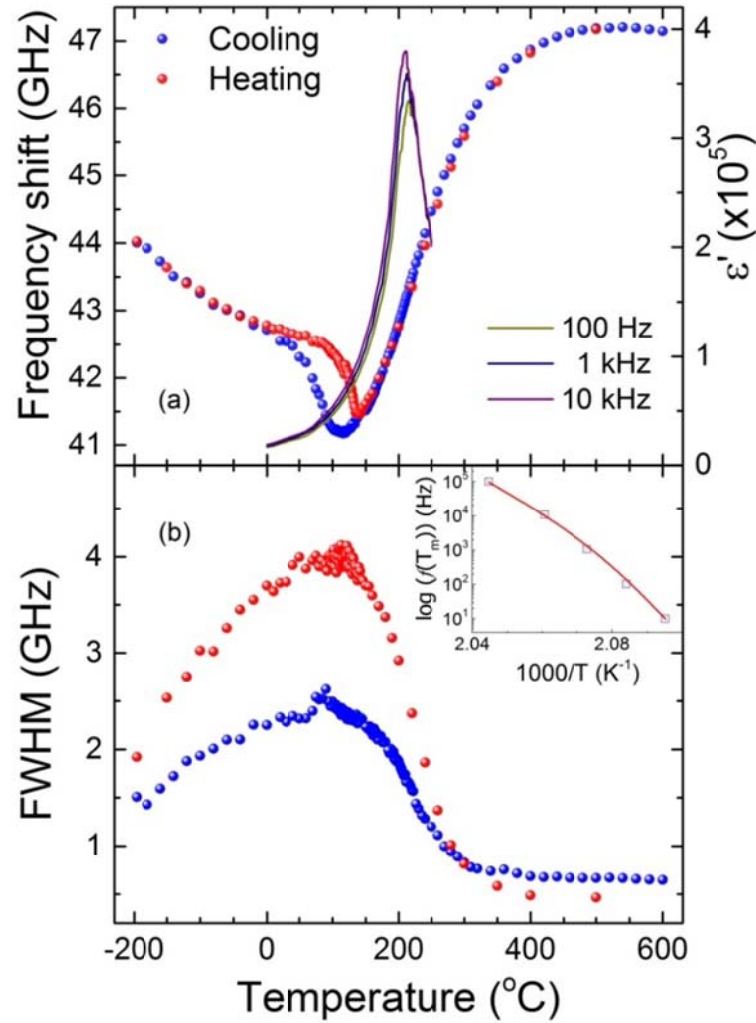

Fig. 4. 4 The temperature dependences of (a) the Brillouin frequency shift and (b) the FWHM of the LA mode of the unpoled sample measured on both cooling and heating processes. The dielectric permittivity is shown in Fig. (a) for comparison. The inset of (b) is the characteristic relaxation frequency as explained in the text in the Arrhenius plot.

Fig. 4. 3(b) shows the Brillouin spectra of the same crystal before and after poling (denoted as "unpoled" and "poled", respectively, in the figure) at 30 ^oC. The application of dc bias field of 15 kV/cm induces several interesting changes in the Brillouin spectrum: (a) hardening of the LA mode frequency and decrease in its half width, (b) suppression of the CP intensity, and (c) the appearance of the TA mode. Since the electric field of 15 kV/cm is lower than the minimum field required to induce the tetragonal symmetry [4.20], the [001]c-poled PIN-PMN-PT is expected to have a multidomain (or domain-engineered) state composed of four $< 111 >$ rhombohedral domains [4.1] and may be considered to have a tetragonal symmetry on average. In this case, the observed LA and TA modes may correspond to the C_{33} and C_{44} elastic constants, respectively.
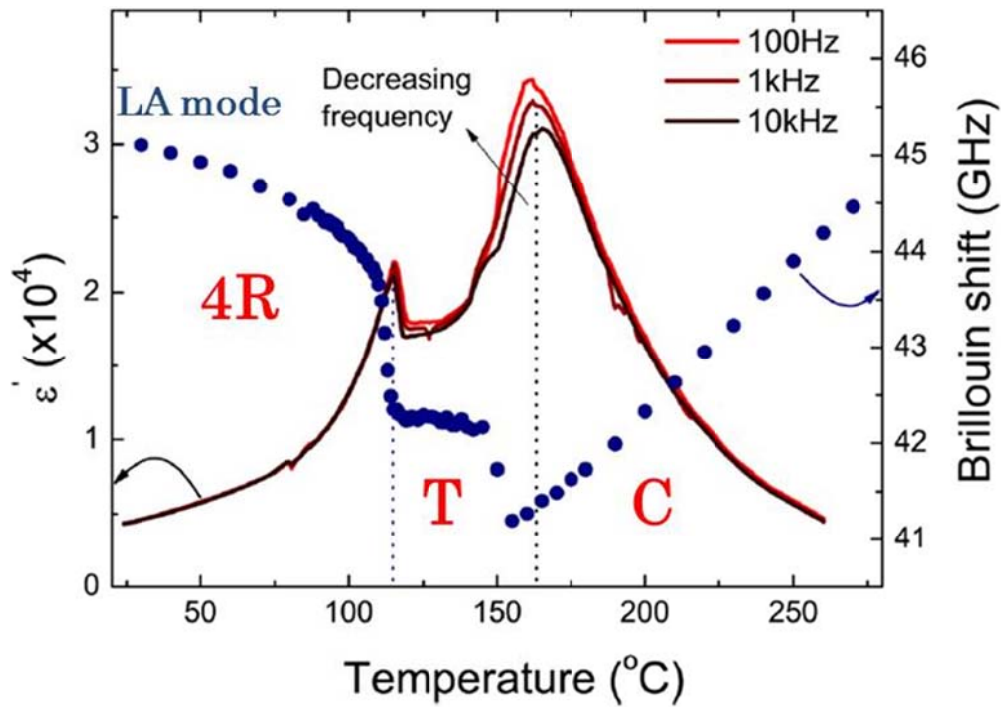
Fig. 4.5. The Temperature dependence of the dielectric permittivity and the Brillouin shift of the poled PIN-PMN-PT single crystal.

The discontinuous change in the LA mode frequency and the appearance of the TA mode can be attributed the transformation from the relaxor-like state (or slightly distorted mesoscopic ferroelectric state) into a domain-engineered state [4.1]. In addition, the fact that the TA mode persists when the dc bias field is turned off indicates that the field induced structural change remains stable even without the dc bias field. Brillouin frequency shifts were obtained at room-temperature from the measured spectrum to calculate the elastic constants of a poled sample and to compare them with previous reports. When the reported density of 8,102 kg/cm³ and the average refractive index 2.66 (at the wavelength of 546 nm) of PMN-35%PT are

54

considered [4.12,27], the elastic constants C_{33} and C_{44} of the poled sample are calculated to be 16.5 and 6.65 GPa at room temperature. These numerical values are very similar to the reported elastic constants (C_{33}^D=16.7 and C_{44}^D= 7.0 GPa) of the [001]c-poled PIN-PMN-PT single crystal of a similar composition obtained in terms of the resonance method [4.8]. This result seems to suggest that acoustic dispersion effect between the resonance technique and hypersonic Brillouin scattering might be very small in PIN-PMN-PT of this composition.
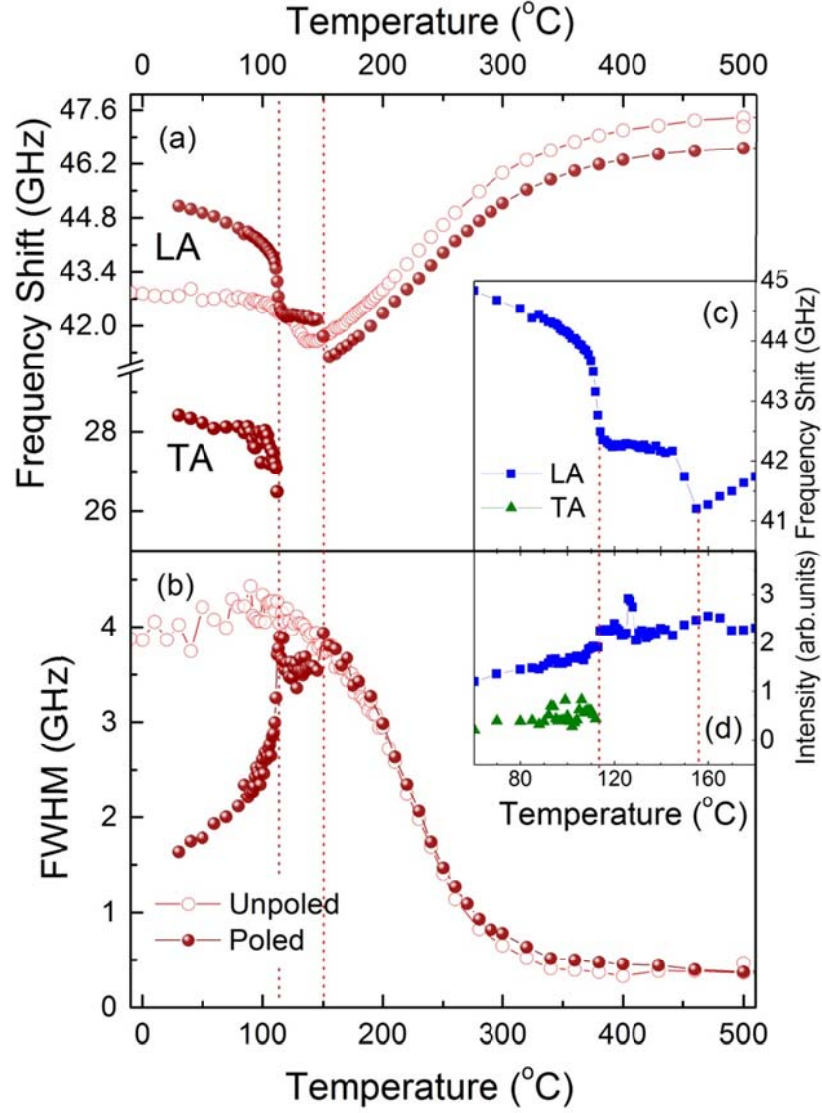
Fig. 4. 6. The temperature dependences of (a) the Brillouin frequency shift and (b) the FWHM of the LA and TA modes of both the unpoled and poled samples measured on heating process. The insets (c) and (d) show the extended plot of v_B and the mode intensities of the poled sample near the ferroelectric phase transitions, respectively.

Fig.4.5 shows the Brillouin shift of the LA mode along with the dielectric data of the poled sample as a function of temperature measured upon heating. The dielectric permittivity shows two clear anomalies at ~116 ^oC and ~165 ^oC consistent with dielectric properties of previous study carried out on similar compositions [4. 20]. In addition, these two dielectric anomalies are correlated with the step-like changes in the elastic property. The fact that the high-temperature anomalies of both measurements do not appear at exactly the same temperature is not surprising, because the dielectric anomaly has some frequency dispersion and the dielectric maximum temperature depends on the probe frequency. The comparisons of the temperature dependence of v_B and Γ_B of unpoled and poled samples are shown in Fig. 4. 6 (a) and (b), respectively, obtained at the heating process.

The two insets (c) and (d) of Fig. 4. 6 show the extended plot of v_B of the LA mode and the intensity changes of both modes, respectively, of the poled sample near the ferroelectric phase transitions. The temperature dependence of v_B and Γ_B clearly shows that the two step-like changes in v_B are correlated to the hypersonic damping peaks at almost the same temperatures. The inset (d) of Fig. 4. 6 shows that the TA mode intensity becomes zero at ~116 ^oC, which is a clear evidence for a structural phase transition at this temperature. Based on the observed transition temperatures and comparison with previous studies [4.20], we attribute the observed two dielectric and elastic anomalies to the successive phase transitions from rhombohedral to tetragonal and then from tetragonal to cubic phases with increasing temperature.
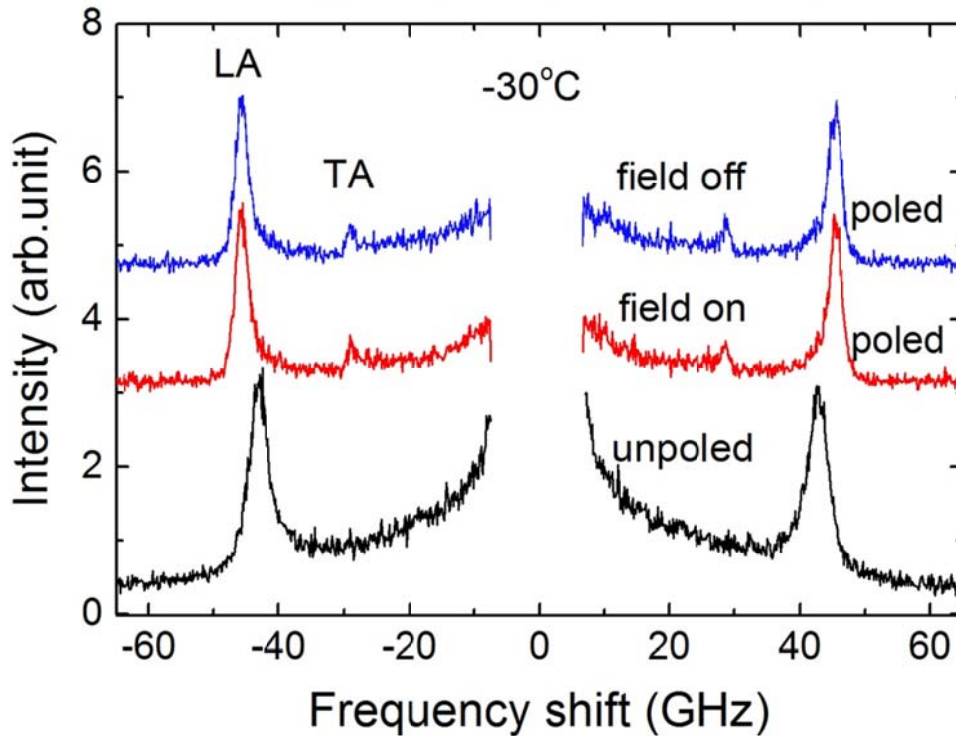

Fig. 4. 6. The Brillouin spectra at -30 ^oC with dc field (red line), after turned off field (blue line).

We note that the tetragonal-cubic phase transition at high-temperature remains somewhat diffused characterized by the frequency dispersion and a smeared change in v_B compared to PMN-xPT [4.25]. The diffuseness of the dielectric property at the Curie temperature has also been observed from other PIN-PMN-PT single crystals [4.8,20] which is in contrast to the sharp, discontinuous changes in the dielectric and elastic properties of PZN-xPT and PMN-xPT near MPB at the cubic-tetragonal phase transition temperature. This may be understood based on the suggestion by Chen *et al.* on the intermediate state below the dielectric maximum temperature on approaching the cubic phase [4.21]. They reported that [001]-oriented 0.34PIN-0.25PPM-0.41PT exhibited an intermediate state via which transformation from macrodomain to microdomain states occurs. The macroscopic long-range polar order formed under high dc bias field does not disappear abruptly at the phase transition but changes into microdomains due to inherent disorder and random fields in relaxors. Finally, we point out that the temperature range of the intermediate tetragonal phase may be changed and controlled depending on the previous poling treatment. When the crystal was poled under the same electric field at $-30\ ^oC$ and the Brillouin spectrum was measured upon heating without the dc bias field as Fig. 4. 7, the temperature dependence of v_B and Γ_B showed two clear anomalies at $\sim100\ ^oC$ and $\sim125\ ^oC$. This means that the intermediate temperature range can be reduced significantly by using poling at lower temperatures.

4.4 Conclusions

  In conclusion, we compared the phase transition behaviors of unpoled and [001]c-poled PIN-PMN-PT single crystals by using Brillouin light scattering and dielectric spectroscopies. The unpoled sample showed broad elastic softening along with substantial dielectric dispersion, which is typical in relaxors. The Burns temperature was determined to be about 550 ℃ by observing the spectral changes in central peaks and the corresponding change in the relaxation time. The small damping peak at $\sim90\ ^oC$ was attributed to the development of moderately diffused and short-ranged (or mesoscopic) polar state due to the abrupt growth and merging of polar nanoregions without changing the directions of their dipole moments. Poling the crystal under DC bias field of 15 kV/cm along the [001]c direction gave rise to the appearance of the TA mode, suppression of the central peak, and substantial changes in the LA mode properties, indicating structural transformation from the short-range polar state into a domain-engineered rhombohedral state. The temperature dependence of dielectric and elastic properties of the poled sample exhibited two clear anomalies at $\sim116\ ^oC$ and $\sim165\ ^oC$. These two-step changes were attributed to the successive phase transitions from rhombohedral to tetragonal and then from tetragonal to cubic phases with increasing temperature based on the observed transition temperatures and comparison with previous

studies. The high-temperature tetragonal-cubic phase transition remained diffused even for the poled sample, which may be understood as the transformation of macrodomains into microdomains upon heating due to local random fields inherent in relaxors.

References

[4.1] S.-E. Park, and T. R. Shrout, J. Appl. Phys., **82** (1997) 1804.

[4.2] Z. -G. Ye, *Handbook of Advanced Dielectric, Piezoelectric, and Ferroelectric Mater: Synthesis Characterization and Applications*, (Woodhead, Cambridge, 2008).

[4.3] F. Li, S. Zhang, Z. Xu, X. Wei, and T. R. Shrout, Adv. Funct. Mater., **21** (2011) 2118.

[4.4] Y. Hosono, Y. Yamashita, K. Hirayama, and N. Ichinose, Jpn. J. Appl. Phys., **44** (2005) 7037.

[4.5] G. Xu, K. Chen, D. Yang, and J. Li, Appl. Phys. Lett., **90** (2007) 032901.

[4.6] J. Tian, P. Han, X. Huang, H. Pan, J. F. Carroll III and D. A. Payne, Appl. Phys. Lett., **91**, (2007) 222903.

[4.7] P. Yu, F. Wang, D. Zhou, W. Ge, X. Zhao, H. Luo, J. Sun, X. Meng, and J. Chu, Appl. Phys.Lett., **92** (2008) 252907.

[4.8] S. Zhang, J. Luo, W. Hackenberger, and T. R. Shrout, J. Appl. Phys., **104** (2008) 064106.

[4.9] X. Li, Y. Wang, L. Liu, X. Zhao, H. Luo, D. Lin, Mater. Chem. Phys., **122** (2010) 350.

[4.10] S. Zhang, J. Luo, W. Hackenberger, N. P. Sherlock, R. J. Meyer, Jr., and T. R. Shrout, J. Appl.Phys., **105** (2009) 104506.

[4.11] X. Liu, S. Zhang, J. Luo, T. R. Shrout, and W. Cao, J. Appl. Phys., **106** (2009) 074112.

[4.12] X. Liu, S. Zhang, J. Luo, T. R. Shrout, and W. Cao, Appl. Phys. Lett., **96** (2010) 012907.

[4.13] E. Sun, S. Zhang, J. Luo, T. R. Shrout, and W. Cao, Appl. Phys. Lett. **97** (2010) 032902.

[4.14] P. Finkel, H. Robinson, J. Stace, and A. Amin, Appl. Phys. Lett. **97** (2010) 122903).

[4.15] S. Zhang, F. Li, J. Luo, R. Xia, W. Hackenberger, and T. R. Shrout, Appl. Phys. Lett., **97** (2010) 132903.

[4.16] F. Li, S. Zhang, Z. Xu, X. Wei, J. Luo, and T. R. Shrout, J. Appl. Phys., **107** (2010) 054107.

[4.17] W. Wang, D. Liu, Q. Zhang, B. Ren, Y. Zhang, J. Jiao, D. Lin, X. Zhao, and H. Luo, J. Appl.Phys., **107** (2010) 084101.

[4.18] Q. Li, Y. Liu, J. Schiemer, P. Smith, Z. Li, R. L. Withers, and Z. Xu, Appl. Phys. Lett., **98** (2011) 092908.

[4.19] P. Finkel, K. Benjamin, and A. Amin, Appl. Phys. Lett., **98** (2011) 192902.

[4.20] F. Li, S. Zhang, D. Lin, J. Luo, Z. Xu, X. Wei, and T. R. Shrout, J. Appl. Phys., **109**

(2011) 014108.

[4.21] Y. Chen, K. H. Lam, D. Zhou, X. S. Gao, J. Y. Dai, H. S. Luo, and H. L. W. Chan, J. Appl. Phys., **109** (2011) 014111.

[4.22] S. Zhang, G. Liu, W. Jiang, J. Luo, W. Cao, and T. R. Shrout, J. Appl. Phys., **110** (2011) 064108.

[4.23] R. Vacher, and L. Boyer, Phys. Rev. B, **6** (1972) 639.

[4.24] A. A. Bokov, and Z. -G. Ye, J. Mater. Sci., **41** (2006) 313.

[4.25] J. -H. Ko, D. H. Kim, S. Tsukada, S. Kojima, A. A. Bokov, and Z. -G. Ye, Phys. Rev. B, **82** (2010) 104110.

[4.26] J. -H. Ko, D. H. Kim, S. Kojima, W. Chen, and Z. -G. Ye, J. Appl. Phys., **100** (2006) 066106.

[4.27] C. He, F. Wang, D. Zhou, X. Zhao, D. Lin, H. Xu, T. He, and H. Luo, J. Phys. D: Appl. Phys., **39** (2006) 4337.

Chapter 5. Phase transition behaviors in relaxor ferroelectric [011]-poled Pb(In$_{1/2}$Nb$_{1/2}$)O$_3$–Pb(Mg$_{1/3}$Nb$_{2/3}$)O$_3$–PbTiO$_3$ single crystals studied by Brillouin light scattering

5. 1 Introduction

The origin of the ferroelectric phase transition in the relaxor ferroelectrics is still in controversy. In the last chapter, we discussed acoustic and dielectric properties of [001]c-poled and unpoled PIN-PMN-PT crystals and determined Curie temperature, T_{RT}, T^*, and T_{VF}. In this chapter, we report on the experimental results of a [001]c-poled crystal and discussion.

In this chapter, we report [011]c-oriented xPIN-(1-x-y)PMN-yPT (x=0.26, y=0.28) single crystals under different poling conditions by using micro-Brillouin scattering and dielectric spectroscopies over a wide temperature range between 20 and 700 °C during both cooling and heating processes. This is a complementary work to our previous study of the last chapter, where [001]c-oriented PIN-PMN-PT single crystals were studied by Brillouin and dielectric spectroscopies.

5. 2 Experimental

The ternary 0.26PIN-0.46PMN-0.28PT single crystals used in the current study were supplied by TRS Technologies Inc. Samples were oriented along the [011]c direction and the largest (011) surfaces were vacuum-sputtered by gold to apply an external electric field. Electric poling was achieved by applying a dc bias field of 15 kV/cm to a crystal immersed in silicone oil at room temperature.

Complex dielectric constant and Brillouin spectra were obtained from the same system of the last chapter. Additionally, a forward symmetric scattering geometry was used to measure the sound velocity in GHz range. From this geometry, we don't need refractive index in order to calculate the sound velocity.
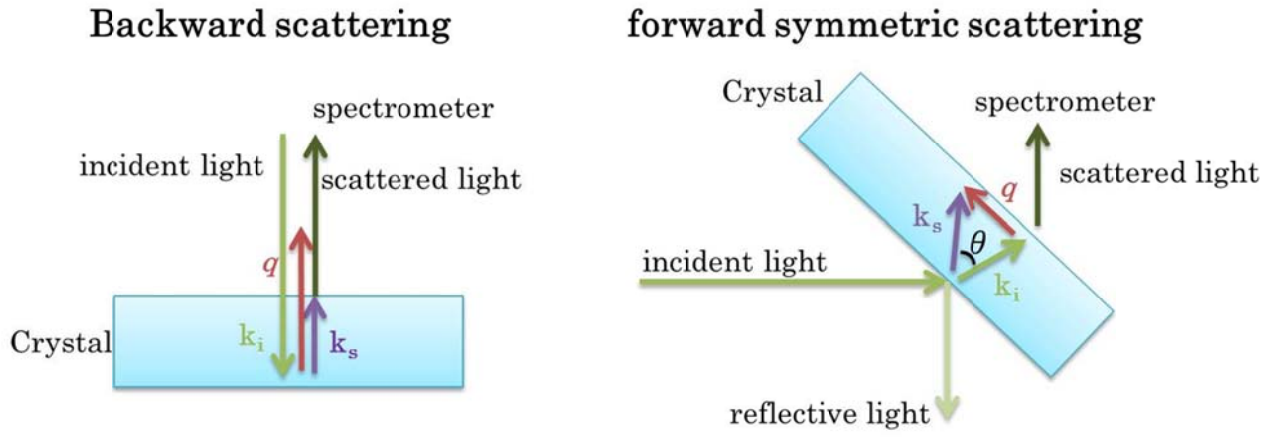
Fig. 5.1. Backward scattering and forward symmetric scattering geometries.
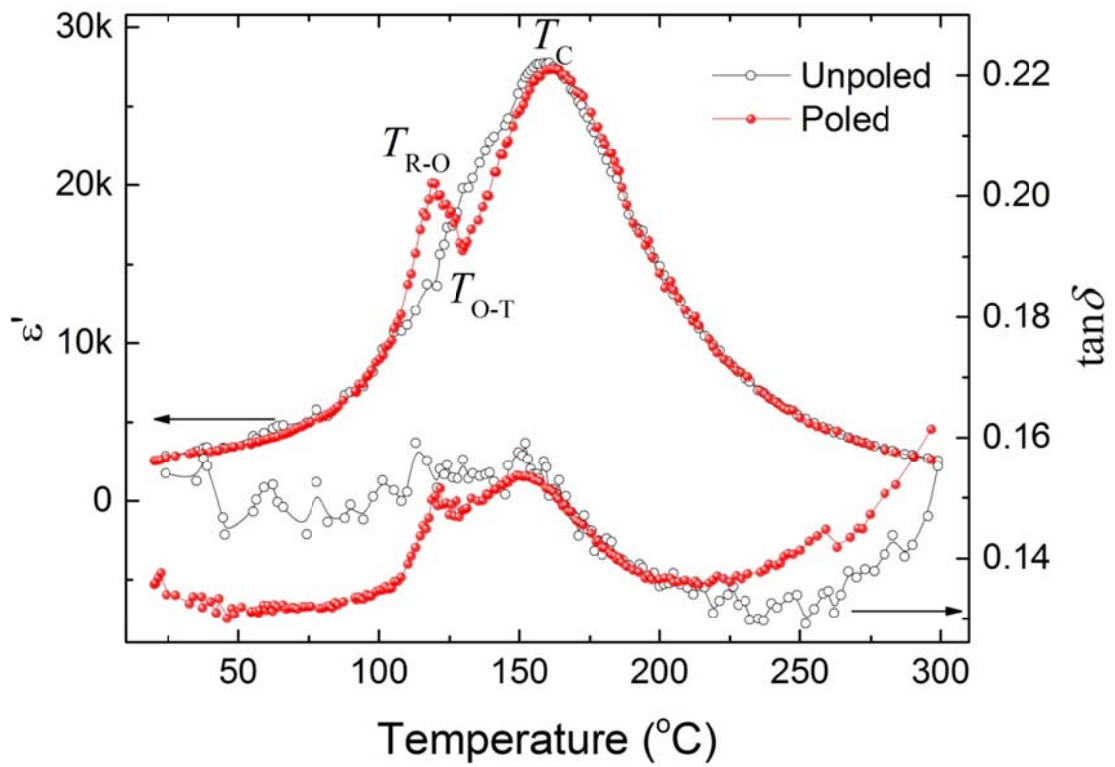
5. 3 Results and Discussion

Fig. 5. 2. Dielectric permittivity and loss tanδ as a function of temperature for [011]c-poled and unpoled PIN-PMN-PT single crystals measured at 1kHz during heating process.

Fig. 5. 2 shows the temperature dependence of the real part of the complex dielectric constant ($\varepsilon' + \varepsilon''$) and the dielectric loss ($\tan\delta = \varepsilon''/\varepsilon'$) of [011]c-poled and unpoled PIN-PMN-PT single crystals, where ε' and ε'' are the real and imaginary parts of the complex dielectric constant, respectively. The data were measured upon heating at a probe frequency of 1 kHz. The Curie temperature T_C of both samples can be determined as the temperature of the dielectric maximum, which is approximately 160 °C. For the poled crystal, ε' shows two sharp anomalies at ~119 and ~126 °C, below T_C. Similar dielectric anomalies were also observed for [011]c-poled, Mn-doped 0.26PIN-0.42PMN-0.32PT, which were attributed to rhombohedral-monoclinic and monoclinic-tetragonal phase transitions [5.9]. We attribute the two anomalous temperatures of the poled sample to the rhombohedral-orthorhombic ($T_{R\text{-}O}$) and orthorhombic-tetragonal ($T_{O\text{-}T}$) transition temperatures considering a previous report [5.11] and the fact that poling along the [011]c direction induces the orthorhombic phase on an averaged structure. On the other hand, unpoled PIN-PMN-PT exhibits one broad dielectric maximum, which is considered to be the phase transformation from the rhombohedral phase to the cubic phase without the intermediate orthorhombic phase [5.1,5]. This is consistent with a recent neutron diffraction study on PIN-PMN-PT of the same composition, which showed that the unpoled crystal maintained an average rhombohedral phase from room temperature to T_C [5.12].

The dielectric property of the unpoled sample, shown in Fig. 5. 2, exhibits typical relaxor characteristics, such as diffuseness and deviation from the Curie-Weiss law. The temperature dependence of ε' may thus be analyzed by using an empirical relation that has been applied to relaxors. We adopted the extended Curie-Weiss law [5.13] as given below to fit the dielectric data of Fig. 1 in the paraelectric phase;

$$\frac{1}{\varepsilon'(v,T)} = \frac{1}{\varepsilon_{max}(v)}\left\{1 + \frac{[T - T_m(v)]^\gamma}{2\delta_\gamma^2}\right\}, \tag{5. 1}$$

where $\varepsilon_{max}(v)$ and $T_m(v)$ are the magnitude of the dielectric peak and the dielectric maximum temperature at the probe frequency v, respectively. γ and δ_γ are fitting parameters indicating the degree of the diffuseness of the phase transition. Fig. 5. 3 shows the inverse of $\varepsilon'(v,T)$ and the best-fitted results obtained by Eq. 5.1. The obtained parameters are summarized in Table 5. I. According to this result, γ is close to 2, which means that typical relaxor behavior is confirmed from unpoled 0.26PIN-0.46PMN-0.28PT. This may be attributed to the enhanced frustration of B-site cations in this ternary system compared with in the binary relaxor system.

Table 5. I. The obtained parameters for the dielectric constant of unpoled PIN-PMN-PT by using Eq. 5.1 and calculated sound velocity in by using Eq.5. 2 compared with other method.

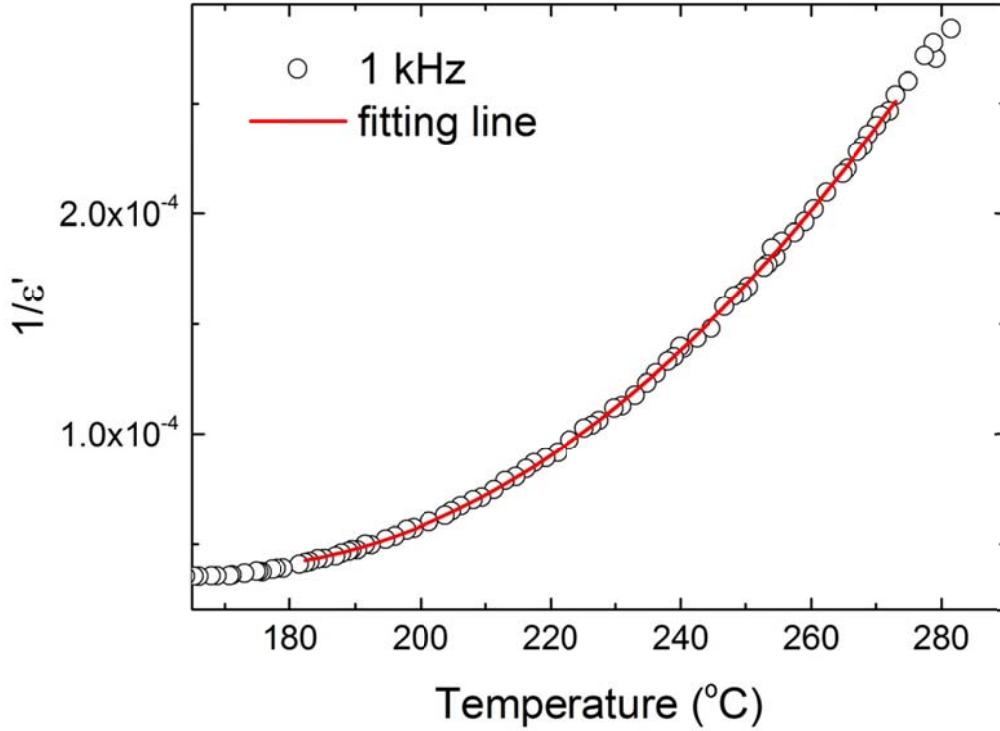| condition	$\varepsilon_{\max}(v)$	T_m (°C)	γ	δ_γ	condition	$V_{Brillouin}$ (m/s)	$V_{ultrasonic}$[§] (m/s)
unpoled	25638	169	1.99	31.6	poled	4683	4746

[§](composition :0.25PIN-0.47PMN-0.28PT

Fig. 5. 3. Inverse of dielectric permittivity measured at 1 kHz and best-fitted results (solid line) obtained by Eq. 5.1.

Figures 5. 4(a) and 4(b) respectively show the Brillouin spectra of poled and unpoled PIN-PMN-PT at a few selected temperatures along with fitting lines, as explained in the next paragraph. The Brillouin doublet appearing at about ±50 GHz is due to the scattering of longitudinal acoustic (LA) phonons propagating along the [011]c direction. Also, a central peak (CP), which is related to the relaxation process of dynamic PNRs, appears in the paraelectric phase and grows as it approaches T_C. A strong CP appears in both the poled and unpoled conditions below T_C, while its intensity decreases markedly upon heating to above T_C. For the poled sample, a TA mode clearly appears at about ±31 GHz, as shown in Fig. 5. 4(a), with an additional low-frequency broad peak near ±9 GHz below ~119 °C. The appearance of the TA mode is a clear indication of symmetry lowering from the cubic phase due to the appearance of macroscopic domain structures, which is consistent with the dielectric anomaly shown in Fig. 5. 2. In contrast, the absence of the transverse acoustic (TA) mode in the spectrum of Fig. 5. 4(b) indicates that the average symmetry of the unpoled sample is essentially cubic because of quenched mesoscopic or nanoscale fine domain structures even at low temperatures below T_C [5.26]. The origin of the lowest frequency mode and its relation to a ferroelectric phase transition is discussed separately in the last of this section.
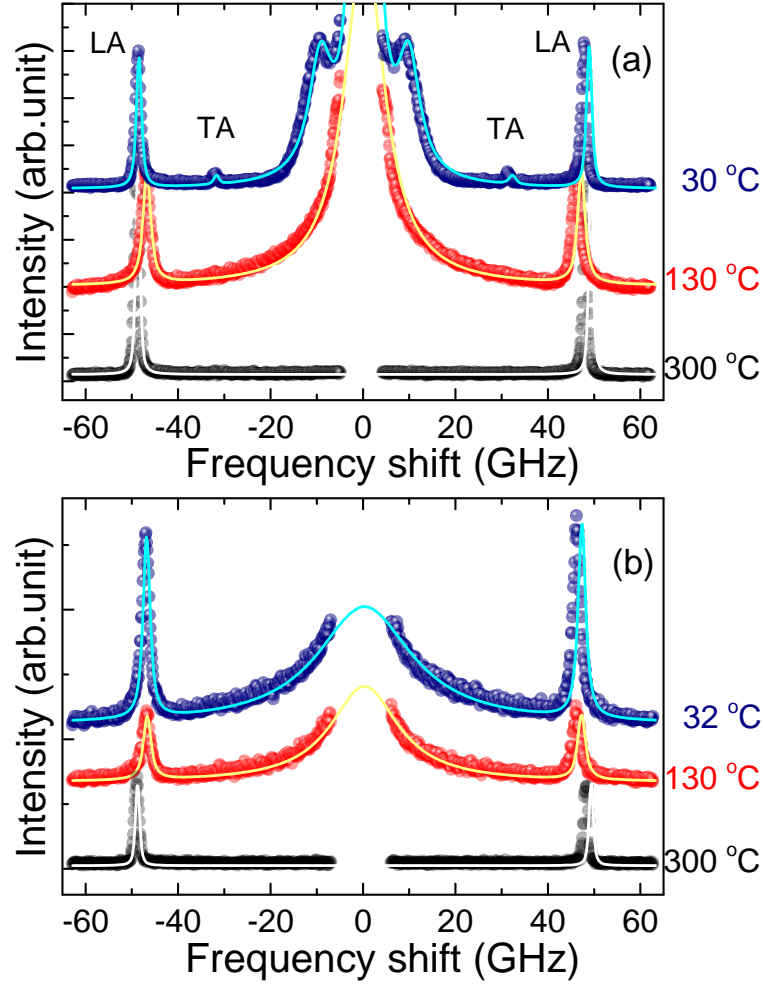
64

Fig. 5. 4 Brillouin spectra of (a) poled and (b) unpoled PIN–PMN–PT single crystals measured at a few selected temperatures (solid circles) along with fitting lines.

The Brillouin spectra were fitted by the superposition of two kinds of response functions consisting of damped harmonic oscillators for the LA (and TA) mode(s) and a single Debye relaxator for the CP. Fig. 5. 5(a) and 5(b) respectively show the Brillouin frequency shift (v_B) and its full width at half maximum (FWHM, Γ_B) of the LA mode of the unpoled sample as functions of temperature. It is found that v_B exhibits significant softening upon cooling toward T_C. The temperature range above T_C in which the mode softening occurs amounts to ~300 ^{o}C, which can be ascribed to the coupling with polarization fluctuations of dynamic PNRs in the cubic phase. In contrast, Γ_B is almost constant above about 300 ^{o}C and grows upon cooling toward T_C, which is very similar to the cases of PMN and PMN-0.15PT [5.15]. The characteristic temperature of PNRs in unpoled PIN-PMN-PT are also known: $T_B = 590$ ^{o}C,

65

$T^* = 320 \,^{\circ}\text{C}$. This enhancement of the acoustic damping near T_C is related to the slowing down of the dynamics of PNRs, which is related to the narrowing of the CP. Large thermal hysteresis can be observed from v_B, which suggests the first-order nature of the diffuse phase transition between cubic and rhombohedral symmetry at T_C.   The sound velocity of the poled sample was measured at room temperature in the forward, symmetric scattering geometry by using Eq. 5.2 [5.16].

$$V = \frac{v_B \lambda}{2n \sin\frac{\theta}{2}},$$
(5.2)

where λ, n, and θ are incident wavelength (532 nm), refractive index (2.66), and scattering geometry angle (60°), respectively

  The obtained sound velocity of the LA mode is 4,683 m/s, which is close to the value for PIN-PMN-PT of a similar composition measured by the ultrasonic technique [5.17]. These sound velocities are given in Table 5. I. Such closeness was also confirmed for [001]c-oriented 0.26PIN-0.46PMN-0.28PT. These two results suggest that the acoustic dispersion effect in the frequency range between 15 MHz (ultrasonic technique) and 45 GHz (Brillouin scattering) may be negligible in PIN-PMN-PT at room temperature. That is, the frequency dependence of the sound velocity is very small in the frequency range from 15 MHz to 45 GHz.
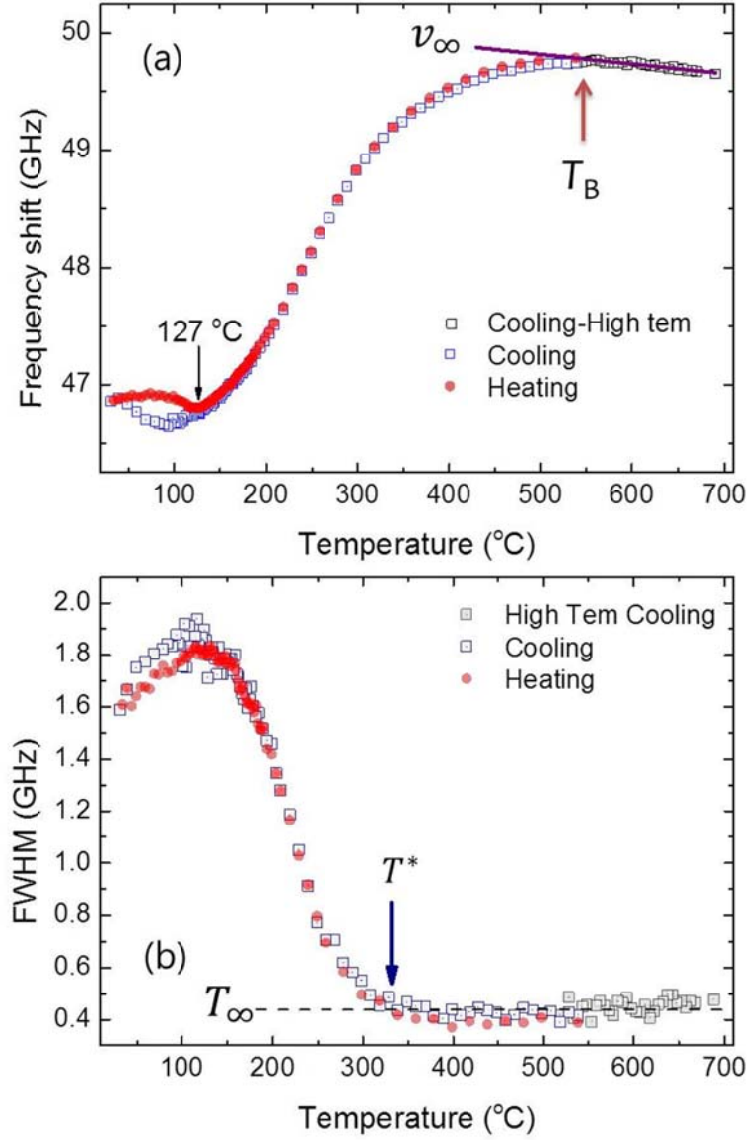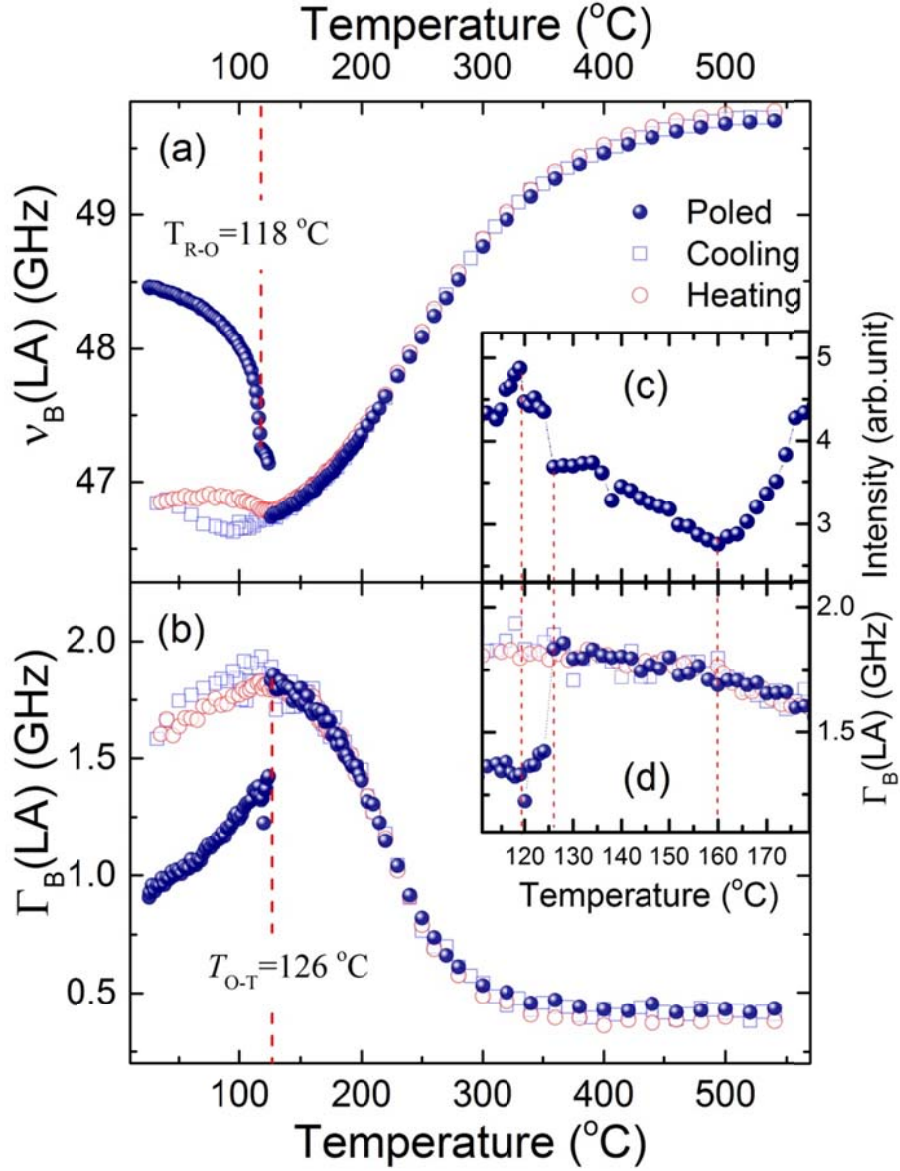
Fig. 5. 5. Temperature dependence of (a) Brillouin frequency shift and (b) FWHM of the LA mode of the unpoled sample measured during both cooling (blue and black open squares) and heating (red circles) process.

Figures 5. 6(a) and 5. 6(b) show comparisons of the temperature dependences of v_B and Γ_B, respectively, between unpoled and poled crystals. The two insets display extended views of the temperature dependences of the LA mode intensity and Γ_B near the phase transition temperatures. Fig. 5. 7 shows the comparison between ε' and v_B of poled samples. v_B of the TA mode is also shown. These two comparisons in Figs. 5. 6 and 5. 7 reveal the interesting phase transition behaviors of PIN-PMN-PT.

Fig. 5. 6. Temperature dependences of (a) Brillouin frequency shift and (b) FWHM of the LA of the poled sample measured during heating (blue solid circles) and the unpoled sample measured during both cooling (blue open squares) and heating (red open circles) processes. Insets (c) and (d) show extended plots of the LA mode intensity and the FWHM of the poled sample near the phase transition temperatures, respectively.

(i) v_B and Γ_B do not show any noticeable differences between the poled and unpoled crystals over a wide temperature range down to ~126 ℃ (T_{O-T}), that is, the LA mode softening extends to temperatures below T_C. Only the kink in the temperature dependence of the mode intensity, shown in Fig. 5. 6(c), is the signature of a diffuse phase transformation at T_C. The continuous softening of v_B down to a temperature well below T_C was also observed from [001]-poled and [111]c-poled PIN-PMN-PT single crystals studied by Brillouin scattering and resonant

68

ultrasonic spectroscopy [5.6]. These results clearly show that the diffuse phase transition near T_C is not affected by the poling process. The present results also suggest that T_{O-T} may be understood as the depolarization temperature where the field-induced macroscopic ferroelectric domains induced by poling at room temperature are decomposed into mesoscopic polar domains coexisting with dynamic PNRs. Therefore, the phase of the poled crystal between T_{O-T} and T_C is expected to be nearly the same as that of the unpoled one from the macroscopic point of view, and the coupling of the dynamic PNRs to the acoustic waves dominates the acoustic properties in both samples. The diffuseness together with the dielectric dispersion near T_C was attributed to tweed domain structures and the competition between the antiferroelectric and ferroelectric ordering similarly to in relaxor states [5.2-3].
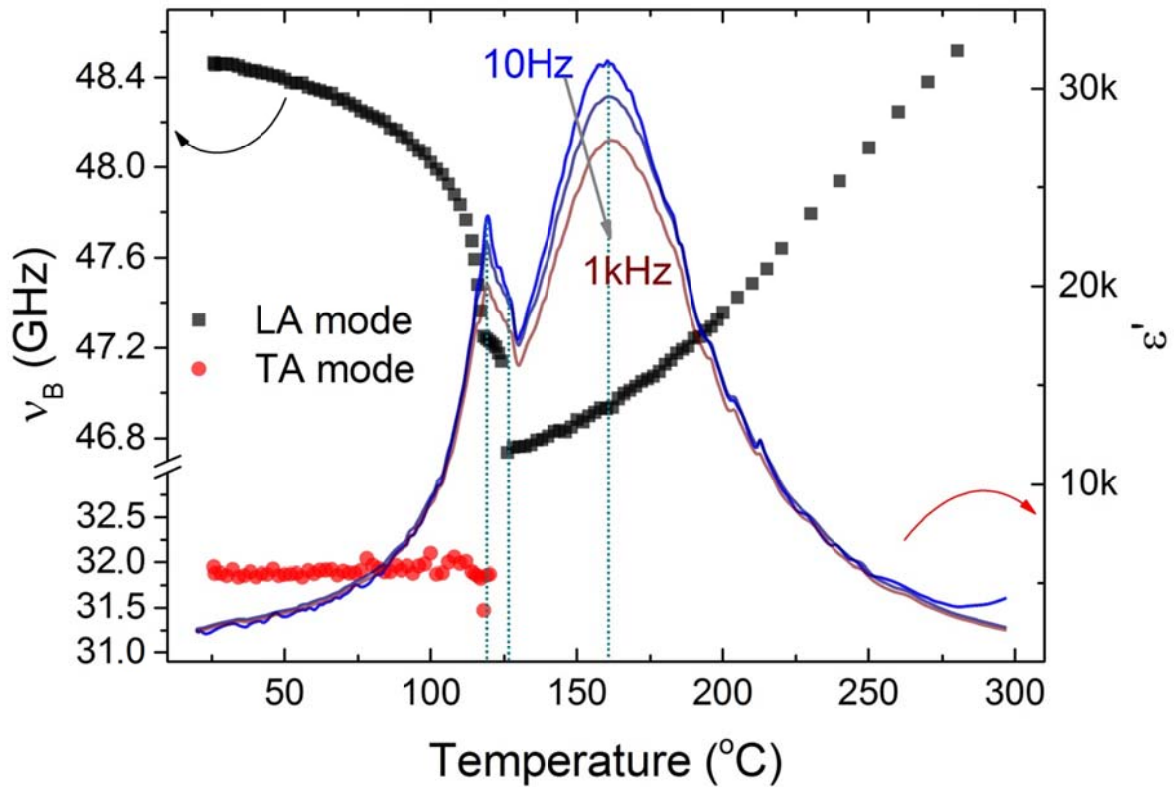
Fig. 5. 7. Dielectric permittivity (solid lines) and Brillouin frequency shift of the LA (black solid squares) and TA modes (red solid circles) as functions of temperature for the [011]c-poled PIN–PMN–PT single crystal.

(ii) Both v_B and Γ_B exhibit discontinuous changes at T_{O-T} for the poled sample. In addition, the two step like changes in v_B occur at nearly the same temperatures as where the dielectric anomalies appear, as can be seen in Fig. 5. 7. The temperature dependences of Γ_B and the mode intensity exhibit either a small discontinuity or a kink at T_{R-O} and T_{O-T}. In addition, T_{R-O} is characterized by the appearance of the TA mode. It is clear that Γ_B of the poled crystal in

the rhombohedral phase is substantially smaller than that of the unpoled one. Poling the sample along the [011]c direction can decrease the density of twin domain walls and static/dynamic PNRs, which is expected to reduce the interaction between the acoustic waves and the fluctuating polar regions and/or the mobile interfaces between domains, resulting in lower acoustic damping in the poled condition. These changes are in agreement with similar changes in damping behaviors induced by the poling process observed for [001]c-poled and [111]c-poled PIN-PMN-PT single crystals [5.6].
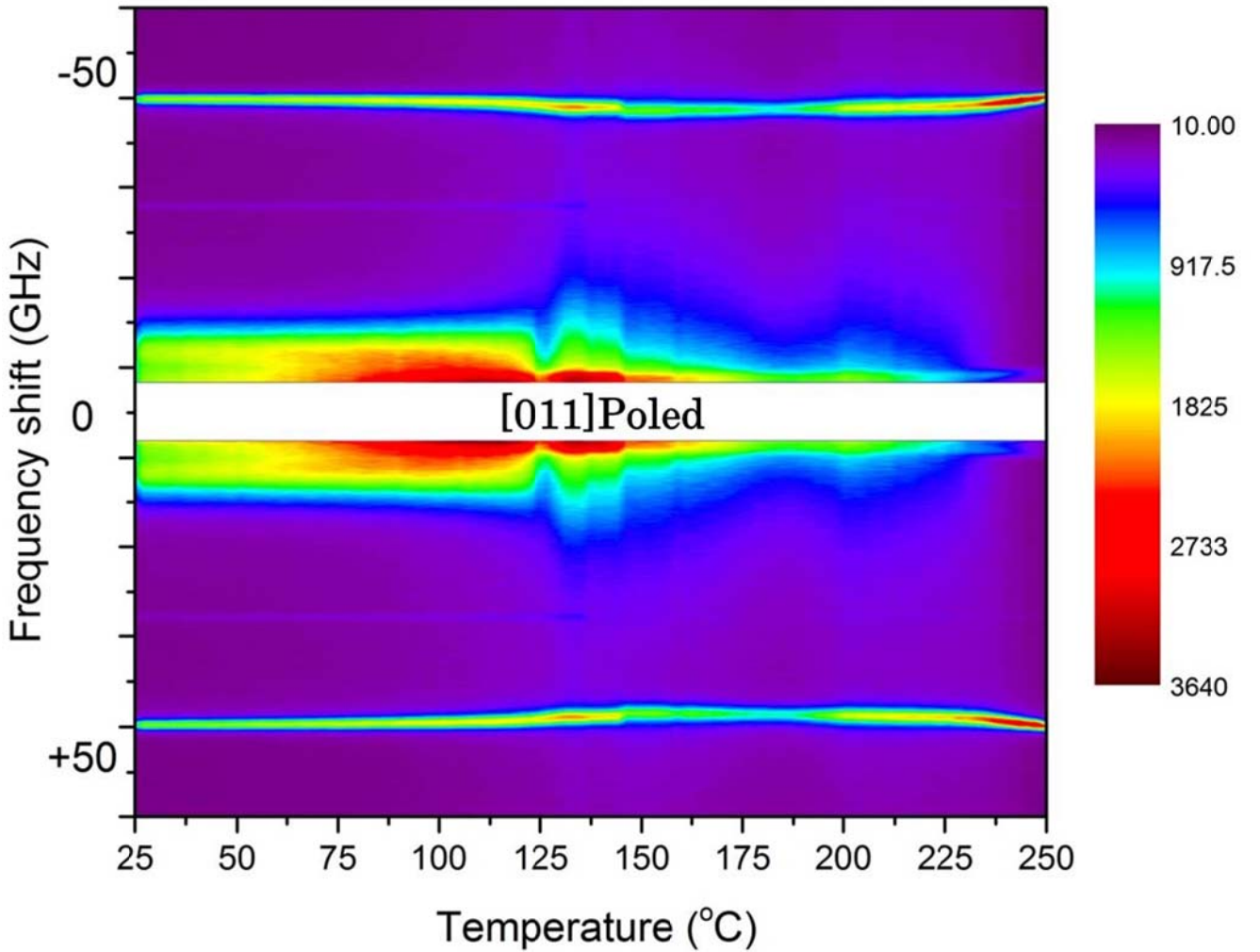
Fig. 5. 8. Contour map of Brillouin scattering intensity from [011]c-poled PIN-PMN-PT crystal vs. temperature and frequency shift in the back scattering geometry.

Fig. 5. 8 shows the contour map of the Brillouin scattering intensity of [011]c-poled PIN-PMN-PT as a function of frequency shift and temperature under the geometry of 180°. The low frequency peak only appears in depolarized spectra below $T_{O\text{-}T}$ with higher intensity than other peaks. It seems coupled mode with CP below $T_{O\text{-}T}$. Also, the low frequency peak follows soft mode behavior but diverse both the peak position and the FWHM near $T_{O\text{-}T}$ as Fig. 5. 9.

70

However, this peak does not allow the selection rule of the present scattering geometry. In order to find the origin of the low frequency peak, we performed forward scattering on [011]c-poled and unpoled samples.
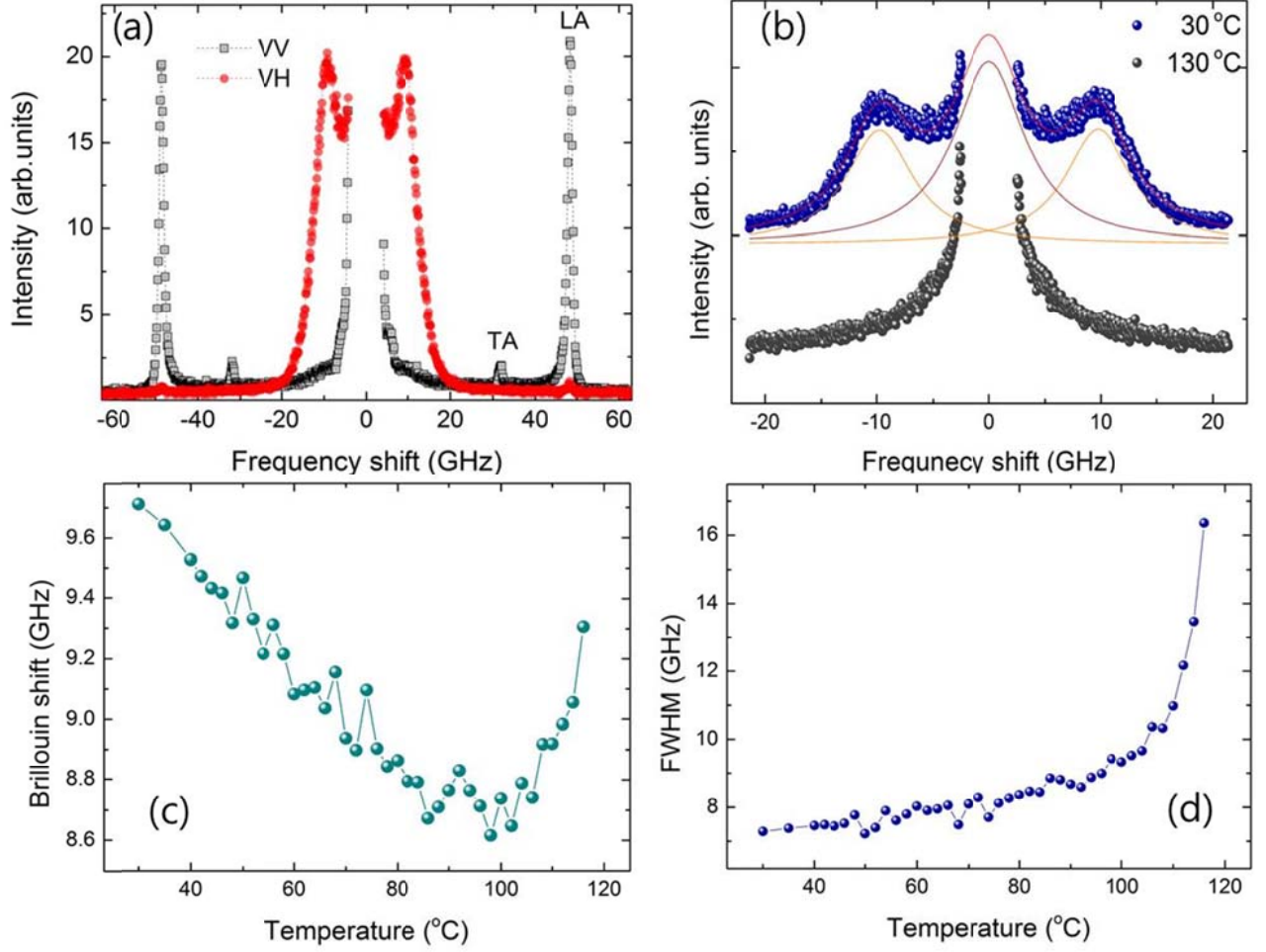

Fig. 5. 10. (a) The Brillouin spectra in polarized (red circles) and depolarized mode. (b) The Brillouin spectra in FSR=25 GHz with best fitted line at a few selected temperatures. Temperature dependences of (c) Brillouin shift and (b) FWHM of a low frequency peak of the [011]c-poled sample measured during heating.

We expect that it is related the phonon propagation direction, because v_B of a low frequency peak is similar to v_B of LA mode position by obtained in the forward scattering. In TEM image, only large size micro/macro cracks between domain structures appeared in a [011]c-poled sample [5.16]. From the phenomena, other axis (or axes) will be formed by [011]c-poled process. Therefore, a low frequency peak may propagate both [011]c and vertical of [011]c.

5. 4 Conclusion

The phase transition sequences of [011]c-oriented 0.26PIN-0.46PMN-0.28PT single crystals were investigated under different poling conditions by dielectric and Brillouin spectroscopies. The unpoled sample showed a diffuse, frequency-dependent dielectric maximum, which was accompanied by broad elastic softening and acoustic damping of the LA mode. The Brillouin shift of the LA mode exhibited continuous softening down to a temperature well below the Curie temperature, which suggests that the coupling of the fluctuating dynamic PNRs to the acoustic waves plays the dominant role in the acoustic anomalies near the Curie temperature. Poling the crystal along the [011]c direction induced two abrupt changes in both dielectric and acoustic properties, which can be attributed to the rhombohedral-orthorhombic and orthorhombic-tetragonal phase transitions. In case of [001]c-poled sample, two clear anomalies at ~116 ^oC and ~165 ^oC were exhibited. These two-step changes were attributed to the successive phase transitions from rhombohedral to tetragonal and then from tetragonal to cubic phases with increasing temperature. However, the diffuse tetragonal-cubic phase transition was not affected by the poling process, indicating that the macroscopic ferroelectric domains are transformed into mesoscopic domains and PNRs at the orthorhombic-tetragonal transition temperature. The acoustic damping in the rhombohedral phase was decreased significantly by the poling process because of the reduced density of twin domain walls and static/dynamic PNRs

References

[5.1] Y. Hosono, Y. Yamashita, K. Hirayama, and N. Ichinose, Jpn. J. Appl. Phys., **44** (2005) 7037.

[5.2] N. Yasuda, T. Fuwa, H. Ohwa, Y. Tachi, Y. Yamashita, K. Fujita, M. Iwata, H. Terauchi, and Y. Ishibashi: Jpn. J. Appl. Phys., **50** (2011) 09NC01.

[5.3] N. Hidayah, N. Yasuda, H. Ohwa, Y. Tachi, Y. Yamashita, and M. Iwata, Jpn. J. Appl. Phys., **51** (2012) 09LC06.

[5.4] S. Zhang, J. Luo, F. Li, R. J. Meyer Jr., W. Hackenberger, and T. R. Shrout, Acta Metall., **58** (2010) 3773.

[5.5] S. Zhang, J. Luo, W. Hackenberger, N. P. Sherlock, R. J. Meyer Jr., and T. R. Shrout, J. Appl. Phys., **105** (2009) 104506.

[5.6] G. F. Nataf, Q. Li, Y. Liu, R. L. Withers, S. L. Driver, and M. A. Carpenter, J. Appl. Phys., **113** (2013) 124102.

[5.7] S. Tsukada, Y. Ike, J. Kano, T. Sekiya, Y. Shimojo, R. Wang, and S. Kojima, J. Phys. Soc. Jpn., **77** (2008) 033707.

[5.8] J.-H. Ko, T. H. Kim, K. Roleder, D. Rytz, and S. Kojima, Phys. Rev. B, **84** (2011) 094123.

[5.9] S. Kojima, Jpn. J. Appl. Phys., **49** (2010) 07HA01.

[5.10] X. Huo, S. Zhang, G. Liu, R. Zhang, J. Luo, R. Sahul, W. Cao, and T. R. Shrout, J. Appl. Phys., **113** (2013) 074106.

[5.11] S. Zhang, F. Li, J. Luo, R. Xia, W. Hackenberger, and T. R. Shrout, Appl. Phys. Lett., **97** (2010) 132903.

[5.12] Q. Li, Y. Liu, J. Wang, A. J. Studer, R. L. Withers, Z. Li, and Z. Xu, J. Appl. Phys., **113** (2013) 154104.

[5.13] Z.-Y. Cheng, R. S. Katiyar, X. Yao, and A. Guo, Phys. Rev. B, **55** (1997) 0163.

[5.14] R. Vacher and L. Boyer, Phys. Rev. B, **15** (1972) 639.

[5.15] J.-H. Ko, D. H. Kim, S. Tsukada, S. Kojima, A. A. Bokov, and Z.-G. Ye, Phys. Rev. B, **82** (2010) 104110.

[5.16] J. H. Kim, J.-Y. Choi, M.-S. Jeong, J.-H. Ko, M. Ahart, Y. H. Ko, and K. J. Kim, J. Korean Phys. Soc., **60** (2012) 1419.

[5.17] Y. Zhang, D. Liu, Q. Zhang, W. Wang, B. Ren, X. Zhao, and H. Luo, J. Electron. Mater., **40** (2011) 92.

Chapter 6. Polarized Raman study of the phonon dynamics in [001]-poled Pb(In$_{1/2}$Nb$_{1/2}$)O$_3$–Pb(Mg$_{1/3}$Nb$_{2/3}$)O$_3$–PbTiO$_3$ single crystals

6. 1 Introduction

Lead magnesioniobate, Pb(Mg$_{1/3}$Nb$_{2/3}$)O$_3$ (PMN) is an well-known material as a relaxor material showing a diffuse phase transition characterized by a strong frequency dispersion of the dielectric susceptibility at temperatures near and below the T_{max}=−3 ℃ (270 K) [6.1]. However, Many properties of PMN-based relaxor are still unclear and the nature of the relaxor behavior has yet to be understood, especially relaxation behaviors. One of the difficulties is multiheterogeneity.

PMN has a perovskite structure with an averaged (macroscopic) cubic $Pm\bar{3}m$ symmetry with Mg^{2+} and Nb^{5+} ions randomly occupied B sites. However, PNRs appear below Burns Temperature, at which nanometric local polarization clusters form. Size of the PNR steadily increases from 7 to 20 nm as the temperature decreases. It would have a rhomboheral symmetry $R3m$. But, a network of superstructure clusters (COR) with face-centered cubic symmetry $Fm\bar{3}m$ destroys the picture. The size of these clusters is of the order of 2–3 nm; the distance between the centers of neighboring clusters is smaller than 5 nm [6.2-3]. Thus, the structures of PMN is considered as $R3m$, $Fm\bar{3}m$ and $Pm\bar{3}m$ symmetry in the disordered matrix.

Especially in polarized Raman scattering studies, vibrational spectrum has a shorter characteristic length scale, Raman spectrum is a good microprobe to study the nanodomain structures. But most of all, low-frequency (low-wavenumber) spectra are important because soft optic phonon mode and CP can explain phase transition behaviors and obtain relaxation time.

In the present chapter, we discuss the role of the relaxational dynamics of the PNR by the observation of the CP in the wide frequency and temperature ranges and confirm local structure from [001]-poled and unpoled PIN-PMN-PT single crystals. We offer a complex analysis of the temperature and angular dependences of the polarized (VV, $z(x,x)\bar{z}$), unpolarized (VH, $z(x,y)\bar{z}$) Raman spectra from unpoled PIN-PMN-PT crystals. This analysis is based on the multiple-peak decomposition suggested by Siny *et al.* [6.4]. For the investigation of relaxation behaviors, Brillouin and Raman spectra were measured at VV and VH scattering. The fine analysis of the CP must be important, because many papers on CPs in the spectra of Brillouin and Raman scattering discussed individually and they are contradicted each other [6.5]

6. 2 Experimental

A single crystal of 0.26PIN-0.46PMN-0.28PT was grown by the modified Bridgeman method. Each surface is perpendicular to [001]c of the pseudocubic orientation. Micro-Brillouin scattering was measured with the same setup in Chap. 4, 5, while Raman spectra were measured by a triple-grating spectrometer of additive dispersion (T64000, Horiba Jobin-Yvon) as illustrated in Fig. 3. 4 with a resolution of $1.6 \sim 1.2$ cm^{-1}. For fine measurement, we used same condition, such as objective lens and laser power at focusing area. The scattered light was collected at the scattering angle of 180° with polarized and depolarized configurations shown in Fig. 6. 1.
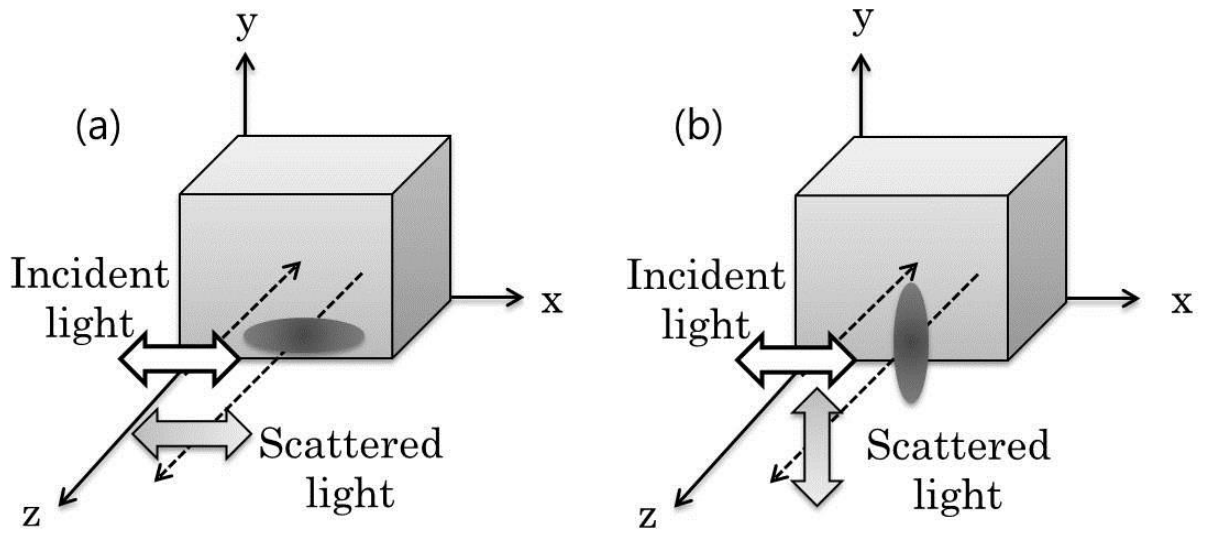
Fig. 6. 1. Two main geometries used in the light scattering experiment, (a) $z(x,x)\bar{z}$ (or VV) and (b) $z(x,y)\bar{z}$ (or VH).

To investigate angular dependence of Raman spectra, we measured polarized and depolarized Raman spectra with the same setup in Fig. 3. 5(b). It is possible to measure angular dependence without rotation of sample in cryostat.

6. 3 Results and Discussion

6. 3. 1 Analysis of Raman spectra

The polarized (VV) Raman raw and reduced intensity spectra in unpoled PIN-PMN-PT are

shown in Fig. 6. 2 at 30 ℃. As known in Fig. 6. 2, all modes are broad and overlapped. Therefore, we performed deconvolution process without partial analysis process. In order to obtain CP intensity and it's width, we directly decomposed the measured spectra using a multiple-peak fitting procedure without reduced the Bose-Einstein factor (Eq.6.1).

$$F(\omega, T) = \begin{cases} n(\omega) + 1, & \text{for Stokes part} \\ n(\omega), & \text{for anti} - \text{Stokes part,} \end{cases} \qquad (6.\,1)$$

where

$$n(\omega) = \frac{1}{\exp\left(\frac{\hbar\omega}{kT}\right) - 1}.$$

The best fits could be achieved with the assumption of a Lorentzian-type CP and other peaks described by the spectral response functions of a damped harmonic oscillators, modified by the Bose-Einstein factor;

$$I(\omega) = \frac{A}{\pi} \frac{\Delta\omega}{4\nu^2 + \Delta\omega^2} + F(\omega, T) \sum_i \frac{A_i \Gamma_i \omega_i^2 \omega}{(\omega^2 - \omega_i^2)^2 + \omega^2 \Gamma_i^2} \qquad (6.\,2)$$

where ω_i, A, and Γ are peak position, intensity, and width, respectivly. $\Delta\omega$ of CP fitted parameter is related $1/\pi\tau$, where τ is relaxation time [6.11~13].
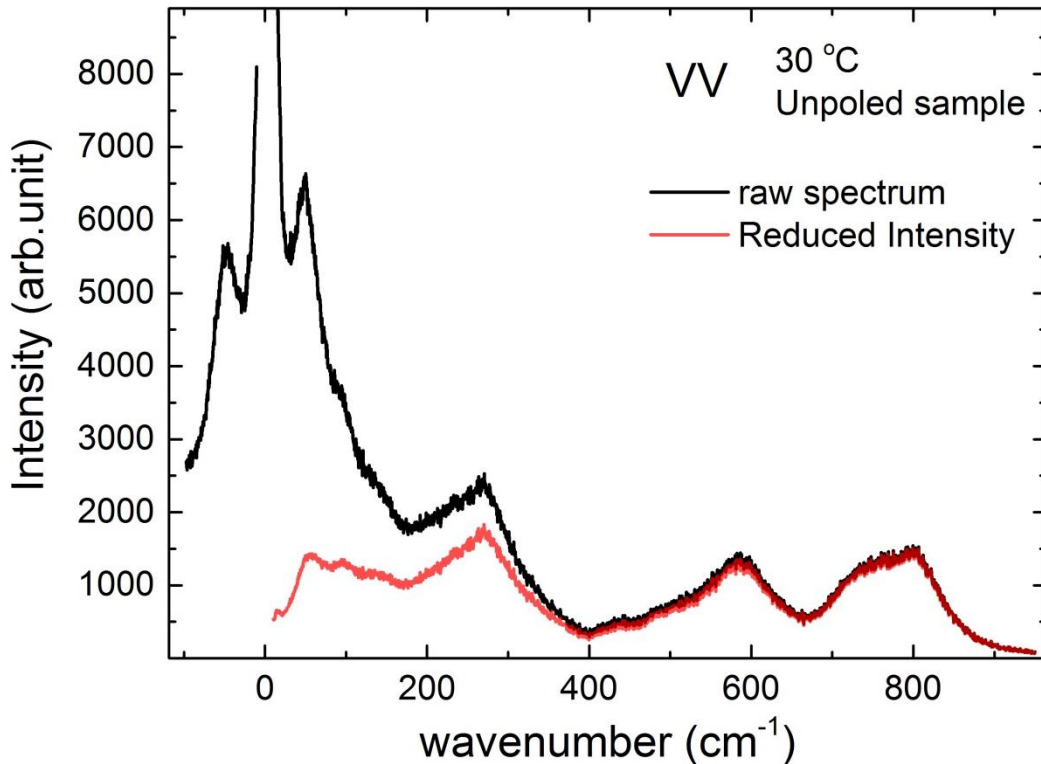

Fig. 6. 2. Polarized Raman spectra from raw data (black line) and corrected by the Bose-Eistein factor (red line).

6. 3. 2 Angular dependence of Raman spectra in unpoled PIN-PMN-PT

Figs. 6. 3(a) and 3(b) show the angular dependence of Raman spectra in unpoled PIN-PMN-PT at 300 °C observed with VV and VH configurations, respectively. The Raman spectra clearly change periodically with rotation. In particular, the intense peak at around 50 cm^{-1} (in case of PMN, a low-frequency peak is located 45 cm^{-1}), indicated by red closed circles, changes markedly in intensity. However, the variation of the intensity of other peak is smaller than PMN crystal [6.6]. It is considered more complex disordered matrix form by added anti-ferroelectric PIN composition even though they has PT composition which contribute long-range order.
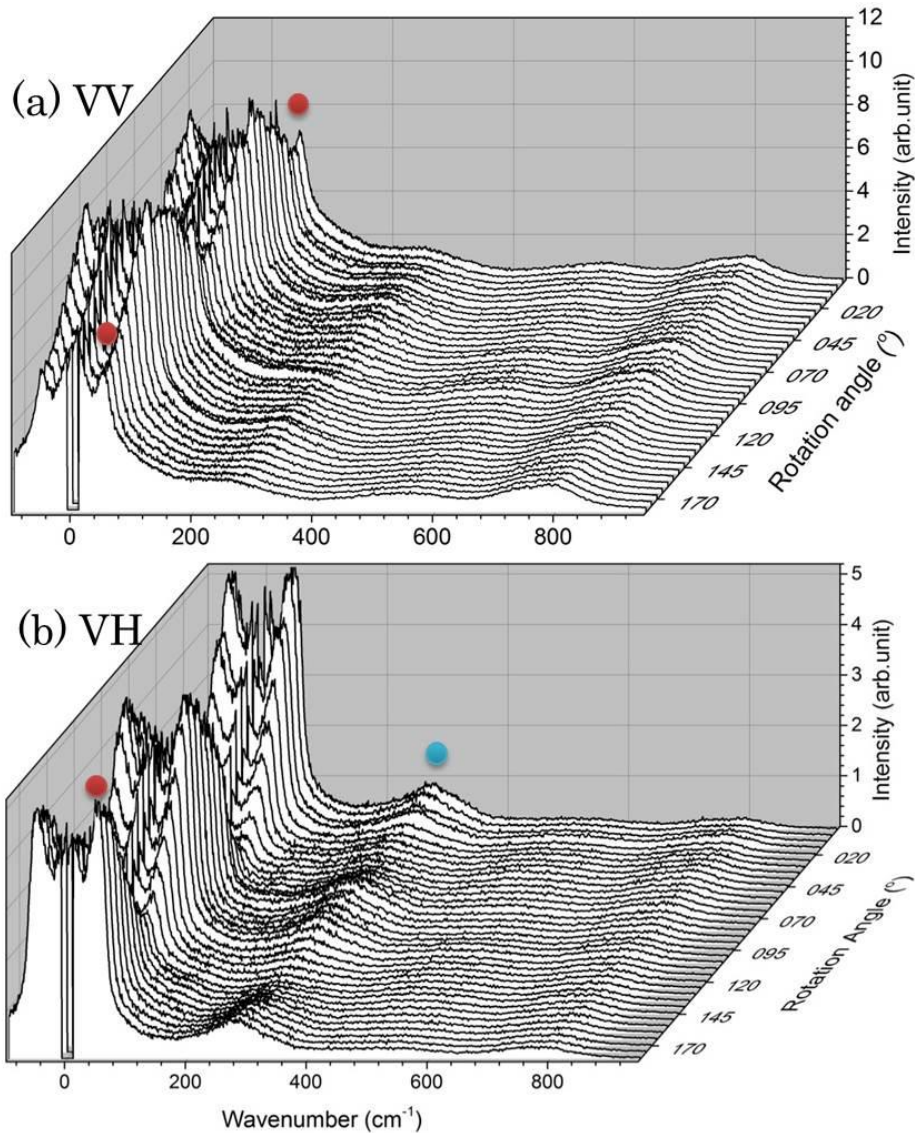
Fig. 6. 3. Angular dependences of the Raman spectra in unpoled PIN-PMN-PT. (a) and (b) present the spectra observed with VV and VH configurations, respectively.

To analyze the angular dependences of Raman spectra, we carry out Raman tensor analysis with rotation matrices about the cubic [001]c axis. From Table 2. 2-3, $Fm\bar{3}m$ symmetry has four Raman active mode ($2F_{2g}$, E_g, and A_{1g}). The Raman tensors of these modes are as follows;

$$A_{1g}: \begin{pmatrix} a & 0 & 0 \\ 0 & a & 0 \\ 0 & 0 & a \end{pmatrix}$$

$$E_g: \begin{pmatrix} b & 0 & 0 \\ 0 & b & 0 \\ 0 & 0 & b \end{pmatrix}$$

$$F_{2g}: \begin{pmatrix} 0 & d & d \\ d & 0 & d \\ d & d & 0 \end{pmatrix}, \qquad (6.3)$$

where a, b, and c are constants. For the calculation of angular dependence, the rotation matrix $\vec{R}$ is expressed as follow;

$$\vec{R}: \begin{pmatrix} \cos\theta & \sin\theta & 0 \\ -\sin\theta & \cos\theta & 0 \\ 0 & 0 & 1 \end{pmatrix}. \qquad (6.4)$$

The angular dependences are calculated by

$$\vec{R}^{-1} \cdot (A_{1g} \text{ or } E_g \text{ or } F_{2g}) \cdot \vec{R}. \qquad (6.5)$$

The calculated angular dependences of the Raman intensities are described in Fig. 6. 4 by using F_{2g} mode. Because the A_{1g} and E_g modes show angular independence in VV mode.
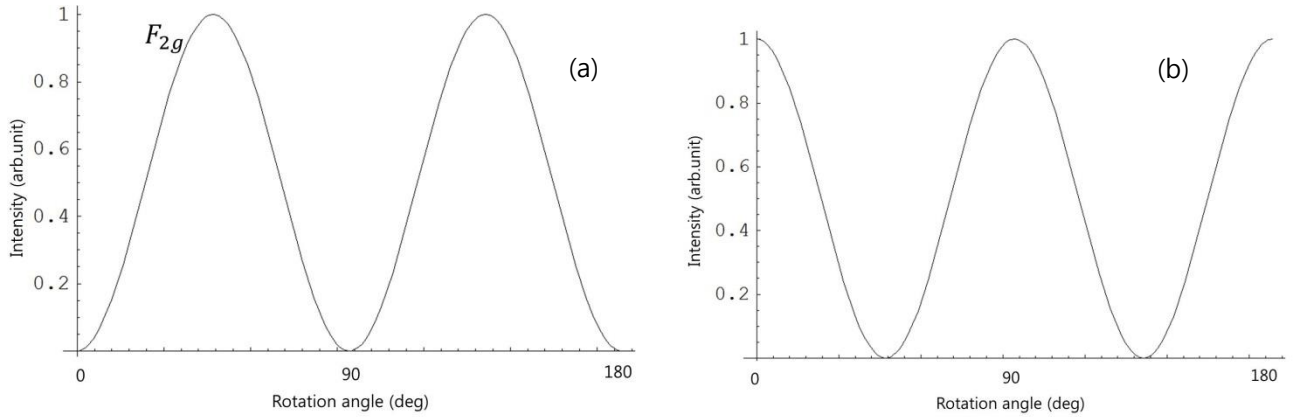

Fig. 6. 4. Calculated angular dependence of Raman scattering intensity in $Fm\bar{3}m$. (a) and (b) are for the VV and VH configurations, respectively.

In case of PMN, the observed intensity variation conforms to the calculated results, indicated that the strong components at around 45 cm^{-1} stem from the COR of $Fm\bar{3}m$ symmetry. Also, the first-principles calculation indicated that the mode in the $Fm\bar{3}m$ region is located at around 45 cm^{-1} [6.7].
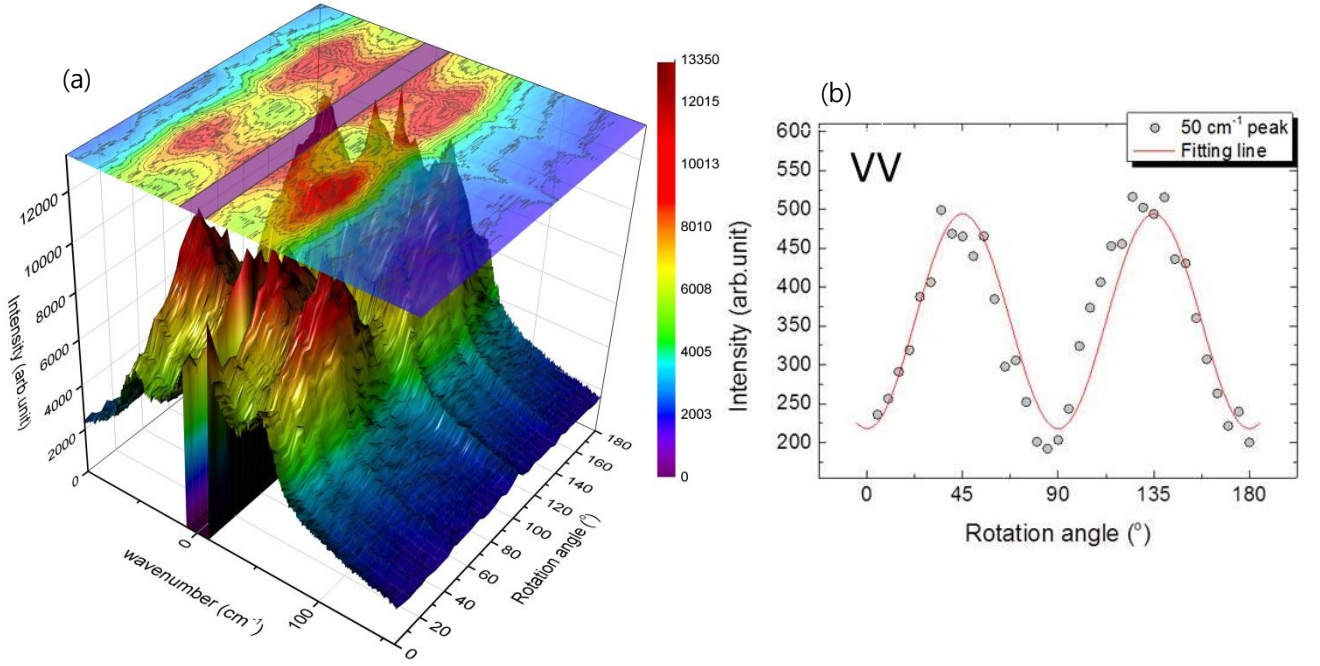
Fig. 6. 5. (a)Contour 3D map of polarized (VV) Raman scattering intensity from an unpoled PIN-PMN-PT crystal vs. rotation and wavenumber (-100~150 cm^{-1}). (b)Observed angular dependences of the peak intensity at 50 cm^{-1} were calculated with Eq. 6. 3, 5. Calculated curves are denoted by red solid line, which is for the VV configuration.

We now compare the observed intensity variation for the low-frequency component at 50 cm^{-1} with calculated intensity. It is incredibly similar to PMN results. On the other hand, angular dependence of the peak around 50 cm^{-1} is not compatible with that of $R3m$ symmetry for PNR. It is therefore reasonable to assign it to the F_{2g} mode of $Fm\overline{3}m$ symmetry.

6. 3. 3 Temperature dependence of Raman spectra

The deconvolutions of the Raman spectra of depoled PIN-PMN-PT are presented in Fig. 6. 6. At 30 °C, polarized spectrum is decomposed into 11 lines. The peak frequencies are almost independent of temperature. Also, VH spectra show normal cubic symmetry type spectra. However, some of peaks appeared broad phase transition behavior related dynamics of PNRs. As mentioned in chap. 1, COR shows temperature independence. Therefore peak intensity of F_{2g} mode of $Fm\overline{3}m$ symmetry doesn't grow rapidly below Bruns temperature. Unlike the peak of COR, 560 cm^{-1} peak increase dramatically below T^* as Fig. 6. 7. It was suggested that the onset of rapid growth in the size of PNRs and local phase transformation. This temperature almost same Brillouin scattering result. Also, the angular dependence of the intensity variation of 560 cm^{-1} peak conformed by the Raman tensor analysis in the $R3m$.
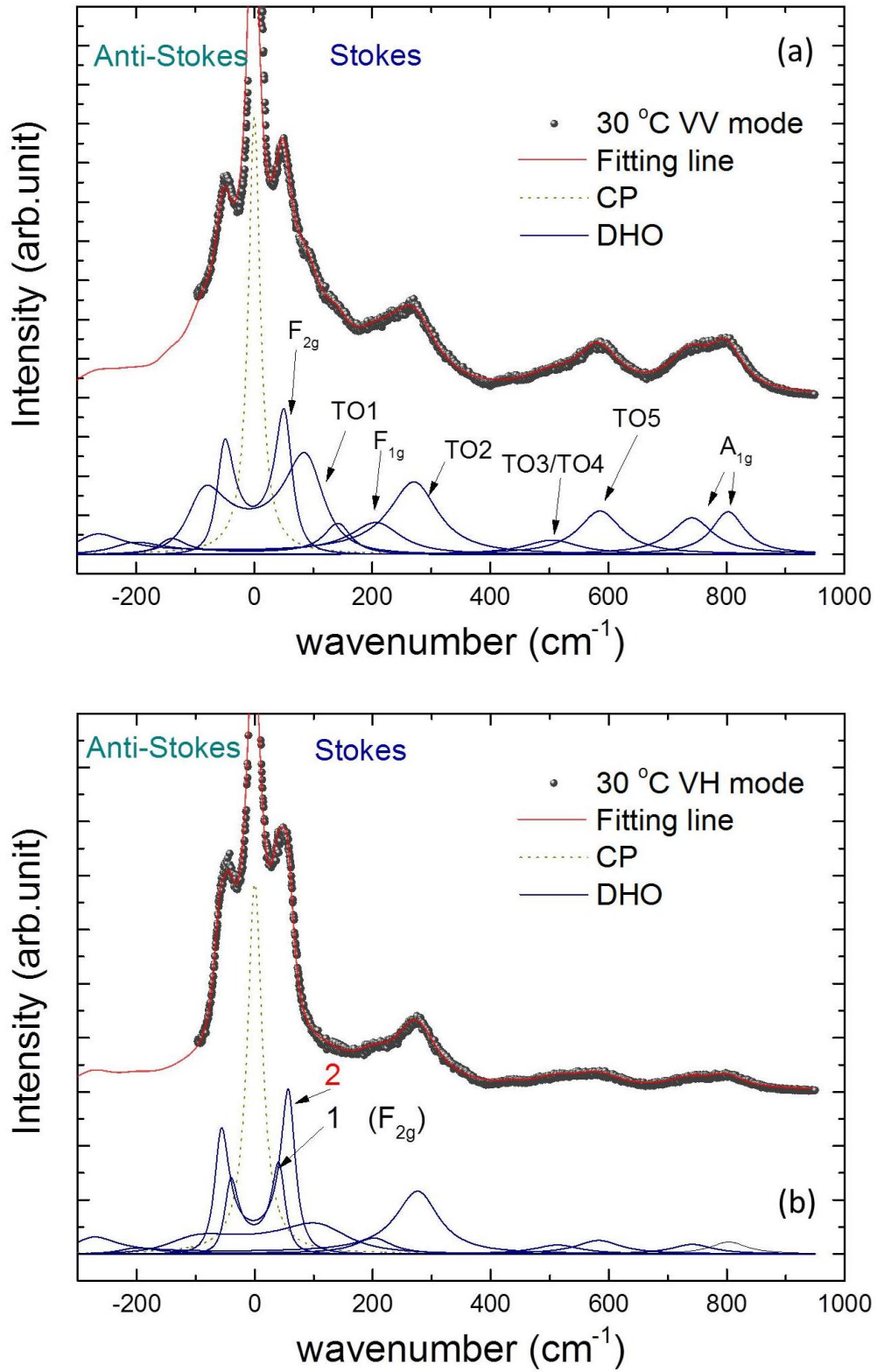
Fig. 6. 6. Examples of multiple peak decomposition of Rama spectra measured at 30 °C in (a)VV and (b)VH geometry. The mode assignment cited results of first principles computations in $Pm\bar{3}m$ [6.7].
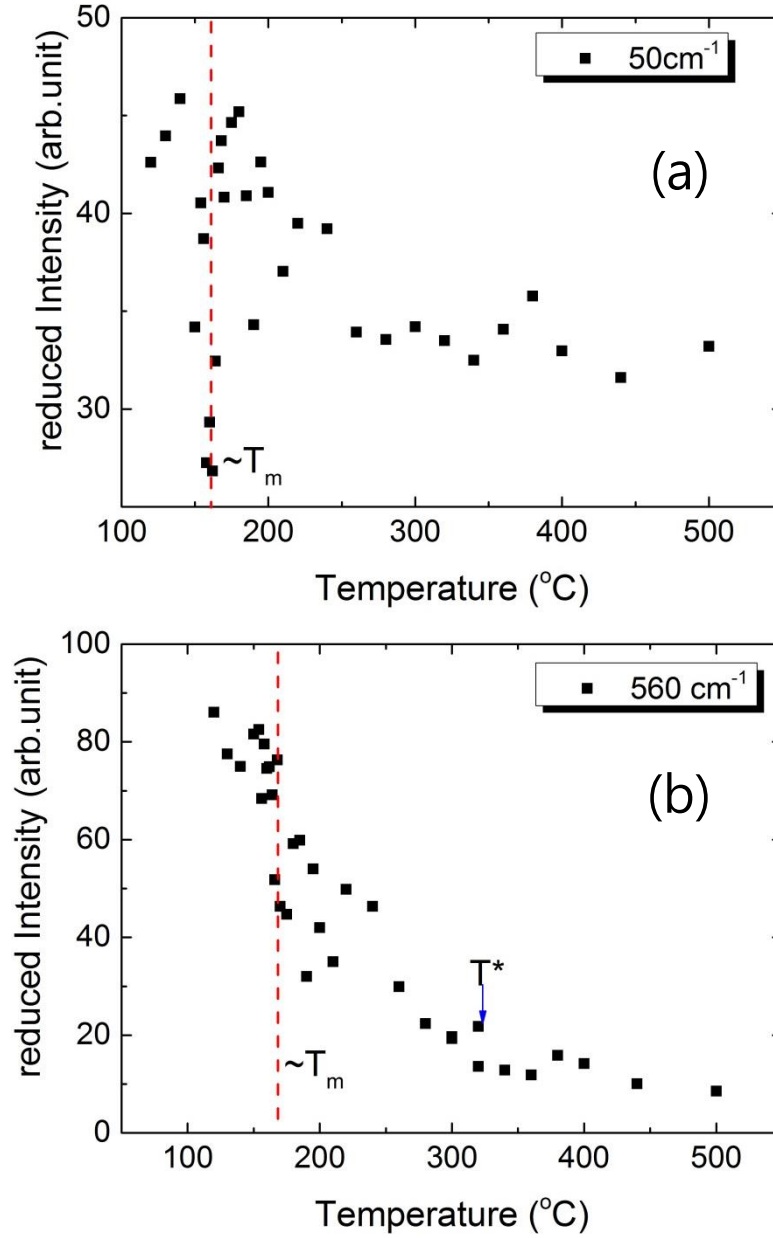
Fig. 6. 7. Temperature dependences of the intensity of the Raman peaks in (a) 50 cm⁻¹ and (b) 560 cm⁻¹.

From these results, we confirmed two types of local structure in unpoled PIN-PMN-PT: the rhombohderally disorted PNR of $R3m$ symmetry and 1:1 chemically order region of $Fm\bar{3}m$ symmetry. However, we can't find $Pm\bar{3}m$ symmetry by using present Raman analysis. Because first-order scattering doesn't allow Raman selection rule above T_c ($Pm\bar{3}m$).

Fig. 6. 8 shows temperature dependences of the Raman peak positions and the intensity of peaks 1 and 2 of depolarized spectra. From here, we can find step-like change of peaks 1 and 2

near T_{R-T}. Unfortunately, other peaks are too board and shape of spectra are too similar in cubic and tetragonal symmetry in PIN-PMN-PT, we can't obtain other structure phase transition temperature such as T_c.
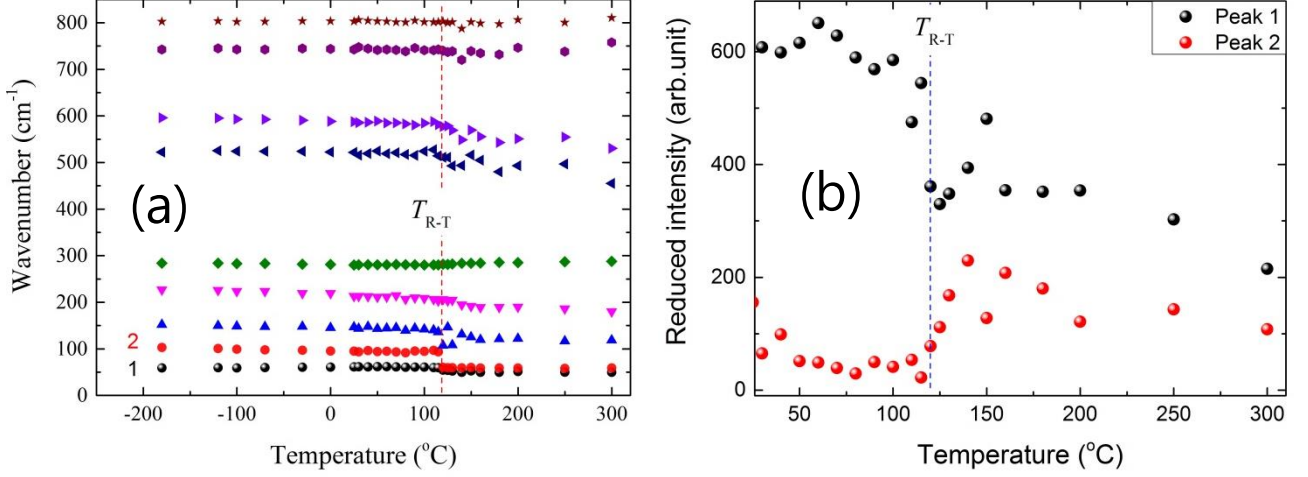

Fig. 6. 8 shows temperature dependences of the Raman peak positions and the intensity of peaks 1 and 2 of depolarized spectra.

6. 3. 4 Two polarization relaxation observed in CP

The CP of a PIN-PMN-PT single crystal cannot be reproduced by single Debye-type relaxation in a Brillouin scattering range. To confirm the lineshape of the CP, the spectra VH scattering geometry are analyzed. Because the intensity of the CP in VV scattering geometry doesn't change below Burns temperature. As a first step to clarify its shape, Brillouin and Raman spectra are combined to make the scanning range broad. Fig. 6. 9 shows the combined spectra at two temperatures. They indicate that each CP can be expressed by two Debye-type relaxations.

To connect between Brillouin and Raman spectra, the Brillouin spectra are measured in as wide frequency range as possible (to 600 GHz) on a (001)c plate. The FWHM of the broader one (~300GHz) corresponds to the single Debye-type CP in the Raman spectrum. In the case of relaxor ferroelectrics, softening transverse optical phonon inside the PNRs exists below Bruns temperature [6. 8], then, the CP appears. Therefore, the induced local polarization inside the PNRs is the most probable origin of the relaxation process observed in the CP [6.9].

Origins of two relaxations could refer to the flipping motions of the polarization inside a PNR. From diffuse neutron scattering in PMN [6.10], the polarization inside a PNR has been reported to align along the eight equivalent [111]c. Therefore, the slower relaxation process (the narrow Lorentzian peak) can correspond to the non-180° flipping accompanied by the

change in strain, while the faster relaxation process (the broad peak) can correspond to the 180º flipping free from any change in strain [6.9].
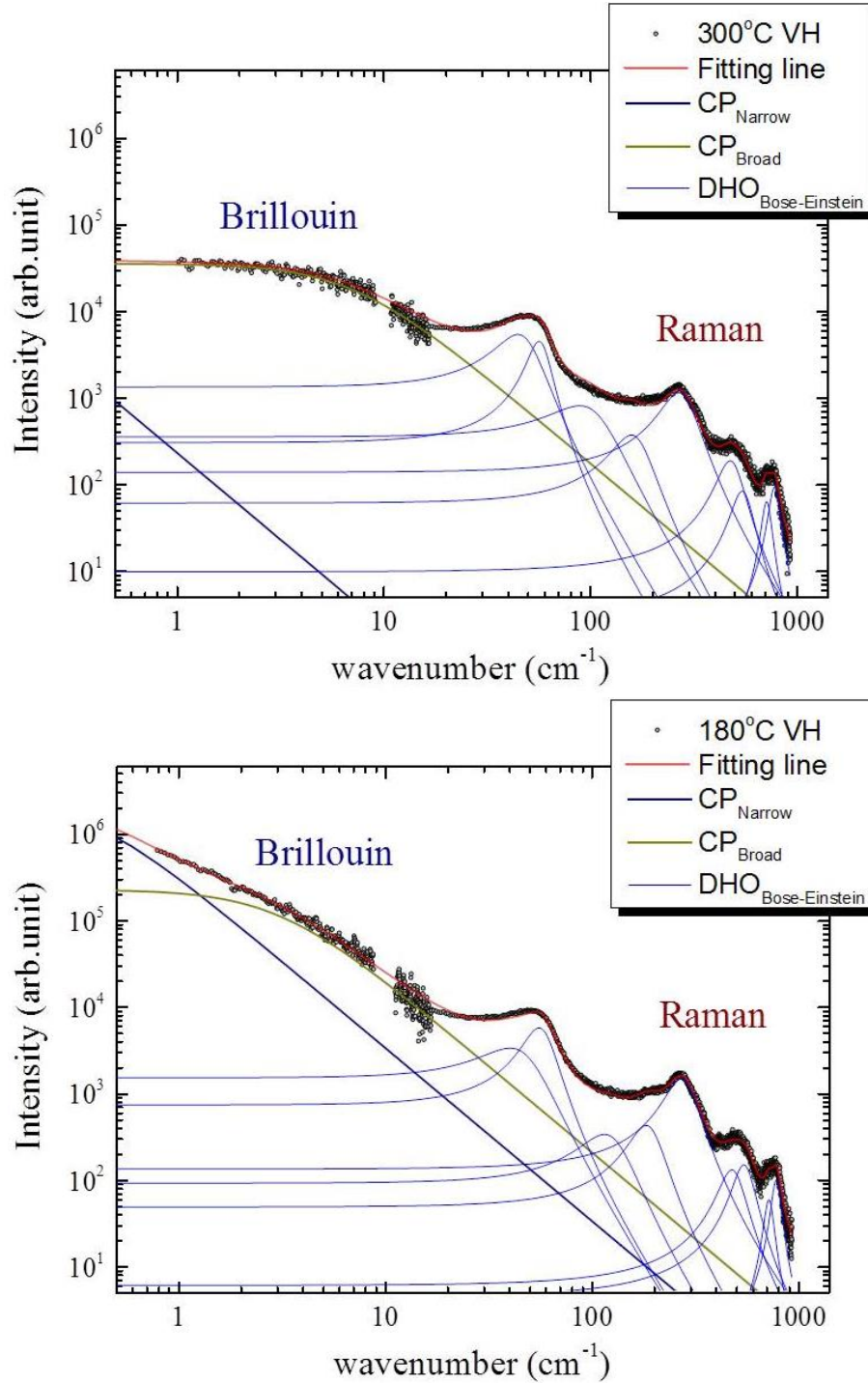

Fig. 6. 9. Broadband spectra of PIN-PMN-PT at VH scattering geometry at 300 ºC and 180 ºC in log-log scale. Two spectra with different instruments are combined for the better understanding of the lineshape. Fitted curves are constituted with two Debye-type relaxations for the CP and DHOs with Bose-Einstein factor.

The obtained temperature dependence of the slower relaxation time and the CP intensity is shown in Fig. 6.10. τ_{ncp} is of the order picoseconds and rapidly grows toward T_m. However, inverse of the slower relaxation time does not show linear behavior as Fig. 6. 10(b). The typical critical slowing down is not observed near T_C. The local transition from dynamic to static PNRs stops the farther slowing down. To reproduce such a suppressed slowing down by random fields, we proposed the empirical equation of the stretched slowing down in the vicinity of T_C as given by

$$\frac{1}{\tau} = \frac{1}{\tau_0} + \frac{(T-T_c)^\beta}{\Delta'}, (1 \leq \beta) \qquad (6.6)$$

where β is the stretched index. In the case of $\beta = 1.0$, the eq. (6.7) gives the normal critical slowing down without random fields. In the case of $\beta > 1.0$, the slowing down of relaxation time is suppressed and/or stretched by the increase of the strength of random fields.

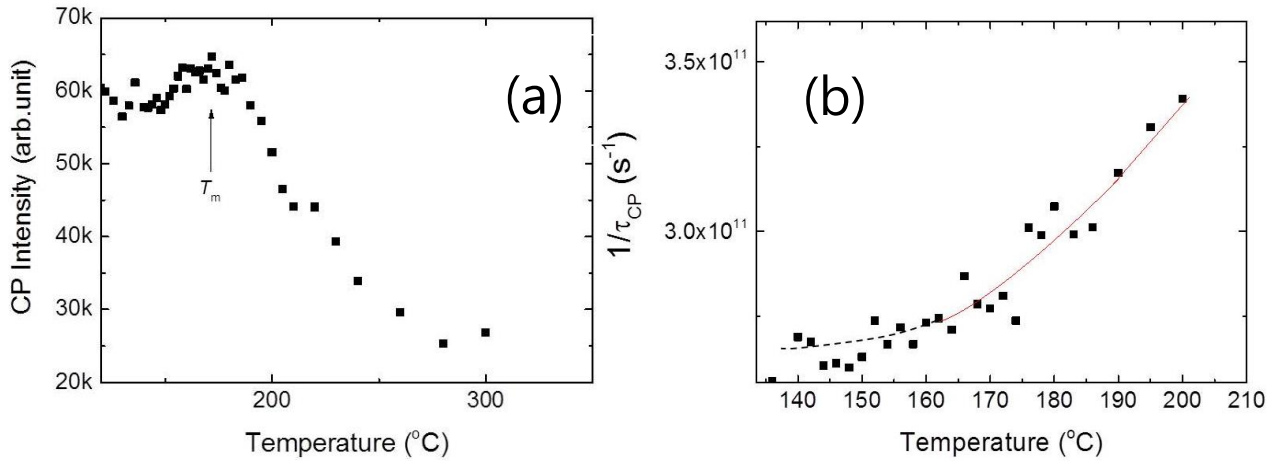$$\frac{1}{\tau} = \frac{1}{\tau_0} + \frac{T-T_c}{\Delta}. \qquad (6.7)$$

Fig. 6. 10. Temperature dependences of (a) the narrow CP intensity and (b) the inverse slower relaxation time of a PIN-PMN-PT crystal. The solid line shows the values calculated by Eq. 6.6 of stretched slowing down.

As shown Fig. 6. 10(b), it is found that the value of β=1.3. However, the inverse fast relaxation time of a broad central peak as a function of temperature shows a linear behavior at short temperature range. This kind of temperature dependence is typical critical slowing down in order–disorder type phase transitions.
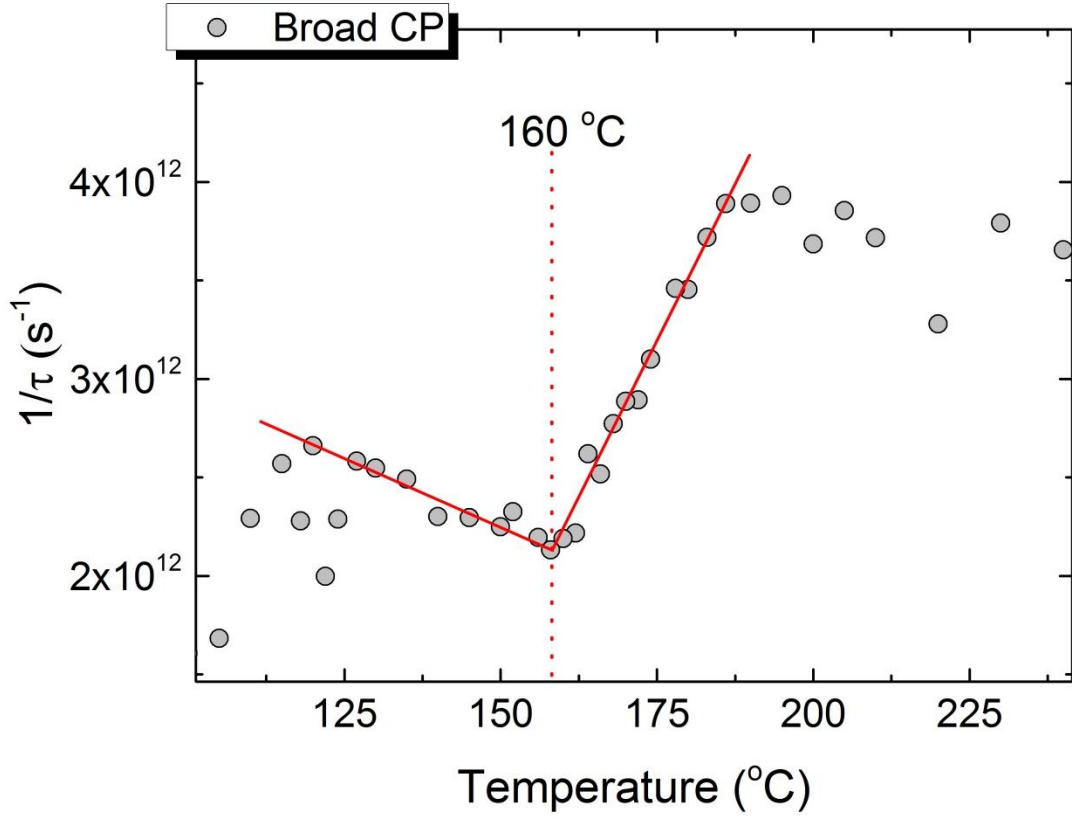
Fig. 6. 11. The inverse of the faster relaxation time of PIN-PMN-PT along with the best-fitted reuslts (solid lines) by using Eq. 6. 7.

6. 4 Conclusion

Dynamical properties of the optic phonon and the PNRs of a relaxor ferroelectric PIN-PMN-PT single crystal are studied in a broad frequency range from 10 GHz to 28.5 THz to explain the mechanism of the diffuse ferroelectric phase transition. The CP is temperature dependent in a wide temperature range, and two Debye-type relaxations are attributed to the CP. The fast (short range dynamics) and slow (long range dynamics) relaxations show different behavior. The slow relaxation process is considered to originate from the suppressed slowing down by random fields. On the contrary, the inverse of the fast relaxation time shows critical slowing down behavior in a narrow temperature range. From these results, we consider that added PIN composition form random fields in long range scale but added PT composition develop short range ferroelectric ordering near T_m. In addition, we confirm $Fm\bar{3}m$ and $R3m$ types of local structures in the disordered cubic matrix of PIN-PMN-PT by using angular dependence of Raman scattering.

References

[6.1] V. A. Bokov and I. E. Myl'nikova, Sov. Phys. Solid State, **3** (1961) 613.

[6.2] D. Viehland, S. Jang, and L. E. Cross, Philos. Mag. B, **64** (1991) 335.

[6.3] J. Chen, H. M. Chan, and M. P. Harmer, J. Am. Ceram. Soc., **72** (1989) 593.

[6.4] I. G. Siny, S. G. Lushnikov, R. S. Katiya, and E. A. Rohacheva, Phys. Rev. B, **56** (1997) 7962.

[6.5] Y. Nakata, Y. Tsujimi, K. Katsuraya, M. Iwata, and T. Yagi, Appl. Phys. Lett., **89** (2006) 22903.

[6.6] H. Taniguchi, M. Itoh, and D. Fu, J. Raman Spectrc., **42** (2011) 706.

[6.7] S. A. Prosandeev, E. Cockayne, B. P. Burton, S. Kamba, J. Petzelt, Y. Yuzyuk, R. S. Katiyar, S. B. Vakhrushev, Phys. Rev. B, **70** (2004) 134110.

[6.8] K. Hirota, S. Wakimoto, and D. E. Cox, J. Phys. Soc. Jpn., **75** (2006) 111006.

[6.9] S. Tsukada and S. Kojima, Phys. Rev. B, **78** (2008) 144106.

[6.10] G. Xu, G. Shirane, J. R. D. Copley, and P. M. Gehring, Phys. Rev. B, **69** (2004) 64112.

[6.11] A. Slodczyk, P. Daniel, and A. Kania, Phys. Rev. B, **77** (2008) 184114.

[6.12] O. Svitelskiy, J. Toulouse, G. Yong, and Z. –G. Ye, Phys. Rev. B, **68** (2003) 104107.

[6.13] J. Toulouse, F. Jiang, O. Svitelskiy, W. Chen, and Z. –G. Ye, Phys. Rev. B, **72** (2005) 184106.

[6.14] S. Kojima and S. Tsukada, Ferroelectric, **405** (2010) 32.

Chapter 7. Summary

I compared the phase transition behaviors of unpoled and [001]c-and [011] c-poled 0.26PIN–0.46PMN–0.28PT single crystals by using Brillouin, Raman light scattering and dielectric spectroscopies.

We explained that unpoled and [001]c-and [011] c-poled samples showed various phase transition behaviors by using considered dynamic/static behaviors of PNRs with local random field.

In case of a [001]c-poled sample, The high temperature tetragonal-cubic phase transition remained diffused even for the poled sample, which may be understood as the transformation of macrodomains into microdomains upon heating due to local random fields inherent in relaxors.

In case of a [011]c-poled sample, the diffuse tetragonal–cubic phase transition was not affected by the poling process, indicating that the macroscopic ferroelectric domains are transformed into mesoscopic domains and PNRs at the orthorhombic–tetragonal transition temperature. The acoustic damping in the rhombohedral phase was decreased significantly by the poling process because of the reduced density of twin domain walls and static/dynamic PNRs.

The unpoled sample showed broad elastic softening along with substantial dielectric dispersion, which is typical in relaxors. At 300 ^{o}C, the symmetry of B-site ordering CORs was confirmed by investigating the angular dependence of low-frequency Raman spectra. The CORs are located in a stable equilibrium state like PMN. Therefore, dynamic PNRs must play an essential role in the formation of complex dynamic characteristics and/or diffuse ferroelectric phase transition of this ternary system. The Burns temperature was determined to be about 550 ^{o}C by observing the spectral changes as deviated normal lattice anharmonicity. The small damping peak at 90 ^{o}C was attributed to the development of moderately diffused and short-ranged (or mesoscopic) polar state due to the abrupt growth and merging of PNRs without changing the directions of their dipole moments. Poling the crystal under DC bias field of 15 kV/cm along the [001]c and [011]c direction gave rise to the appearance of the TA mode, suppression of the central peak, and substantial changes in the LA mode properties, indicating structural transformation from the short-range polar state into a domain-engineered 4R and 2R state, respectively.

Two relaxations in an unpoled PIN-PMN-PT sample are investigated by the Brillouin and Raman scattering. The slower and faster relaxation times determined by assuming the two Debye-type relaxations. We attribute the fast and slow relaxations to the thermally activated flipping of polarization inside the PNRs from compositional fluctuation. We consider that the

faster relaxation indicates short range dynamics with ferroelectric order parameter by added ferroelectric PT composition, while, the slower relaxation indicates long range dynamics with the suppressed slowing down by random fields by added anti-ferroelectric PIN composition.

Acknowledgements

Papers closely related to my dissertation

<u>Tae Hyun Kim</u>, Jae-Hyeon Ko, and Seiji Kojima

Phase Transition Behaviors in [011]-Oriented Pb(In1/2Nb1/2)O3–Pb(Mg1/3Nb2/3)O3–PbTiO3 Single Crystals Studied by Dielectric and Micro-Brillouin Spectroscopies,

Japanese Journal of Applied Physics, **52**　(2013) 09KC01.

<u>Tae Hyun Kim</u>, Seiji Kojima, and Jae-Hyeon Ko

Phase transition behaviors in relaxor ferroelectric [001]-poled Pb(In1/2Nb1/2)O3-Pb(Mg1/3Nb2/3)O3-PbTiO3 single crystals studied by Brillouin light scattering and dielectric spectroscopies

Journal of Applied Physics, **111** (2012) 054103.

Other Related Papers

<u>Tae Hyun Kim,</u> Jae-Hyeon Ko, Seiji Kojima, Alexei A. Bokov, Xifa Long, and Zuo-Guang Ye

Phase transition behaviors of $PbZr_{1-x}Ti_xO_3$ single crystals as revealed by elastic anomalies andcentral peaks,

Applied Physics Letters, 100, (2012) 082903.

<u>Tae Hyun Kim</u>, Jae-Hyeon Ko, Haruki Takayama, Tomohiko Shibata, and Seiji Kojima

Glass Transition Dynamics of Enantiomer (+)-Ibuprofen,

AIP Conf. Proc. **1518**, (2013) 316.

<u>Tae Hyun Kim</u>, Seiji Kojima, Chang Won Ahn, Ill Won Kim, and Jae-Hyeon Ko

Raman- and Brillouin-scattering Studies on Lead-free Piezoelectric Bi0.5(Na0.78K0.22)0.5−xTiO3 Ceramics with A-site Vacancies,

Journal of the Korean Physical Society, **62**, (2013) 1009.

Shinya Tsukada, <u>**Tae Hyun Kim**</u>, and Seiji Kojima

Large acoustic thermal hysteresis in relaxor ferroelectric $Pb(Zn_{1/3}Nb_{2/3})O_3$-$PbTiO_3$,

APL Materials, 1, (2013) 032114.

Mirosław Maczka, <u>**Tae Hyun Kim**</u>, Maciej Ptak, Irena Jankowska-Sumara, Andrzej Majchrowski, and Seiji Kojima

High-resolution Brillouin scattering studies of phase transitions and precursor phenomena in $PbZr_{0.78}Sn_{0.22}O_3$ single crystals,

Journal of Alloys and Compounds, 587, (2014) 273.

Jae-Hyeon Ko, **Tae Hyun Kim**, K. Roleder, D. Rytz, and Seiji Kojima

Precursor dynamics in the ferroelectric phase transition of barium titante single crystals studied by Brillouin light scattering,

Physical Review B, 84, 094123 (2011) 094123.

Jae-Hyeon Ko, **Tae Hyun Kim**, Seiji Kojima, Ki-Soo Lim, and Tae-Yeong Koo

Effects of Sr content and bias field on acoustic properties of strontium barium niobate studied by Brillouin light scattering,

Applied Physics Letters, 99, (2011) 212902.

T. Shibata, H. Takayama, **T. H. Kim**, and S. Kojima

Acoustic and thermal anomalies in a liquid-glass transition of racemic S(+)-R(-) ketoprofen,

Chemical Physics Letter, 592, (2014), 80

J.-H. Ko, **T.H. Kim**, S. Kojima, K. Roleder, and D. Rytz

Precursor dynamics in rhodium-doped barium titanate single crystals studied by Brillouin light scattering and birefringence measurements,

Phase Transitions, 85, (2012) 718.

Jae-Hyeon Ko**, Tae Hyun Kim**, Kwang-Sei Lee, Seiji Kojima

Brillouin scattering study on crystalline and glassy states of antiflamamatory racemic S(+)-R(--) ibuprofen,

Chemical Physics Letters, 515, (2011) 221.

Jae-Hyeon Ko, **Tae Hyun Kim**, Shinya Tsukada, Seiji Kojima, Tae-Yeong Koo

Comparison of acoustic properties between ferroelectric $bAtIo_3$ AND $pBtIo_3$ single crystals,

Ferroelectrics, 420, (2011) 66.